Spring 1-1-2011

Mode Theory of Multi-Armed Spiral Antennas and Its Application to Electronic Warfare Antennas

Matthew John Radway
University of Colorado at Boulder, mradway@gmail.com

Mode Theory of Multi-Armed Spiral Antennas and Its Application to Electronic Warfare Antennas

by

Matthew J. Radway

B.S., South Dakota School of Mines and Technology, 2005

M.S., University of Colorado, 2011

A thesis submitted to the

Faculty of the Graduate School of the

University of Colorado in partial fulfillment

of the requirements for the degree of

Doctor of Philosophy

Department of Electrical, Computer, and Energy Engineering

2011

This thesis entitled:
Mode Theory of Multi-Armed Spiral Antennas and Its Application to Electronic Warfare Antennas
written by Matthew J. Radway
has been approved for the Department of Electrical, Computer, and Energy Engineering

_____

Dejan S. Filipović

_____

Michael C. Buck

Date _____

The final copy of this thesis has been examined by the signatories, and we find that both the content and the form meet acceptable presentation standards of scholarly work in the above mentioned discipline.

Radway, Matthew J. (Ph.D., Electrical Engineering)

Mode Theory of Multi-Armed Spiral Antennas and Its Application to Electronic Warfare Antennas

Thesis directed by Prof. Dejan S. Filipović

Since their invention about 55 years ago, spiral antennas have earned a reputation for providing stable impedance and far-field patterns over multi-decade frequency ranges. For the first few decades these antennas were researched for electronic warfare receiving applications, primarily in the 2-18 GHz range. This research was often done under conditions of secrecy, and often by private contractors who did not readily share their research, and now have been defunct for decades. Even so, the body of literature on the two-armed variant of these antennas is rich, often leading non-specialists to the misconception that these antennas are completely understood. Furthermore, early work was highly experimental in nature, and was conducted before modern data collection and postprocessing capabilities were widespread, which limited the range of the studies. Recent research efforts have focused on extending the application of spirals into new areas, as well as applying exotic materials to improve their performance and reduce their size. While interesting results have been obtained, in most instances these were incomplete, often compromising the frequency independent nature of these antennas.

This thesis expands the role of the multi-armed spiral outside of its traditional niche of receive-only monopulse direction finding. As a first step, careful study of the spiral-antenna mode theory is undertaken with particular attention paid to the concepts of mode filtering and modal decomposition. A technique for reducing the modal impedance of high arm-count spirals is introduced. The insights gained through this theoretical study are first used to improve the far-field performance of the coiled-arm spiral antenna. Specifically, expanding the number of arms on a coiled arm spiral from two to four while providing proper excitation enables dramatically improved broadside axial ratio and azimuthal pattern uniformity.

The multiarming technique is then applied to the design of an antenna with exceptionally stable and clean radiation patterns without use of an absorbing cavity. The multiarming technique allows the spiral to retain its pattern integrity at frequencies well below those of comparable two-armed spiral antennas. A quadrifilar helix-type of end-loading is applied to the end of the spiral, resulting in dramatically-improved low-

frequency gain. Careful application of resistive end-loading allows good impedance matching at frequencies as low as one-half of the Mode 1 cutoff frequency, while providing acceptable radiation efficiency due to effective use of the available antenna volume. A novel dual-layering technique for reducing the spiral's modal impedance is presented, allowing the antenna to present a good impedance match to a 50 ohm system.

The third application of mode theory has been to exploit the wideband multi-mode capability of the multi-armed spiral antenna to implement a simple wide-band radiation pattern nulling technique on a multi-armed spiral antenna. It is shown that wideband nulling is possible and that, in contrast to traditional array antennas, grating lobes do not appear even over extremely wide bandwidths. Simple techniques for addressing the phenomenon of null rotation with frequency are discussed.

Finally, mode theory has been used to analyze beamformer non-idealities. This has led to the revelation that the spectral distribution of beamformer errors is at least as important as the magnitude of those errors. Proper choice of beamformer topology can result in noticeable improvement in the antenna performance.

Dedication

To my beautiful wife Kendra and our lovely new daughter Franchesca.

Acknowledgements

I would like to thank the Office of Naval Research, United States Navy, for supporting the majority of the research in this thesis, and Dr. Peter Craig for providing valuable guidance in meeting the Navy's research objectives. I would also like to express my gratitude to Mr. Tom Cencich at Lockheed Martin Space Systems Company, which supported my early research. I am also thankful to FIRST RF Corporation for providing me valuable work experience as a summer intern. Dr. C. J. Reddy at EMSS-USA provided **FEKO** licenses that enabled much of the research reported in this thesis.

I would like to thank my advisor, Prof. Dejan Filipovic, for many things. For the past four years he has provided a stable, supportive, and flexible research environment. Graduate school has turned out much different than I thought it would be, and Filip's constant direction and encouragement has greatly enhanced my education. I'm happy and grateful to have the opportunity to continue our productive working relationship.

I owe Dr. Neill Kefauver a big debt of gratitude for his help with getting measurements for my antennas, mostly done on the weekend late at night. Among other things he taught me effective use of MATLAB, and how to solder together a coax bundle correctly. This thesis has been greatly enhanced thanks to our many fruitful technical conversations.

Anything I can put in words will fall far short of my true feelings for Kendra. Kendra was the one who convinced me to go to graduate school in the first place. In addition to her unwavering love and support, her genuine interest in my research and her organizational skills have been of huge practical value, especially during certain critical periods. There is no way I could have done this without her.

Contents

Chapter

Tables

Table

Figures

Figure

Chapter 1

Introduction

1.1 Historical Background

1.1.1 Experimental Development

While it is generally accepted that Edwin Turner invented the planar spiral antenna, its development was anticipated to some extent by J. S. Chatterjee [5] at Calcutta University in his work submitted for publication in late 1952. In his paper he describes a substantial bandwidth enhancement obtained by deforming a single-armed axial-mode cylindrical helix into a conical spiral shape. However, his antenna was excited at the bottom of the conical spiral, and therefore the huge pattern bandwidth of the center-fed spiral was not observed due to what would today be recognized as modal contamination. His work also mentioned the single-arm spiral, but this antenna has well-known limitations compared to the two-armed spiral invented by Turner.

Edwin Turner, a scientist at Wright Air Development Center (now Wright-Patterson Air Force Base), invented the spiral antenna when he wrapped the arms of a dipole antenna into a spiral shape and noted the huge increase in bandwidth that resulted. He filed for a patent [6] on his invention in 1955 and it immediately became a sensation among the national defense-related antenna community. The preferred embodiment was described as a center-fed two-armed spiral, backed by a shallow reflecting cavity. The primary advantages of the spiral were noted in the patent: wide bandwidth, high efficiency, circular polarization, and a wide broadside radiation pattern.

In 1958 Dyson [7] studied the center-fed two-armed equiangular conical spiral, showing improved gain

compared to the planar spiral over a 10:1 bandwidth. The next year Dyson published [8] his experimental work on the planar equiangular spiral. His paper continues to be the most frequently-cited research on planar spiral antennas.

The first design of a spiral antenna capable of handling high power was presented in [9]. The spiral was fashioned from copper tubing and foamed dielectric, wrapped into a tight Archimedean spiral shape. Average power handling was found to be in excess of 500 W over 2-4 GHz. Another high-power design [10] achieved 600 W at 2.45 GHz, designed to be used with a high-gain fused silica lens.

In 1961 Kaiser proposed [11] the Mode 2 excitation of a two-armed spiral by applying in-phase excitation to the spiral arms. This suggested the use of the two-armed spiral as a broad-band dual-mode device, a concept that proved difficult to implement practically [12] due to spurious radiation from the supporting structure. In 1966 Lantz reported [13, 14] a dual-band monopulse tracker feed using the four-armed spiral, representing one of the first uses of the four-armed spiral in an operational environment. Despite the apparent simplicity of the two-armed approach, the concept of using the four-armed spiral as a dual-mode antenna eventually superseded the idea of using the two-armed spiral for this purpose. The work presented in [12] is the most in-depth exposition of four-arm techniques available in the literature.

1.1.2 Theoretical Development

In 1955 Burdine [15] noted that radiation from a tightly-wrapped two-armed Archimedean spiral emanates from a λ-circumference region on the spiral that would become known as the active region. The radiation pattern was found to be well-approximated by a wire loop model that could be evaluated analytically. It was noted that for a two-armed Archimedean spiral there are no active regions with even-integer wavelength circumference. He also observed that the 1λ active region was the only one that provided axial radiation.

In 1957 Rumsey published his well-known mathematical analysis [16] showing that in order for an antenna to have frequency-independent properties, the antenna must take the shape of an equiangular spiral. He coined this antenna the "frequency-independent" antenna. However, even at that time there had already been many other antennas invented that exhibited the wide bandwidth of the spiral antenna, so Rumsey

coined the additional term "quasi-frequency-independent" to acknowledge those antennas. The critically important topic of Burdine's active region received relatively little attention in this paper. Since then, it has become appreciated by experts that the concept of the active region (leading to the so-called truncation principle) is of far greater practical importance than the particular shape of the antenna. Unfortunately there exist in the literature some introductions to the topic of spiral antennas that emphasize the concept of angles at the expense of the critically important truncation principle.

In 1959 Rumsey reported [17] initial results concerning theoretical work on the infinite-armed spiral antenna, with a follow-up full-length paper on the subject published in 1961 [3] and refined in [18]. This research resulted in far-field expressions for the various modes of the multi-armed spiral, as well as an expression for the phase-center location. The technique used to solve the problem formed the basis for a separate paper [19]. That same year Deschamps extended [20] Booker's extension [21] of Babinet's principle to the case of complementary multi-terminal structures, allowing the impedance of multi-armed spiral antennas to be easily computed. It also enabled relation between the "star" and "ring" modal impedances to be easily computed and used for better impedance match.

In 1963 Sivan-Sussman observed [22] that the far-field expression for the infinite-armed spiral modes matched well with the measured patterns of multi-armed spirals. The detection of higher-order modes, as would be expected from the finite-armed approximation to the infinite-armed spiral, was also reported. Connection of the spiral modes to multipole fields was done by Liang and Lo [23].

1.2 Motivation

1.2.1 Arm Coiling

A topic of perpetual interest in antenna theory and practice is that of antenna minaturization. Spiral antennas, with their extremely wide pattern and impedance bandwidths, are notoriously difficult to miniaturize without introducing unacceptable degradation in impedance, gain, pattern integrity, or axial ratio. Ways of accomplishing this miniaturization include meandering, zig-zagging, and coiling. While arm coiling has found favor with some practitioners, its effect on the performance parameters are particularly severe.

One of the goals of this thesis is to demonstrate multiarming as a way to improve the pattern integrity and axial ratio while retaining the advantages of the arm-coiling technique.

1.2.2 Electronic Attack

Until recently, electronic attack applications have focused on the 1-18 GHz radar (L through Ku) band and the 5 μm-100 nm (near-infrared through UV) band [24]. Recent developments in weapons technologies have forced extensions to this spectrum, both lower (to cover HF through UHF) and higher (to cover the K and Ka bands and beyond). In the past, additional combinations of horn antennas could be used to cover the required bandwidth; however, this becomes cumbersome as the bandwidth increases and the available platform area for antenna placement decreases. Therefore it would be useful to integrate some of these antennas into a single antenna, potentially realizing substantial savings in antenna real estate requirements.

The class of planar frequency-independent antennas in general, and the spiral antennas in particular, would seem to make excellent replacement candidates for the horn antennas currently in use. They are known to provide very large bandwidths (typically 10:1 but sometimes up to 100:1 or more) along with consistent input impedance and radiation patterns. These characteristics are unique to this class of antennas. However, in order to provide these characteristics, these antennas are typically used with an absorbing backing, since reflective cavities tend to have a detrimental effect on the input impedance and pattern bandwidths. This absorbing backing typically results in an efficiency loss of at least 50%. Worse, the absorber (typically carbon-loaded urethane foam or honeycomb) is typically a poor conductor of heat and is intolerant of high temperatures. Therefore the extraordinary measure of forced-air cooling must be taken to thermally manage the absorber. Not only is this cumbersome and expensive to implement, it may not even be sufficient or practical, for example in rarefied atmospheric environments such as high altitude or in outer space.

A major purpose of the research performed in this thesis is to determine if the absorbing cavity can be removed by appropriate use of a multi-armed spiral as the radiating element. Since this research is focused on the electronic attack application, the antennas will be excited in the broadside mode. The ultimate goal is to produce insight that will help bridge the wide performance gap that currently separates horn and spiral antennas. In the case where power handling requirements are judged too extreme for the spiral to make

a reasonable candidate with current technology, and the bandwidths are sufficiently narrow, broadbanding modifications to the horn antenna are pursued. A low-cost horn antenna is demonstrated that uses low-cost printed circuit board in its construction. The wide and azimuthally-uniform beam make it a good candidate for electronic attack applications.

1.2.3 Wideband Nulling

In electronic warfare it is often desirable to place nulls at arbitrary locations in the antenna's radiation pattern. This is true whether the antenna is being used in the transmitting electronic attack (EA) role or the receiving electronic support (ES) role. On the EA side, this can prevent attacking friendly assets. In the ES role nulling can be used to prevent jamming by hostile forces. Array antennas can be used to perform nulling; however, their bandwidth is inherently limited. On the other hand, multi-armed spiral antennas in principle have no limit on their pattern bandwidth since all beams share a similar phase center. In this sense multi-armed spirals could be the ultimate broad-band array antenna. To date there is no scholarly work that applies the multi-armed spiral antenna in this way.

1.3 Thesis Description

1.3.1 Contributions

This thesis has expanded the role of spiral antenna mode theory outside of its traditional realm of monopulse direction finding. The first application has been to mitigate the detrimental effects that an antenna miniaturization technique has on the purity of the far field. The second application is to the design of an antenna with exceptionally stable and clean radiation patterns without use of an absorbing cavity. In both of these cases multiarming is shown to be an effective way to reduce far-field modal contamination of antenna patterns. As part of this research, a simple technique for reducing the Mode 1 impedance of high arm-count spirals is shown for the first time. The third application of mode theory has been to implement wide-band radiation pattern nulling. Finally, mode theory has been used to analyze beamformer non-idealities. This has led to the revelation that the spectral distribution of beamformer errors is at least as important as the magnitude of those errors. Proper choice of beamformer topology can result in noticeable

improvement in the antenna performance. Finally, for space-constrained millimeter-wave platforms where the high-power spiral is not appropriate, a new equal-bandwidth stacked-layer horn antenna is developed. A fabrication approach based on stacked printed circuit board elements was developed for low-cost prototyping of wideband millimeter-wave antennas.

1.3.2 Organization

The data presented in this thesis is obtained from numerical simulations and measurements of fabricated articles. Two numerical simulation packages have been used in this research: EMSS **FEKO** [25] and ANSYS **HFSS** [26]. The thesis is organized as follows:

- Chapter 2 introduces the mode theory of spiral antennas. The basic operational principle of spiral antennas is reviewed before introducing Rumsey's infinite-armed spiral mode theory. Mode theory of multi-armed spiral antennas is introduced, along with the technique for evaluating modal contamination due to beamformer errors. Finally, the ring-excitation technique is used to reduce the modal impedance of high arm-count antennas.

- Chapter 3 applies the mode theory to mitigation of far-field contamination due to aggressive application of a miniaturization technique. Modal decomposition is used to gain insight into the physics of the coiled-arm spiral antenna. The mode-filtering concept introduced in Chapter 2 is used to improve the performance of this variant of the spiral antenna.

- Chapter 4 describes a spiral-helix antenna designed for high power-handling capacity capable of operating with good impedance match far below the cutoff frequency of the spiral, while retaining excellent radiation pattern characteristics.

- Chapter 5 applies mode theory to the placement of nulls in the pattern of a multi-armed spiral antenna. It is shown that wideband nulling is possible and that, in contrast to traditional array antennas, grating lobes do not appear even over extremely wide bandwidths.

- Chapter 6 describes the design of a low-cost electronic-attack antenna with an azimuthally uniform and frequency-stable radiation pattern. Agreement between simulation and measurement is excellent.

- Chapter 7 reviews the conclusions of each chapter. The thesis contributions are outlined as well as potential topics for future work.

- Appendix A introduces an algorithm developed to evaluate the phase center of spiral antennas on the full or partial pattern of the antenna. The algorithm is applied to multi-armed spiral antennas, and it is found that if the spiral arm ends are terminated properly the phase center experiences substantial stabilization. The distinct effects of various modeformer errors on the phase center are also given.

- Appendix B describes a study of an hexagonal array antenna whose constituent element is the spiral-helix of Chapter 4. Good grating-lobe-free bandwidth is demonstrated while providing an azimuthally-uniform pattern. The implications of having multi-mode-capable array element are discussed.

Chapter 2

Mode Theory of Spiral Antennas

2.1 Introduction

The research in this thesis exploits multi-armed spiral antennas to increase pattern quality and power handling, and implement wideband nulling. In-depth study and understanding of mode theory are at the core of this research, thus it is appropriate to present the necessary parts of this theory before researching the the antenna designs based on this theory.

This chapter is organized as follows. Section 2.2 introduces the spiral antenna and the so-called truncation principle that is central to the operation of all frequency-independent antennas. Next, the mode theory of the infinite-armed spiral is discussed in Section 2.3, before introducing the multi-armed spiral theory in Section 2.4. The mode-filtering concept used heavily in Chapters 3 and 4 is discussed in Section 2.5. Analysis of beamforming network errors is explained in Section 2.6, which shows that the mode distribution of beamformer errors is at least as important as the magnitude of such errors. Finally, a phenomenon that reduces the Mode 1 impedance of high arm-count spiral antennas to a practical level is discussed in Section 2.7.

2.2 Spiral Antenna Principle of Operation

A TEM mode propagating along two closely-spaced lossless parallel wires experiences little radiation attenuation, due to the presence of closely-spaced phase-opposing currents (Fig. 2.1(a)). However, if the wires are wrapped into the shape of a spiral (Fig. 2.1(b)), the currents in one wire undergo a progressive

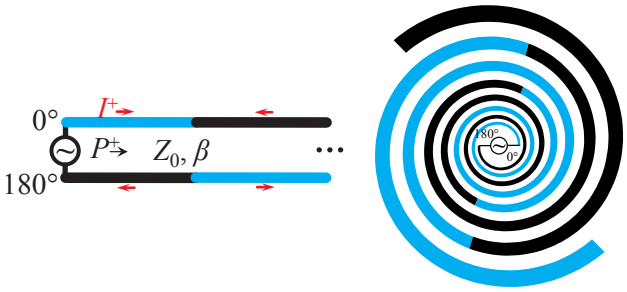

(a) Twin-lead line

(b) Two-armed spiral feeding

Figure 2.1: Evolution of the spiral antenna. (a) The twin-lead transmission line, highlighting phase-opposition of adjacent currents. (b) Center-fed two-armed spiral, highlighting adjacent-arm phase shifts.

phase shift relative to the adjacent wire. As shown in Fig. 2.2(a), the currents become completely phase-aiding in an annular-shaped region, frequently called the **active region**, with mean circumference $C_{AR} = \lambda$. From this figure it can be seen that, if the phase is sampled along the circumference of this active region, the phase will be observed to have a roughly $e^{-j\phi}$ azimuthal progression, for a total of 2π radians of phase progression around the active region. The lowest frequency at which this active region forms is $f_0 = c_0/C_{\text{spiral}}$, where c_0 is the speed of light and C_{spiral} is the spiral circumference, and is often referred to as the **cutoff frequency**. If C_{AR} is less than C_{spiral}, then the mode attenuates rapidly due to radiation, producing an RHCP upper-hemisphere pattern similar to Fig. 2.2(b). The far field radiated from this active region will be observed to share the azimuthal phase variation of the active region. Outside the active region the currents are small and the spiral may be truncated to little ill effect, a phenomenon often called the **truncation principle**. Any antenna in the frequency-independent (FI) family of antennas must have this property. If C_{AR} is greater than C_{spiral} the mode is said to be **cut off** (not to be confused with the cutoff condition of a waveguide, since radiation at reduced efficiency still occurs), and is reflected back to the feed, unless measures have been taken to absorb the mode at the outer edge of the spiral.

2.3 Mode Theory of the Infinite-Armed Spiral

Before beginning the discussion on multi-armed spiral antennas, it is important to review a special case of the multi-armed spiral that has important theoretical value. This spiral is an infinite planar sheet

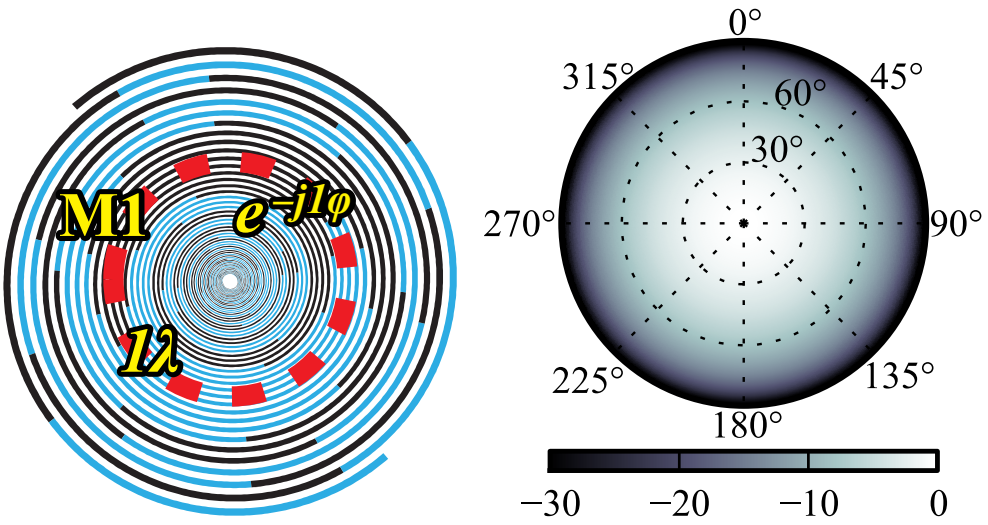

(a) Active region formation (b) Ideal RHCP pattern

Figure 2.2: Active regions on the two-armed spiral antenna. (a) Phase-aiding currents in the active region of the two-armed spiral. (b) Ideal upper-hemisphere RHCP partial (Mode 1 only) radiation pattern as derived in [3].

consisting of an infinite number of perfectly conducting spiral arms. This structure is conductive along the spiral arms, and non-conductive along the in-plane direction orthogonal to the spiral arms. This simplified model of the multi-armed spiral is valuable in that it can be analyzed as an electromagnetic boundary-value problem. Analysis of this structure was performed in [3, 27], and the pertinent results are reviewed in this section.

The far field of an antenna has the general form

$$F_E = A(\theta,\phi)e^{-j\psi(\theta,\phi)}\frac{e^{-jkr}}{r} \tag{2.1}$$

where k is the free space wavenumber, r is the radial coordinate in the spherical system (r,θ,ϕ), $A(\theta,\phi)$ is an amplitude distribution, $\psi(\theta,\phi)$ is a phase distribution, and $\frac{e^{-jkr}}{r}$ is the spherical wave function. For an infinite-armed spiral of infinite extent, the far-field amplitude and phase distributions have the form [3, 27]

$$A(\theta) = \frac{\cot\theta(\tan[\theta/2])^{|m|}e^{|m|/a\tan^{-1}(a\cos\theta)}}{\sqrt{1+a^2\cos^2\theta}} \qquad (\text{any } m \neq 0) \tag{2.2}$$

and

$$\psi(\theta,\phi) = m\phi + \text{ terms in } a \text{ and } \theta \tag{2.3}$$

Where a is the spiral growth rate. In the terminology of [22], m = integer is the **mode number** and the resulting field constitutes a **mode** of the spiral antenna. Such a mode has the following features:

(1) For any constant angle off broadside θ the phase advances linearly by $2\pi m$ as the azimuth ϕ is swept from 0 to 2π.

(2) The far field is circularly polarized with the sense of polarization dependent on the sign of m.

(3) All modes with $|m| \neq 1$ have nulls at broadside.

(4) The far field has zero magnitude in the plane of the spiral.

(5) For small a the phase center of each mode is located approximately a radians behind the spiral aperture.

The upper-hemisphere RHCP amplitude distributions, normalized with respect to their corresponding maximum values, for various modes are shown in Fig. 2.3. As seen, the Mode 1 (M1) pattern is the only one with broadside radiation.

Despite being strictly applicable only to the infinite-armed spiral of infinite spatial extent, these modes are sufficient to accurately describe the operation of spirals that possess a finite number of arms [22], provided that the arms are excited with equal amplitude and with progressive phases $m2\pi n/N$. Here N is the number of arms and $n = (0, 1, \ldots, N-1)$ is the arm number. Since an arbitrary excitation can be represented as a weighted sum of terms with this form, the operation of spiral antennas is often described in terms of this so-called spiral mode theory. In this chapter the far-field performance of spiral antennas is described on the fundamental level in terms of these spiral modes.

Additionally, it has been noted that each mode radiates from an active region on the spiral with circumference $C_{AR} = |m|\lambda$ (Fig. 2.4) [12]. As with the two-armed spiral, when the spiral circumference C_{spiral} is greater than $|m|\lambda$, the current decays rapidly as it travels through this region. When the spiral circumference is less than $|m|\lambda$ the spiral is once said to be "in cutoff". When the spiral is in cutoff, the outward traveling Mode m has not decayed by the radiation mechanism, and instead a reflected mode with index $m - N$ is produced, which propagates inward. The energy is radiated by the aperture if C_{spiral} is large

enough; otherwise, it continues to the feed and forms a standing wave. If radiated, the energy radiated by this spurious mode is predominantly cross-polarized to the desired mode.

For any given far field it is possible to decompose each field component with respect to azimuth using the integral [28]

$$E_m(\theta) = \frac{1}{2\pi}\int_0^{2\pi} E(\theta,\phi)e^{jm\phi}d\phi \tag{2.4}$$

where E is a given vector component of the far field (e.g. θ, ϕ, RHCP, or LHCP), and E_m is the mode field. While this expression obviously yields Fourier series coefficients, this procedure also resembles the partial (azimuthal) decomposition of a field into spherical modes, and therefore the term **modal decomposition** is often used to describe the procedure. We call the entire collection of mode fields the **modal content**, and any undesired mode fields the **modal contamination.** The corresponding E_m remains associated with that vector component, so that various interpretations of the modes in terms of polarization are possible. Due to the $e^{jm2\pi n/N}$-type excitation typically applied to spirals, the fields associated with the desired mode will often dominate all other terms. This efficiency of representation makes these mode fields practical for performing analysis of far-field errors. The analysis of Chapter 3 makes frequent use of this technique to gain insight into physical processes affecting the far field.

In addition to their use in pattern analysis, the procedure is used to analyze errors in the beam-forming network (BFN). Often such analysis reveals that a particular component of the BFN error is responsible for a given far-field parameter of interest (e.g. axial ratio (AR)). The technique is used in the BFN analysis of Chapter 3.

2.4 Multi-Armed Spiral Antenna Theory

The research in this thesis draws heavily on the mode theory of multi-armed spiral antennas comprehensively treated in [12]. Throughout this work we assume the spiral is planar, self-complementary, and has a right-handed wrap with respect to the z coordinate axis (which is normal to the spiral aperture). For a left-handed wrap the theory is essentially the same, except that the polarization and modal phase progression senses are reversed. It is also assumed the spiral is center-fed from an electrically small feed region so that circuit-theoretical concepts such as Kirchhoff's current law are applicable.

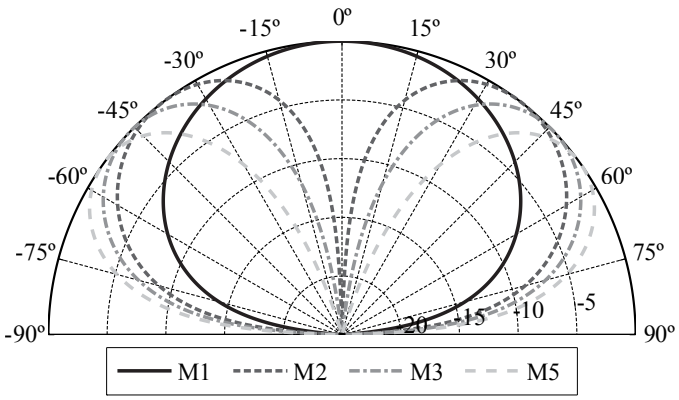

Figure 2.3: Angle off broadside patterns for various spiral modes computed using (2.2) and normalized to the pattern maximum. Note that all modes except for Mode ±1 have nulls at broadside.

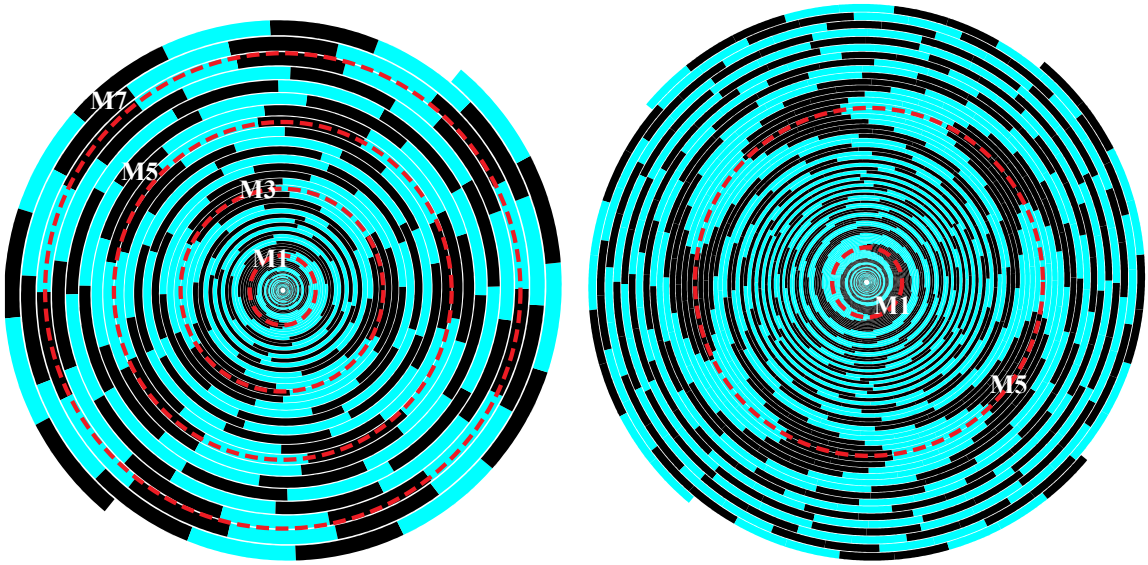

(a) Two-armed (b) Four-armed

Figure 2.4: Instantaneous phase distribution on Mode 1-excited two- and four-armed smooth (non-coiled) spiral apertures, showing positive (lightly-shaded) and negative (darkly-shaded) phase. The active regions are highlighted with their corresponding mode indices, demonstrating the superior mode-rejection of the four-armed spiral.

2.4.1 Excitation

In contrast to the two-armed spiral, where only one balanced excitation exists, multi-armed spirals can be excited in numerous ways. However, for the present discussion excitations that excite only a single active region at a time are chosen. A special set of excitations, corresponding to eigenvectors of the multi-armed spiral's impedance matrix [12, 20], are the excitations that produce this desirable condition. These modes,

Table 2.1: Fundamental spiral modes of a four-armed spiral with their amplitude and phase excitations

Mode	Arm Number			
	1	2	3	4
0	$1\angle 0°$	$1\angle 0°$	$1\angle 0°$	$1\angle 0°$
1	$1\angle 0°$	$1\angle -90°$	$1\angle 180°$	$1\angle 90°$
2	$1\angle 0°$	$1\angle 180°$	$1\angle 0°$	$1\angle 180°$
3	$1\angle 0°$	$1\angle 90°$	$1\angle 180°$	$1\angle -90°$

called **spiral modes** [12], are summarized in Table 2.1 for the case of the four-armed spiral. In the general case, the spiral Mode m excitation of the n-th arm is given by [12]

$$V_m^n = e^{-j2\pi m(n-1)/N} \tag{2.5}$$

where the arm numbering is in accordance with the right-hand rule with respect to the z axis (Fig. 2.5).

It is worth noting that spiral Mode 0 has some unique characteristics compared to other spiral modes. First, the spiral Mode 0 is an unbalanced mode, and will be rejected at the feed due to Kirchhoff's current law unless there is an extra conductor present to carry the return current. Typically the extra conductor is provided by the antenna feed structure, such as the outer shield of the coaxial cable bundle [29]. Since the feed structure cannot produce frequency-independent radiation, the quality of the impedance and far-field pattern is seldom acceptable when wide-bandwidth operation is required. For this reason, this thesis will make no further consideration of spiral Mode 0.

In addition to exciting only one active region per mode, the spiral mode excitations have the additional convenient property that the spiral mode excitations are related to the arm excitations by the discrete Fourier transform (DFT). As an example, for spiral Mode 1 there is the transformation

$$[1\angle 0° \quad 1\angle -90° \quad 1\angle 180° \quad 1\angle 90°]^T \xrightarrow{\text{IDFT}} [0 \quad 1 \quad 0 \quad 0]^T \tag{2.6}$$

Thus the inverse DFT transforms from the "arm" domain vector (LHS) to the "spiral mode" domain vector (RHS), in this example producing an output in the second (Mode 1) element of the spiral mode vector. This property is useful in analyzing spiral beamforming errors [4, 12, 30], and is utilized later to determine the required arm excitations for a given superposition of spiral modes.

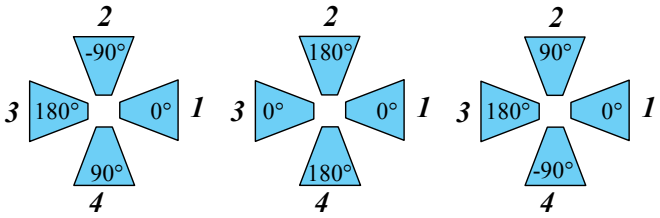

(a) Mode 1 (b) Mode 2 (c) Mode 3

Figure 2.5: Spiral-mode arm phasings for a four-armed spiral. The z direction is out of the page.

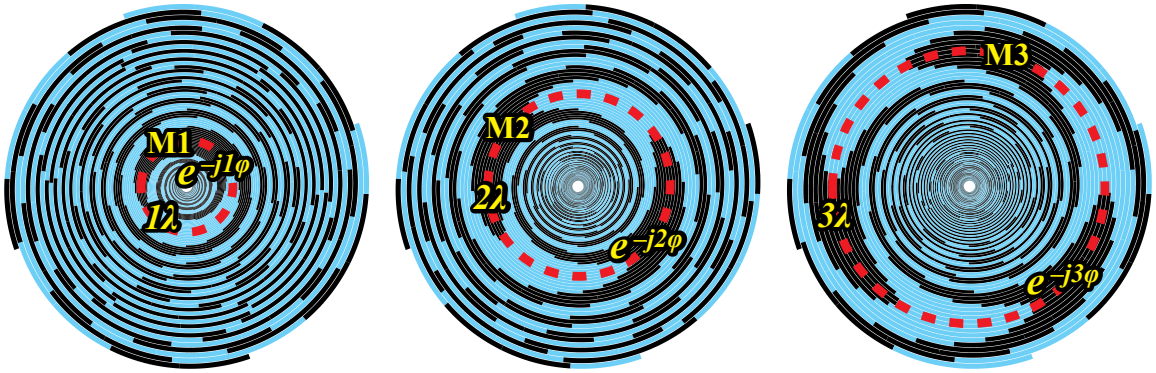

(a) Mode 1 (b) Mode 2 (c) Mode 3

Figure 2.6: Fundamental active regions of the four-armed spiral.

2.4.2 Active Regions and Patterns

Fig. 2.6 shows the active regions for the four-armed spiral, excited as in Fig. 2.5. As in the infinite-armed case, the circumference of the active region C_{AR} is determined by the mode of excitation, and is equal to $|m|\lambda$, where m is an integer corresponding to the spiral mode index and λ is the wavelength. Analogously to the two-armed spiral, the phase in the active region varies by $e^{-jm\phi}$, for a total phase progression around the active region of $2\pi m$. The shape of the resulting far-field patterns for the four-armed spiral is shown in Fig. 2.7, which closely agree with the patterns in Fig. 2.3. In the general N-armed case, Mode 1 has a broadside pattern, while all higher-order modes have conical beams that become more depressed toward horizon with increasing mode index.

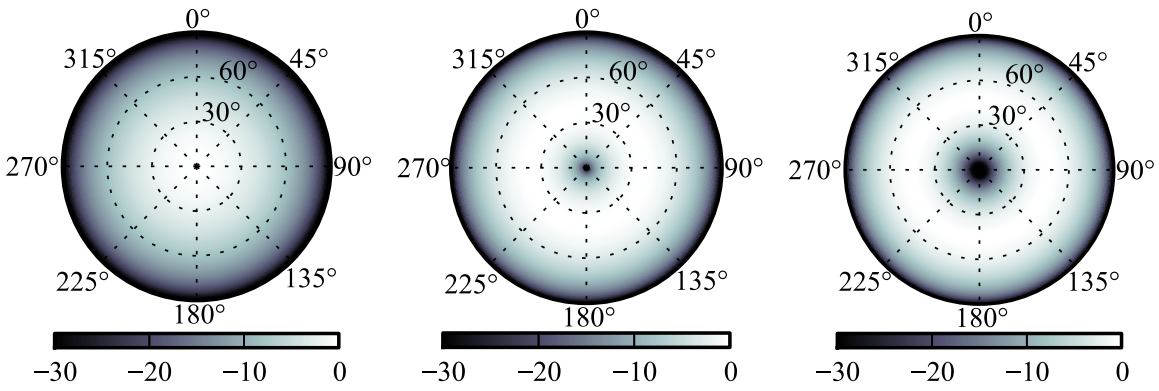

(a) Mode 1 (b) Mode 2 (c) Mode 3

Figure 2.7: Ideal upper-hemisphere RHCP partial far field patterns corresponding to the fundamental active regions of the four-armed spiral.

2.4.3 Fundamental and Higher-Order Active Regions

For clarity, only the "fundamental" active regions from which the majority of radiation takes place have been examined up to this point. However, some residual energy will not radiate from these active regions; instead, it will continue to propagate outward along the spiral. The precise amount of residual energy is dependent on many factors, including metal-to-slot (M/S) ratio, wrap rate, feed imbalances, and material loading just to name a few. In addition to the fundamental active region for a given mode there are "higher-order" active regions from which radiation can occur. An N-armed spiral excited in Mode m can radiate from higher-order active regions of circumference

$$(m + \kappa N)\lambda, \quad \kappa = \pm 1, \pm 2, ... \tag{2.7}$$

if the circumference of the spiral is large enough to support that active region. The active regions excited by each mode in the four-armed case are shown in Table 2.2. From Fig. 2.8 one can visualize the excitation sequence of the outward-traveling mode, with the positive active regions (Fig. 2.8(a)) radiating in increasing order. When a discontinuity is encountered, such as the end of the spiral arms, the energy is reflected back toward the feed. The phase progression of the reflected wave is opposite that of outward-traveling wave, and so the negative active regions are excited (Fig. 2.8(b)), with the largest-circumference supported active region radiating first. The total pattern is the superposition of the partial patterns associated with each radiating active region.

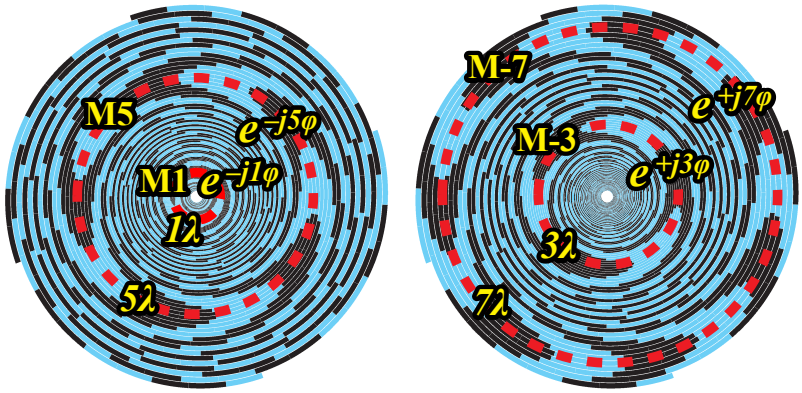

(a) Outward-traveling (b) Inward-traveling

Figure 2.8: The sequence of higher-order active region excitation, for a center-fed four-armed spiral. The active region excitation sequence in this example is $1 \rightarrow 5 \rightarrow -7 \rightarrow -3$.

2.4.4 Modal Decomposition and Mode Patterns

In the same way that a given multi-armed spiral excitation can be decomposed into its constituent spiral modes using the DFT, a given far field can be decomposed into its constituent phase modes [28, 31] by applying the Fourier series decomposition

$$F_\nu(\theta) = 1/2\pi \int_0^{2\pi} F(\theta,\phi) e^{j\nu\phi} d\phi \tag{2.8}$$

where $F_\nu(\theta)$ is the ν-th phase mode, ϕ is the azimuth variable, and θ is the angle off broadside. This decomposition serves to isolate the contributions of the individual active regions with phase progression $e^{-j\nu\phi}$, whose patterns may then be examined individually. Given this decomposition, the total far field is

$$F(\theta,\phi) = \sum_{\nu=-\infty}^{\infty} F_\nu(\theta) e^{-j\nu\phi} \tag{2.9}$$

where the summation over ν may be truncated after a sufficient number of terms. One typical application of this procedure is to evaluate the effects on the pattern asymmetry due to antenna fabrication errors [32]. Herein this information is instead used to assemble the m-th mode pattern of the antenna,

$$F_m(\theta,\phi) = \sum_{\kappa=-\infty}^{\infty} F_{m+\kappa N}(\theta) e^{-j(m+\kappa N)\phi} \tag{2.10}$$

by superimposing like terms according to the fundamental and higher-order active regions of (2.7). Sample mode patterns are shown in Fig. 2.9. Finally, the total pattern is obtained by summing over the $N-1$

Table 2.2: Active regions excited by various modes of the four-armed spiral

Spiral Mode	Active Regions[a]
1	$..., -7, -3, \mathbf{1}, 5, 9, ...$
2	$..., -6, -2, \mathbf{2}, 6, 10, ...$
3	$..., -5, -1, \mathbf{3}, 7, 11, ...$

[a] The fundamental active region is shown in bold.

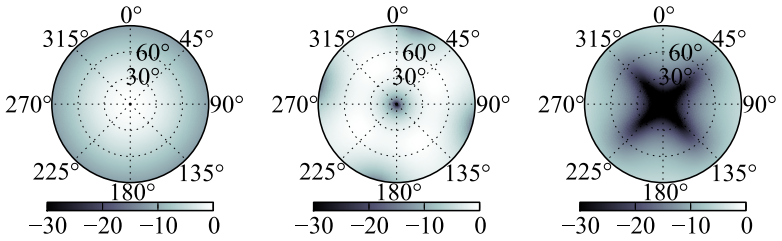

(a) Mode Pattern 1 (b) Mode Pattern 2 (c) Mode Pattern 3

Figure 2.9: **FEKO**-simulated upper-hemisphere RHCP partial mode patterns at $2f_0$ for a four-armed spiral with growth rate $a = 0.062$/rad. Non-ideal pattern undulations are due to interference among fundamental and higher-order active regions.

admissible spiral modes

$$F(\theta, \phi) = \sum_{m=1}^{N-1} \sum_{\kappa=-\infty}^{\infty} F_{m+\kappa N}(\theta) e^{-j(m+\kappa N)\phi} \tag{2.11}$$

2.5 Mode Filtering

If an outward-traveling $m = 1$ pattern with perfect circular polarization at boresight is desired, then the inward-traveling Mode $m = -1$ must be eliminated. On a two-armed spiral this is accomplished by resistively terminating the spiral arms, thereby preventing the $m = -1$ mode from reflecting from the spiral ends and propagating inward. This strategy is often difficult to implement satisfactorily, especially when the spiral is near its cutoff frequency $f_0 = c_0/C$, where c_0 is the speed of light and C is the circumference.

Alternatively, one can exploit the fact that a symmetric four-armed aperture does not radiate Mode $m = -1$ when supplied with a Mode $m = 1$ excitation. This property ensures that the boresight cross-

polarization will be limited only by the quality of the beam-forming network (BFN) and the symmetry of construction. Compared to the two-armed spiral, the four- and eight-armed structures will also have much better purity of the radiated far-field (see Fig. 2.10).

2.5.1 Improving Far-Field Characteristics of Metal-Backed Spiral Antennas

Due to the planar nature of the planar spiral antenna, about half of the radiated power is directed in the backward direction; however, in most applications a unidirectional radiation pattern is required. In this case, absorbing material is placed on one side of the spiral to terminate this radiated power. This accomplishes the desired effect; however, about half of the radiated power is dissipated in the absorber when the spiral is used in an exciter application. This dissipated power could be a liability if removing the excess heat from the cavity increases the size, weight, or cost of the antenna.

For these reasons it is desirable to instead use a cavity made of reflecting material, the most obvious initial choice being a metal ground plane placed below the plane of the spiral. If a center-fed spiral with outward-traveling currents is used, then by image theory the "image spiral" will have oppositely-signed outward-traveling currents. Described in terms of spiral modes, a spiral excited in Mode N will have an image spiral that is also excited in Mode N, but with currents of opposite sign. At low frequencies the modes from the two spirals interfere destructively, resulting in greatly reduced gain. As frequency increases, the delay introduced by the physical separation of the spirals becomes significant so that the gain is enhanced, reaching a maximum when the cavity depth d becomes $\lambda/4$.

2.5.1.1 3-D Radiation Patterns

Spiral antennas with two and four arms were modeled in **FEKO**, placed 2 cm above infinite perfectly electrically conducting (PEC) planes. The 3-D radiation patterns are plotted in Fig. 2.11, and highlight the relative pattern uniformity of the two- and four-armed spirals. The two-armed spiral exhibits significant azimuthal gain non-uniformity (Wobble-on-Wave (WoW)) at all frequencies, becoming catastrophic at 2000 MHz. By contrast, the four-armed spirals pattern has a high degree of azimuthal uniformity at lower frequencies, and while by 2000 MHz the pattern has degraded due to Mode $m = 5$ contamination, it has done

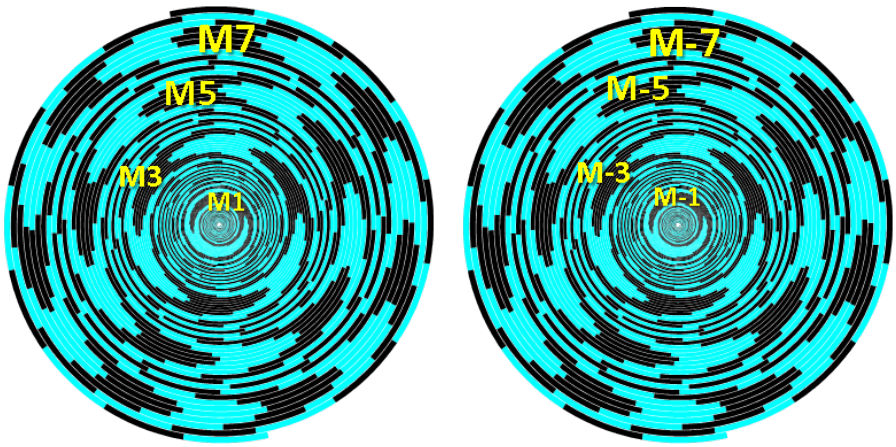

(a) Two Arms: Outward

(b) Two Arms: Inward

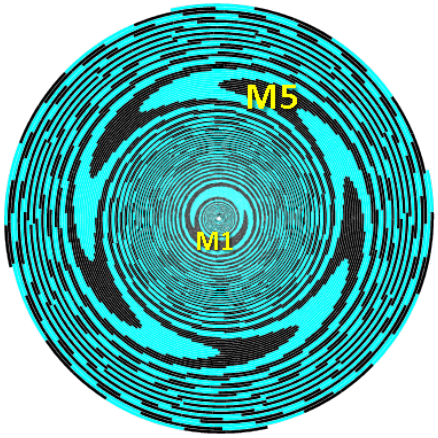

(c) Four Arms: Outward

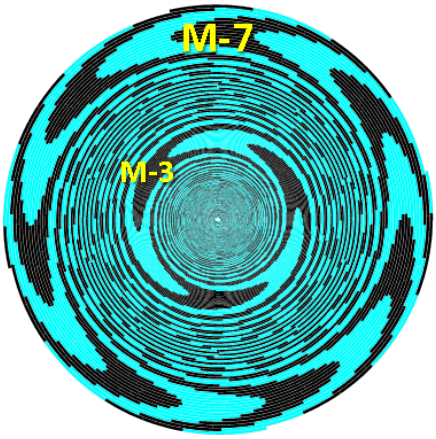

(d) Four Arms: Inward

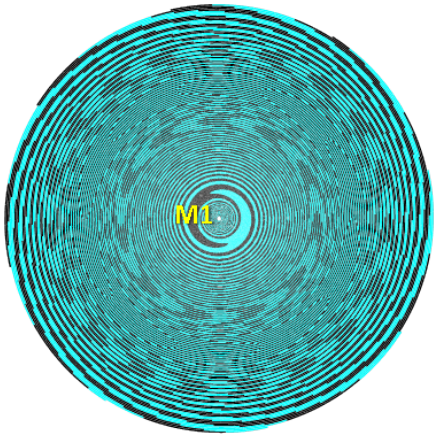

(e) Eight Arms: Outward

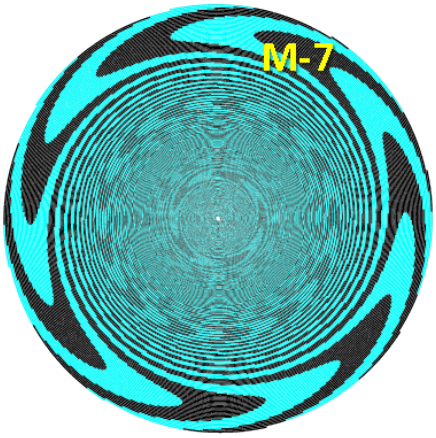

(f) Eight Arms: Inward

Figure 2.10: Comparison of the mode-filtering properties of the two-, four-, and eight-armed spiral apertures. The eight-armed spiral radiates the fewest modes compared to the two- and four-armed spirals, and therefore has a cleaner pattern.

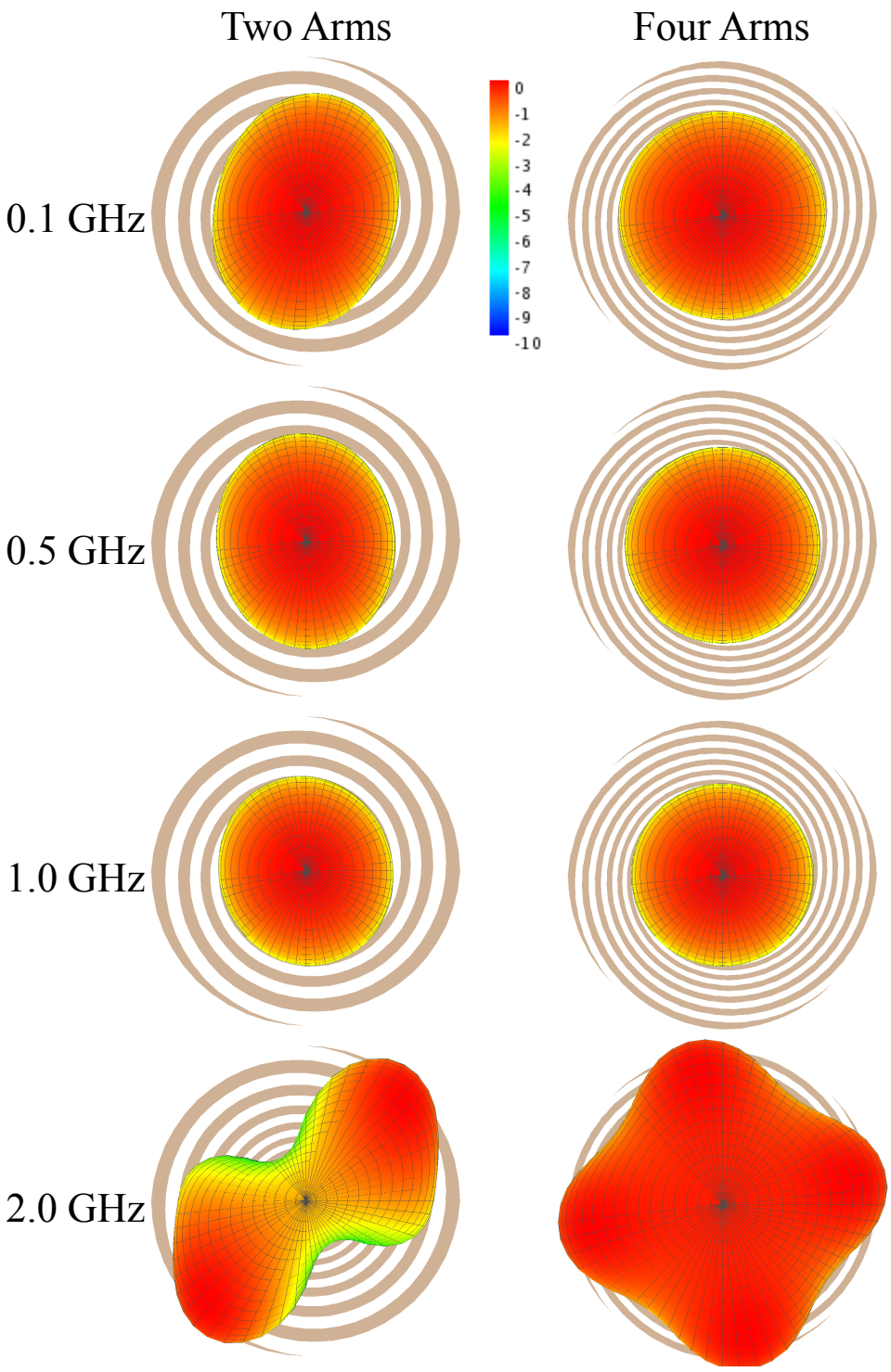

Figure 2.11: Three-dimensional co-polarized gain patterns for 15 cm diameter two-armed and four-armed spiral ($a \approx 0.06$/rad) antennas 2 cm above a PEC plane, as viewed from broadside at several frequencies.

so in a far more graceful way.

2.5.1.2 3-dB Beamwidth

As noted previously, the far field of the two-armed spiral at low frequencies resembles that of a horizontal dipole, with correspondingly poor azimuthal beamwidth variation. In the metal-backed case, however, the fields of the physical spiral and the image spiral interfere to produce a gain null in the plane of the antenna. This reduces the low-frequency beamwidth variation significantly in the case of the two-armed spiral. However, the metal ground plane has introduced a variation in the beamwidth that has a period of approximately 400 MHz (Fig. 2.12(a)). Once again it can be seen that the azimuthal beamwidth variation is still reduced by increasing the number of spiral arms. In fact, the azimuthal beamwidth variation is less than ±3°. Here we can see that the co-polarized 3 dB beamwidth for all spirals is significantly affected.

2.5.1.3 Wobble-on-Wave (WoW)

Fig. 2.12(b) highlights the improvement in azimuthal gain variation that can be realized with the four-armed spiral. The improvement can be attributed to the fact that the first spurious mode for the two-armed spiral is Mode 3, while the first spurious mode for the four-armed spiral is Mode 5. Since the metal plane reduces the radiation efficiency of Mode 1, there is more power available to be radiated in the spurious modes.

2.5.1.4 Axial Ratio

Fig. 2.12(c) shows the benefits that multiarming has on the axial ratio. For the two-armed spiral the contamination from Mode -1 is very large at low frequencies as expected, but fails to reach an acceptable level at higher frequencies because the reduced efficiency of Mode 1 ensures that there is significant power available to Mode -1 and higher modes. Since the four-armed spiral does not radiate Mode -1, the cross-polarization contamination does not begin until much higher frequencies.

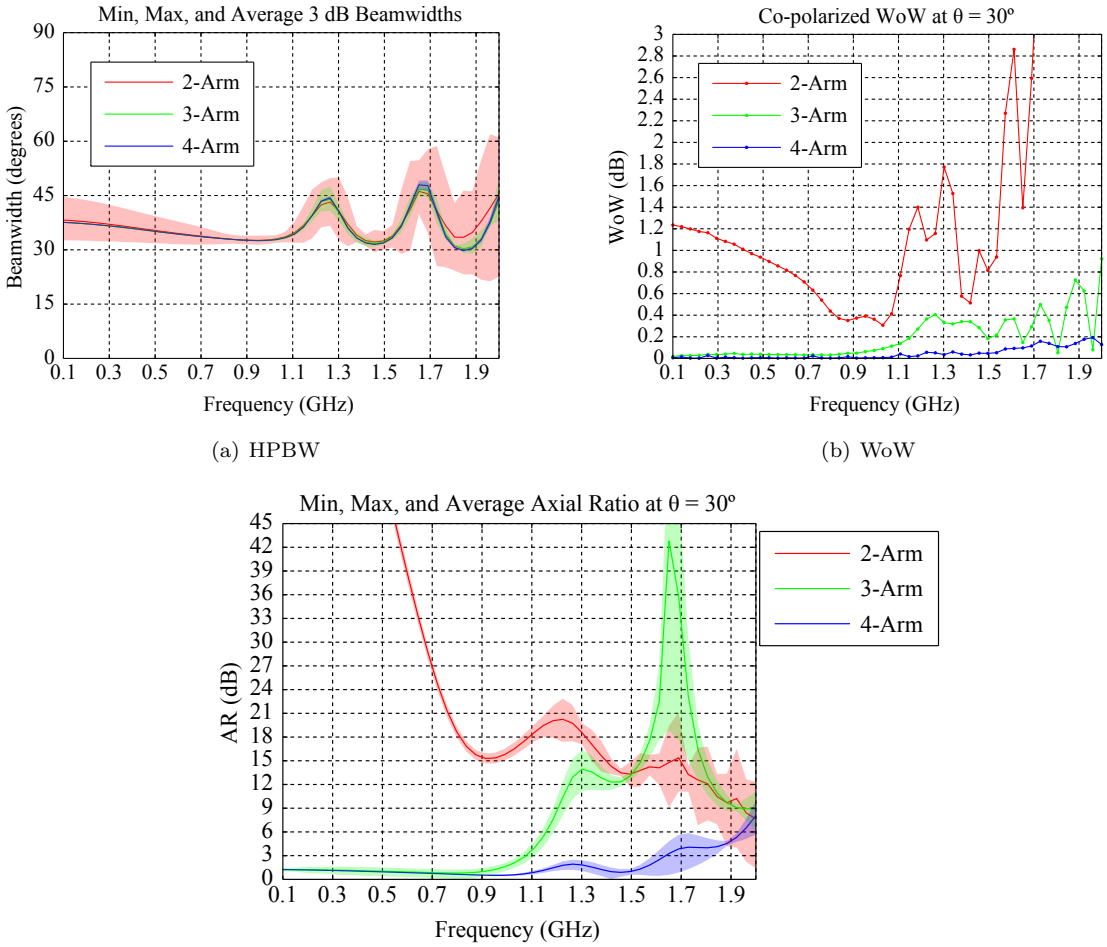

(a) HPBW

(b) WoW

(c) Axial Ratio

Figure 2.12: (a) Co-polarized minimum, maximum, and average 3-dB beamwidths vs. frequency for the spirals shown in Fig. 2.11 plus a three-armed variant. Shaded regions indicate the boundaries of the minimum and maximum beamwidth, and solid lines indicate the average value. (b) Azimuthal pattern nonuniformity (WoW) versus frequency. The four-armed spiral has a very low amount of pattern uniformity degradation at higher frequencies. (c) Minimum, maximum, and average axial ratio at a angle off broadside of 30°. The four-armed spiral shows the best performance.

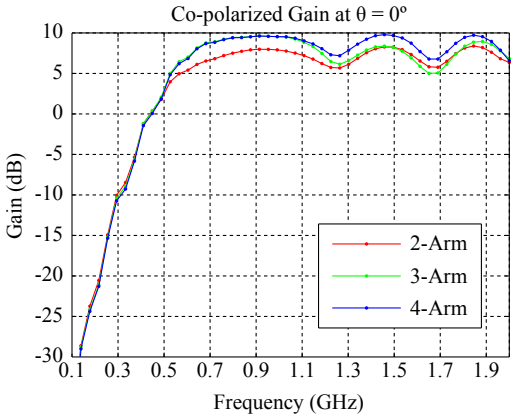

(a) Broadside Gain

Figure 2.13: (b) Co-polarized gain at broadside versus frequency for the two- and four-armed spirals shown in Fig. 2.11 plus a three-armed variant. The four-armed spiral shows the best performance across most of the frequency range.

2.5.1.5 Gain

As explained previously, the broadside co-polarized gain (Fig. 2.13(a)) suffers for spiral antennas that are in the presence of a metal plane placed close to the spiral. However, as frequency increases the gain improves substantially. The gain for the two-armed spiral is lower than the four-armed spiral because the contamination from Mode -1 has "robbed" some of the radiated power from the desired mode. The co-polarized gain for the three-armed spiral starts out the same as for the four-armed spiral, then decreases to that of the two-armed spiral because of contamination from Mode -3. Quantitatively, the co-polarized gain at 300 MHz is about 8 dB lower with the reflective backing present than without. For the two-armed spiral, the gain enhancement at 900 MHz is about 4 dB with the reflective backing present, while the four-armed spiral gets about 6 dB gain improvement.

2.6 Beamforming Network Error Analysis

A classical application of spiral antennas is as the receiving element in monopulse direction finding systems. In this application a multi-armed spiral is used to sense two or more orthogonal modes simultaneously. A modeformer connected to the antenna is used to decompose the received energy into its various spiral modes, directing each mode to a separate port. Beamforming circuitry then compares the amplitudes

and phases of the mode outputs to produce the azimuth and elevation of a target. Fundamental to the accuracy of the direction finding is the level of modal cross-contamination, which occurs when a portion of the energy from one mode is cross-coupled to another spiral mode. As a consequence the far-field amplitude and phase envelopes of desired modes experience undulations which deteriorate system accuracy. One major source of this contamination is the modeformer, which is typically constructed from either lumped or distributed circuit elements. Often this modeformer must operate over bandwidths in excess of a decade while maintaining acceptable amplitude and phase balance.

In this section we quantify the effects that modeformer amplitude and phase deviations have on various far-field performance characteristics of two-, four-, and eight-armed spiral antennas. Specifically, we evaluate azimuthal gain variation (WoW), axial ratio, and cross-modal difference. It is shown in Chapter 3 that the far-field contamination associated with realistic amplitude and phase misbalances of single-mode, multi-armed spiral modeformers is acceptable. In other words, multi-armed spirals with realistic beamformers maintain superior beam symmetry and overall far-field quality when compared with simpler two-arm spirals fed with ideal amplitude and phase balance.

2.6.1 Modal Analysis of Modeformer Outputs

An arbitrary voltage excitation of a four-armed spiral can be represented in the frequency domain as the complex vector

$$V_A = \begin{bmatrix} V_{A1}e^{j\phi_{A1}} & V_{A2}e^{j\phi_{A2}} & V_{A3}e^{j\phi_{A3}} & V_{A4}e^{j\phi_{A4}} \end{bmatrix}^T \tag{2.12}$$

If the spiral is oriented with its normal along the z axis, then it is convenient to number the excitations so that the numbering increases in the counterclockwise direction around the z axis. One can decompose this vector using the discrete Fourier transform into its so-called spiral modes

$$V_M = \begin{bmatrix} V_{M1}e^{j\phi_{M1}} & V_{M2}e^{j\phi_{M2}} & V_{M3}e^{j\phi_{M3}} & V_{M4}e^{j\phi_{M4}} \end{bmatrix}^T \tag{2.13}$$

The correspondences between the arm excitations and the spiral modes are

$$\begin{bmatrix} e^{-j0} & e^{-j0} & e^{-j0} & e^{-j0} \end{bmatrix}^T \xrightarrow{\text{IDFT}} \begin{bmatrix} 1 & 0 & 0 & 0 \end{bmatrix}^T \quad \text{(Mode 0)} \tag{2.14}$$

$$\begin{bmatrix} e^{-j0} & e^{-j\pi/2} & e^{-j\pi} & e^{-j3\pi/2} \end{bmatrix}^T \xrightarrow{\text{IDFT}} \begin{bmatrix} 0 & 1 & 0 & 0 \end{bmatrix}^T \quad \text{(Mode 1)} \tag{2.15}$$

$$\begin{bmatrix} e^{-j0} & e^{-j\pi} & e^{-j0} & e^{-j\pi} \end{bmatrix}^T \xrightarrow{\text{IDFT}} \begin{bmatrix} 0 & 0 & 1 & 0 \end{bmatrix}^T \quad \text{(Mode 2)} \tag{2.16}$$

$$\begin{bmatrix} e^{-j0} & e^{-j3\pi/2} & e^{-j\pi} & e^{-j\pi/2} \end{bmatrix}^T \xrightarrow{\text{IDFT}} \begin{bmatrix} 0 & 0 & 0 & 1 \end{bmatrix}^T \quad \text{(Mode 3)} \tag{2.17}$$

The extension to different arm counts is straightforward.

An example of a simple modeforming circuit described in [4] is shown in Fig. 2.14, where the 90° hybrid is realized using the QS2-01-464 (500-1000 MHz bandwidth, 100 W power handling) from Pulsar Microwave, and the 180° hybrids are realized using the JT-06-411 (20-1000 MHz bandwidth, 1 W power handling) from the same manufacturer. Figs. 2.15(a) and 2.15(b) show, respectively, the worst-case magnitude and phase mismatch of the modeformer shown in Fig. 2.14. However, this information alone fails to provide adequate insight into the potential consequences for the performance of the modeformer/antenna system. A more complete picture is formed by decomposing the modeformer outputs into the constituent modes. Fig. 2.16 shows the mode isolation (i.e. cross-modal difference (CMD)) for the above modeformer, and it is apparent that Mode 3 will be the dominant spurious mode below 500 MHz, the lowest designed operating frequency of the modeformer.

Fig. 2.17 shows the three (two-, four-, and eight-armed spirals with a = 0.62/rad) structures used in the evaluation. Fig. 2.18 shows the corresponding axial ratio of ideal modeformed spirals. The two-armed spiral has poor axial ratio up until approximately $2f_0$, and also beyond $10f_0$. The poor performance of the two-armed spiral below $2f_0$ is due to superposition of Mode -1 on the dominant Mode 1 pattern from reflection off of the arm ends. The high axial ratio above $10f_0$ is caused by the bowtie-shaped feed region, which does not discriminate between Mode 1 and Mode -1. Therefore both modes are radiated in equal measure, resulting in a linearly-polarized field. In contrast, the four- and eight-armed spirals, despite also having bowtie (or perhaps more correctly, turnstile)-shaped feed regions, do not suffer this degradation.

Fig. 2.19 shows the axial ratio in the separate cases of Mode 2 and Mode 3 contamination. Very little

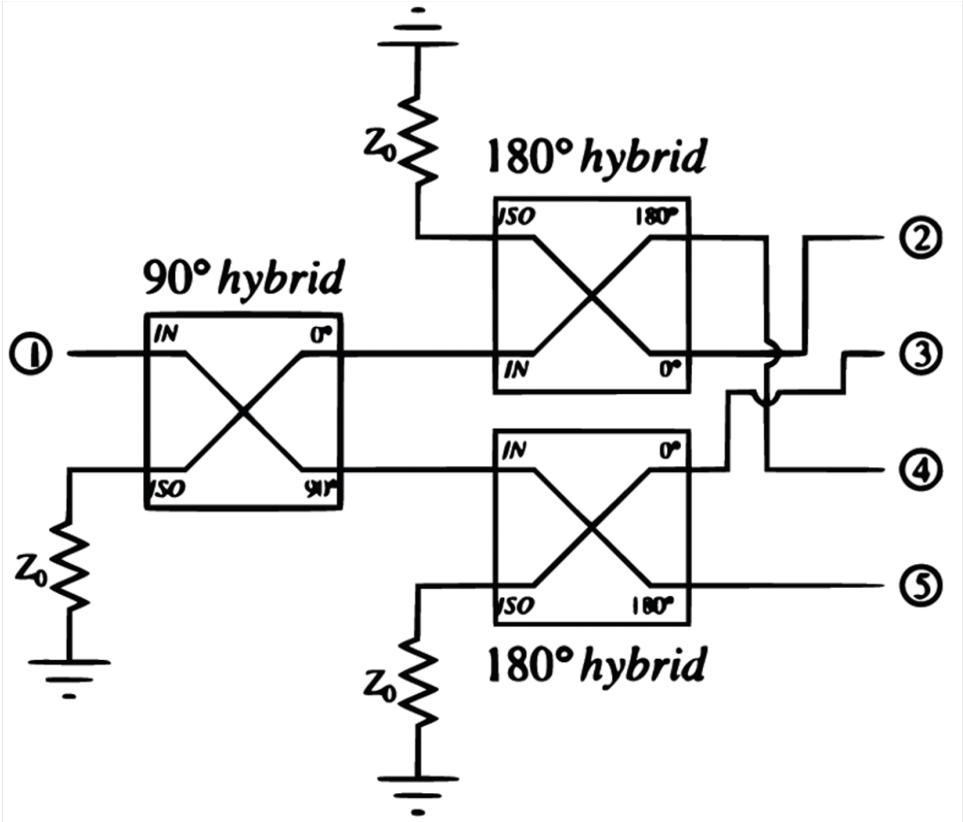

Figure 2.14: A simple Mode 1 modeforming circuit from [4].

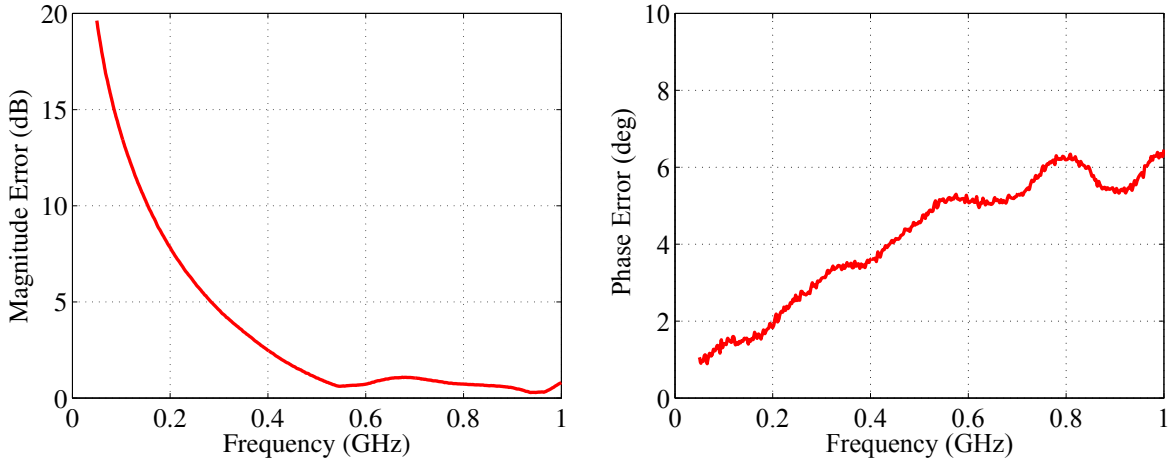

(a) Magnitude

(b) Phase

Figure 2.15: Worst-case arm-to-arm magnitude and phase error of the modeformer in Fig. 2.14. The BFN's rated bandwidth is 0.5-1 GHz.

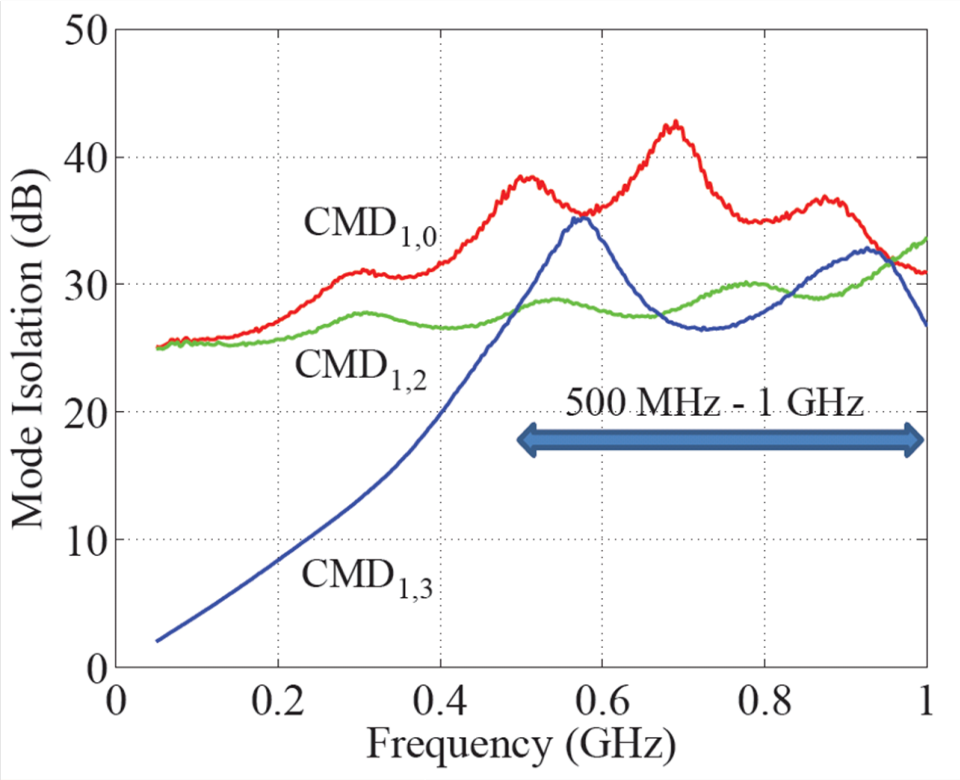

Figure 2.16: Mode isolation of the modeformer in Fig. 2.14.

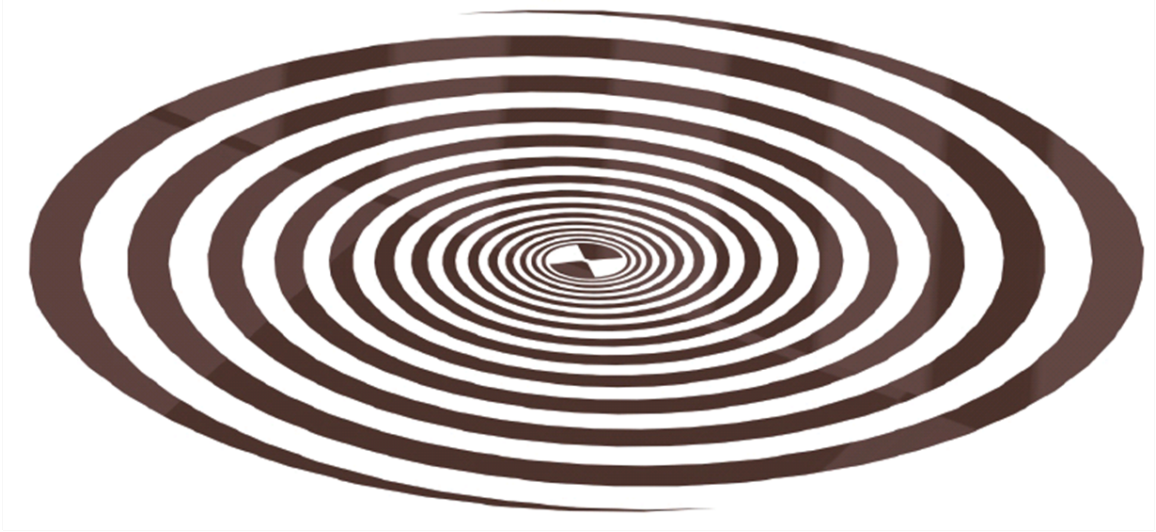

(a) Two Arms

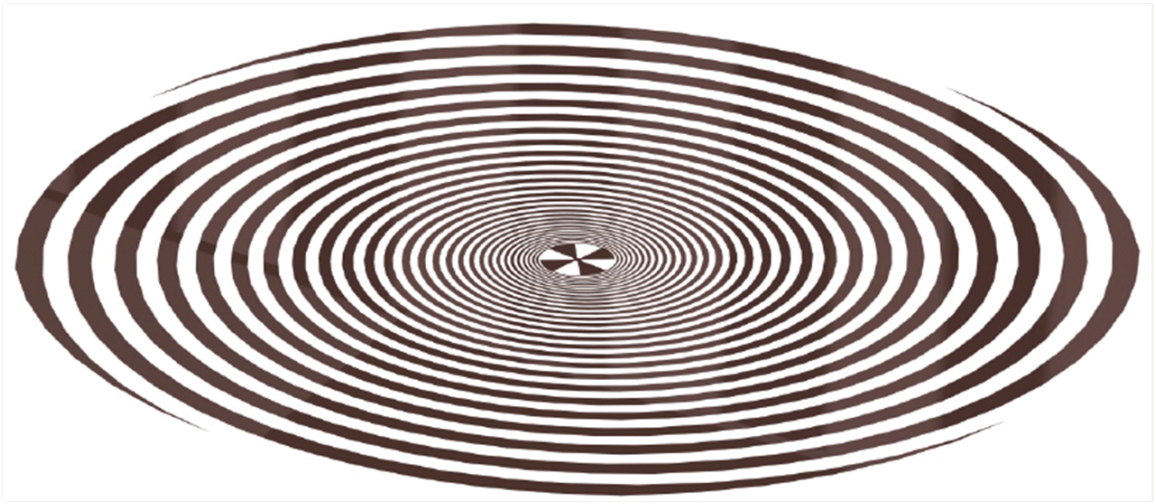

(b) Four Arms

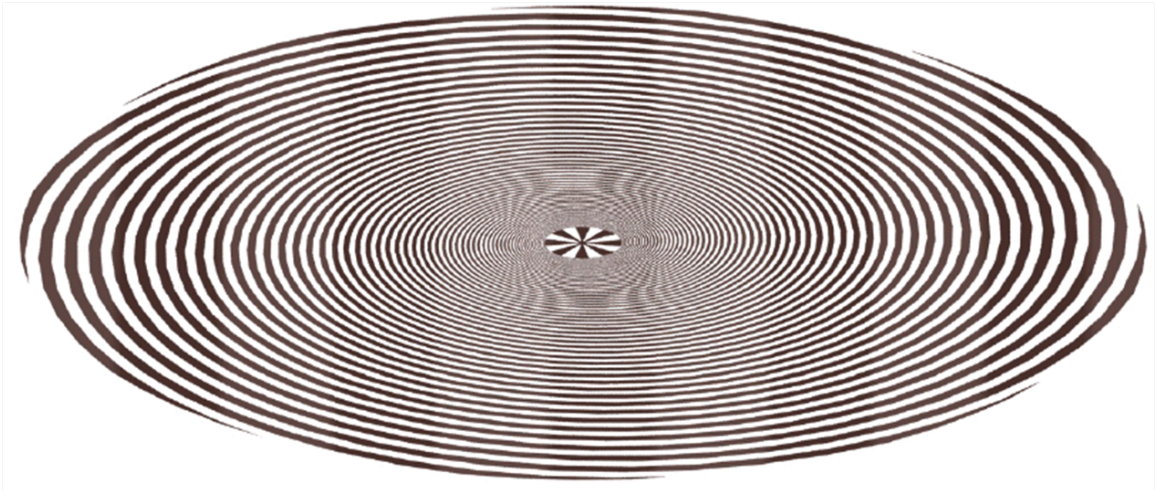

(c) Eight Arms

Figure 2.17: Spiral apertures (15.24 cm diameter, a = 0.62/rad) in free space used to evaluate the effects of mode contamination.

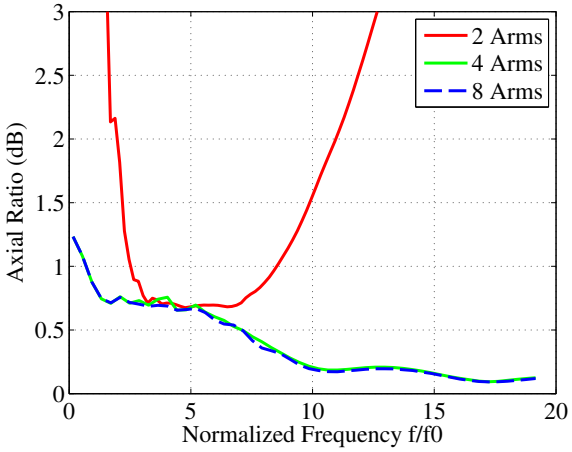

Figure 2.18: Average axial ratio at 30° from broadside of two-, four-, and eight-armed spiral antennas with an ideal modeforming network.

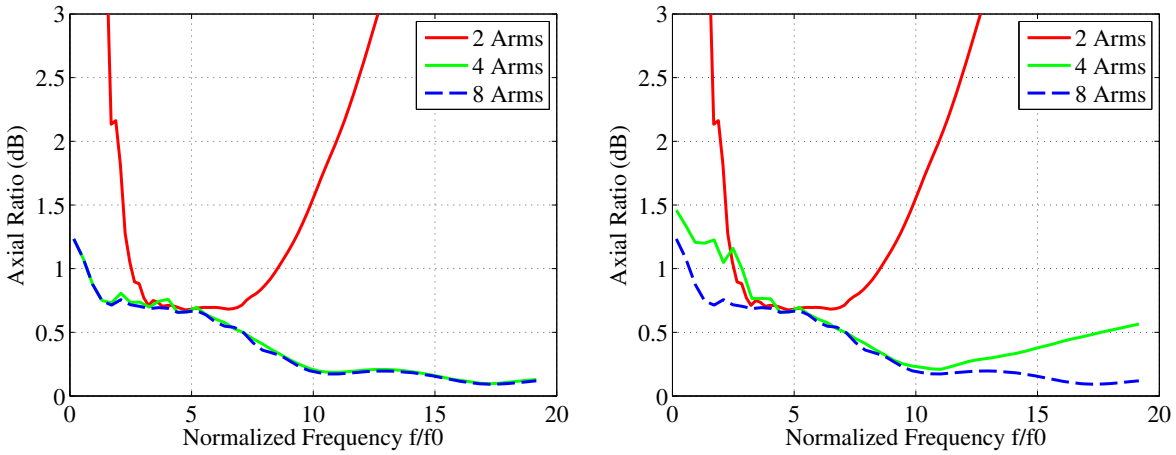

(a) Mode 2

(b) Mode 3

Figure 2.19: Average axial ratio at 30° from broadside of two-, four-, and eight-armed spiral antennas with Mode 2 and Mode 3 contamination. Mode 2 contamination has very little effect, while Mode 3 shows only modest degradation for the four-armed spiral.

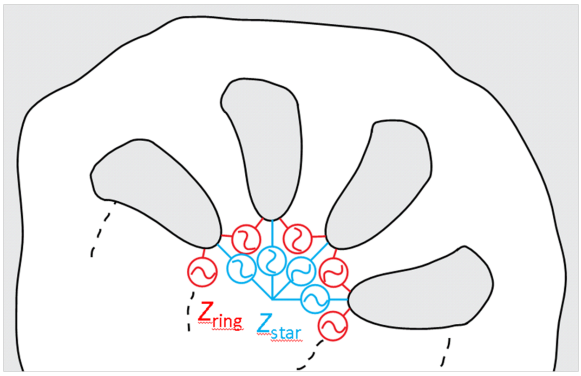

Figure 2.20: Illustration of the difference between the star- and ring-type feeding topologies.

effect is observed in the case of Mode 2 contamination, since Mode 2 radiates at a much higher level than the contaminating Mode -2. However, Mode 3 affects the axial ratio much more strongly below $3f_0$ since nearly all of the energy gets radiated as Mode -1. In the feed region the spiral does not discriminate between Mode 3 and Mode -1, therefore Mode -1 radiates as efficiently as the dominant Mode 1.

2.7 Star- vs. Ring-Type Feeding

The mode impedances Z_m of self-complementary, multi-armed spiral antennas are given by the so-called Deschamp's formula [20, 33]

$$Z_m = \frac{\eta_0}{4 \sin \frac{m\pi}{N}} \tag{2.18}$$

where η_0 is the free-space impedance, m is the mode of excitation, and N is the number of arms. Booker's extension to Babinet's principle [21] can then be applied to transform a star-type feed topology to a ring-type feed (Fig. 2.20). The Mode 1 impedances for multi-armed self-complementary antennas with varying arm counts are shown in Table 2.3. As evident in the table, a ring-type feed is advantageous from an impedance matching standpoint for arm counts higher than six. This theoretical prediction is validated by numerical simulation using **FEKO** in Fig. 2.21. Although not used in the work presented in this thesis, this effect is very important to consider when implementing high arm-count antennas.

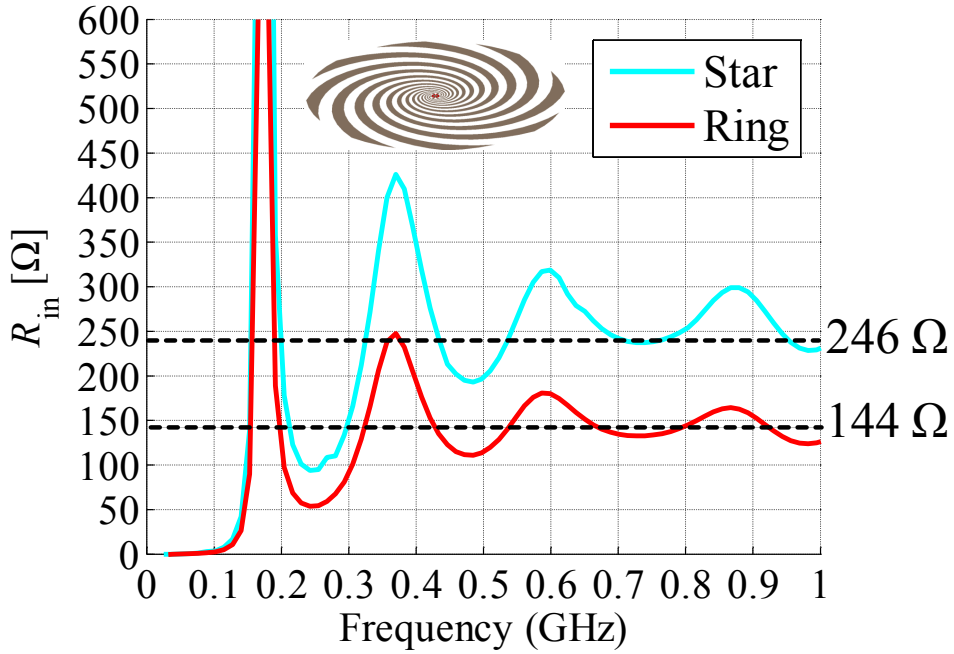

Figure 2.21: Theory validation using **FEKO** of the star- vs. ring-feed impedances for an eight-armed spiral.

Table 2.3: Mode 1 mode impedances for star and ring configurations

Arm Count	Z_{star} [Ω]	Z_{ring} [Ω]
2	94.2	377
3	108	326
4	133	266
6	**188**	**188**
8	246	144
16	483	73.5
32	961	36.9
64	1.92k	18.5

2.8 Conclusions

This chapter covered important theoretical background needed for understanding the material in later chapters. The active-region principle of operation of the spiral antenna was illustrated by evolving the spiral from a simple two-wire transmission line. The concepts of the truncation principle and cutoff frequency are also introduced. Spiral mode theory was introduced by examination of the solution of the infinite-armed spiral electromagnetic boundary-value problem. The usefulness of the mode theory is based on the fact that any arbitary excitation of a spiral can be decomposed into its constituent mode spectrum. The far field can likewise be decomposed into a mode spectrum that is related to the excitation spectrum. The multi-arm case was presented as a discrete version of the infinite-armed spiral. The role of multiarming in accomplishing mode filtering was explored and motivated by example. The use of the DFT for decomposing the excitations of a spiral into its constituent mode spectrum was used to implement a simple method for evaluating the errors in a modeforming network. Finally, impedance reduction of high arm-count multi-armed spirals by ring-feeding was noted, enabling practical implementation of high arm-count spiral antennas.

Chapter 3

Pattern Purity of Coiled-Arm Spiral Antennas

3.1 Introduction

Over the years, many efforts have been undertaken in reducing the spiral's cut-off frequency while maintaining the same aperture size of the spiral. One frequently-employed miniaturization method seeks to increase the electrical circumference of the antenna structure through the use of various loading strategies. These include dielectric [34], magneto-dielectric [35], artificial media [36], arm-shaping [37–40], discrete-element loading [41], or a combination of these [42–44]. Although many have studied this concept from the standpoint of input impedance and broadside gain, little information is available concerning the effects on the spiral's **pattern purity**. Pattern purity, as used in this chapter, is the degree to which a radiation pattern is free from the detrimental effects of **modal contamination**, such as cross-polarization, azimuthal pattern nonuniformity, and beamwidth variation, for example. Modal contamination is the presence of undesired terms in the modal decomposition of the radiation pattern, discussed in Section 2.3. In this chapter we thoroughly discuss the effects of the arm-coiling technique on the far-field characteristics of the spiral antenna.

The two-armed spiral antenna has been studied far more extensively in the open literature than the four-armed spiral. It is well-known that it is a simple matter to feed a two-armed spiral with a Dyson (infinite) balun [8] in order to achieve broadband broadside operation, also referred to as Mode 1 in the terminology of spiral antenna theory. In contrast, four-armed spirals require more complicated feed arrangements. However, the discussion to follow will show that four-armed spiral antennas possess important performance advantages

over the two-armed spiral when combined with the arm-coiling treatment. For instance, it is shown that the measured cross-polarization discrimination of the four-armed spiral at 47° from broadside is improved by up to 15 dB with respect to a comparable two-armed spiral.

This chapter is organized as follows. The geometry under study is discussed in detail in Section 3.2. In Section 3.3, the effect that the arm coiling has on the modal content of the far field is examined, and the physical features of the arm coiling that affect the modal content are identified. Using the modal decomposition data, the effects on pattern azimuthal nonuniformity (WoW), axial ratio, beamwidth, and broadside gain are discussed. The effects of the beam-forming network (BFN) are also discussed. Finally, the fabrication of a coiled-arm spiral and comparisons between measurements and simulations performed using **FEKO** [45] are given in Section 3.4.

3.2 Computational Model Description

The concept of using various types of meandering as a miniaturization strategy for spiral antennas has been advanced by many researchers ([37, 38, 44, 46]). Here we explore the effects of a simple type of volumetric meandering (arm coiling) on the performance of spiral antennas with two and four arms. For this study of arm coiling, an arm geometry was chosen that features two distinct regions. First is an inner self-complementary non-coiled equiangular spiral with a growth rate of $\alpha = 0.0616$/rad and with $5\frac{1}{2}$ turns. This is in contrast with [43, 44], where a wire (non-self-complementary) inner region was used. Second is an outer wire portion with volumetric coiling featuring 168 coils per spiral turn, with $1\frac{1}{2}$ turns, and with the same growth rate as the inner portion. This portion follows the coiling used in [43]. The upper surface of the coiled portion coincides with the plane of the inner spiral, while the lower surface grows exponentially downward with increasing radius. The exponential coil growth rate preserves the log-periodic nature of the structure to some extent. The arm lengths were kept constant among the two- (Fig. 3.1) and four-armed (Fig. 3.2) cases to make the results easily comparable. The overall effect of the coiling is to slow down the outward-traveling wave in the coiled portion of the spiral, thus decreasing the radius of the active region. The expected result is increased realized gain of the desired mode below the spiral's cut-off.

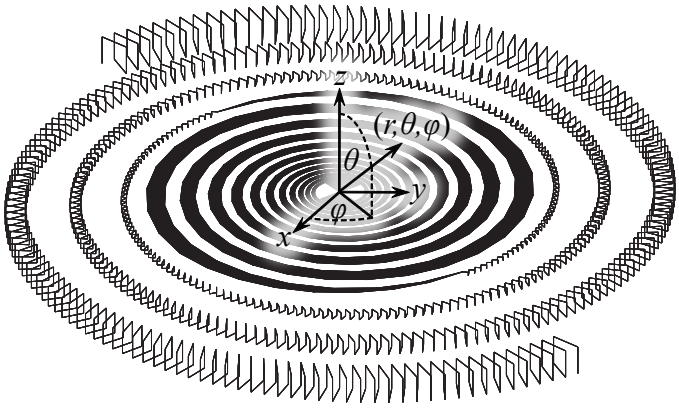

Figure 3.1: Two-armed, seven-turn, right-handed spiral with arm coiling. The center portion is a conventional smooth self-complementary spiral with 5½ turns, and the outer portion is a coiled wire with 1½ turns. The adopted coordinate system is shown at the center.

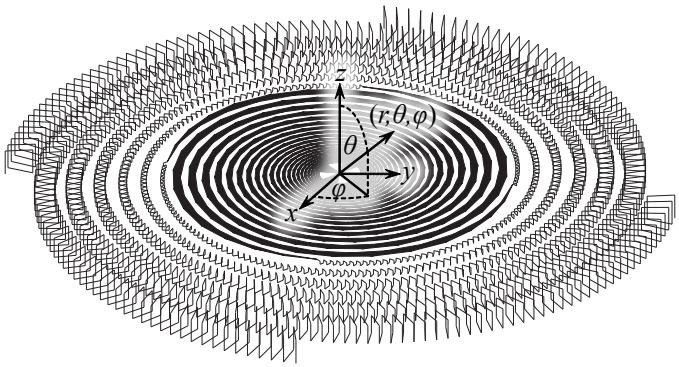

Figure 3.2: Four-armed, seven-turn, right-handed spiral with arm coiling. The center portion is a conventional smooth self-complementary spiral with 5½ turns, and the outer portion is a coiled wire with 1½ turns. The arm length is identical to that of the two-armed spiral. The adopted coordinate system is shown at the center.

3.3 Computational Studies

3.3.1 3D Patterns

An investigation into the co-polarized gain of four-armed spirals is performed using the commercially-available method-of-moments code **FEKO**. For the study a free-standing (free-space) coiled-arm spiral antenna with a radius of 75 mm is used, with other parameters as previously described. We note that the dielectric loading and absorptive backing are not modeled (as is often done in the literature [34, 47, 48]) to reduce the computational complexity; however, their effects will be assessed in Section 3.4. Also, the free-space models used herein simplify the physical interpretation of the spiral's performance. The results,

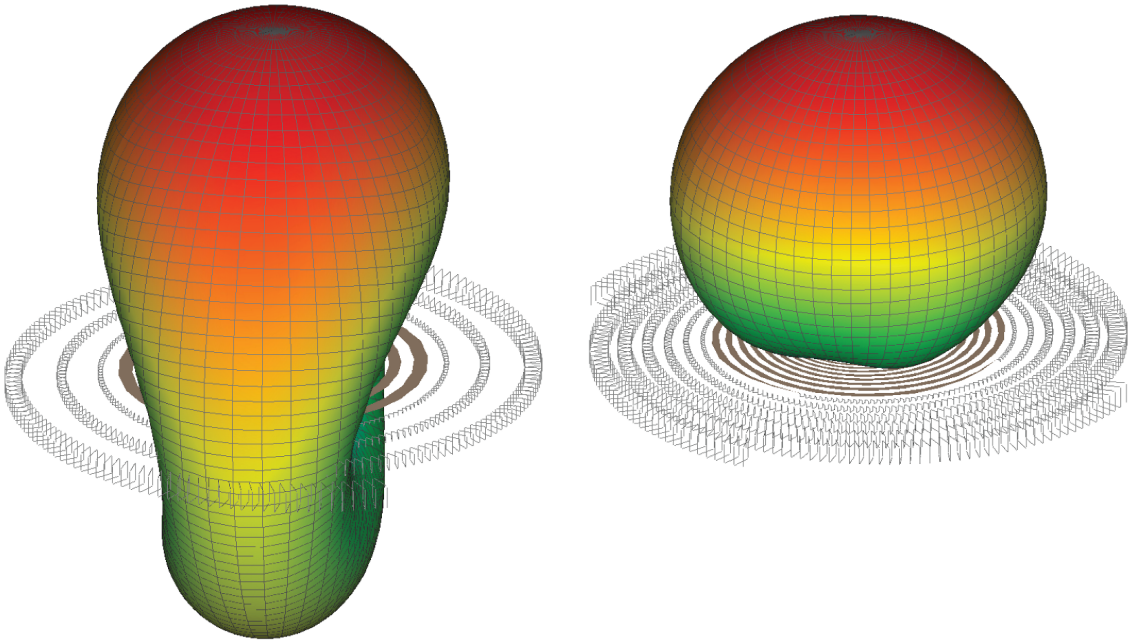

(a) Two-armed (b) Four-armed

Figure 3.3: Three-dimensional co-polarized (RHCP) gain patterns for the coiled-arm spiral antennas at the "cutoff" frequency f_0. The patterns are similar to those of self-complementary, smooth spiral antennas (not shown).

given in the following sections, are shown normalized with respect to the Mode 1 cutoff frequency $f_0 = c/C$ for convenience (c is the speed of light and C is the spiral's circumference). Far below cutoff, the two- and four-armed spiral patterns resemble those of a small horizontal dipole (HPBW$\approx 90°$ in the E-plane and $360°$ in the H-plane) and crossed dipole (HPBW$\approx 130°$), respectively. Well above cutoff the patterns take on the Mode 1 shape (HPBW$\approx 76°$). At f_0, the patterns show a superposition of these characteristics (Fig. 3.3).

It is important to note that as frequency decreases below f_0 the polarization of the two-armed spiral becomes increasingly linear, while the four-armed spiral retains excellent circular polarization. Also, it is well-known that the spiral antenna pattern rotates with frequency [3], owing to its scaling and rotation properties. For the two-armed spiral operated below cutoff, this presents a significant challenge in practical systems. Additionally, the orientation of the polarization ellipse at broadside rotates with frequency, exacerbating the pattern rotation problem. By virtue of its circular polarization at broadside and symmetric pattern below cutoff, the four-armed spiral is far less susceptible to these problems.

The shape of the low-frequency ($f < f_0$) co-polarized radiation patterns (Fig. 3.3) are practically

unchanged compared to those for the free-standing smooth self-complementary spiral. It is apparent that the four-armed spirals have retained their advantage over the two-armed spiral.

3.3.2 Modal Content

As explained in Section 2.3, it is possible to decompose the pattern for a given angle off broadside into its constituent modes, since the spiral modes are orthogonal with respect to azimuth. Figure 3.4(a) shows the mode gains of the two-armed spiral at an angle off broadside of 47°, the theoretical Mode ±3 maximum for small growth rates. Above f_0, the Mode 1 active region is predominantly inside the spiral, allowing Mode 1 to radiate efficiently and producing less efficient spurious Mode -1 radiation (-20 dB at $2f_0$). Above $3f_0$, energy not radiated from the Mode 1 active region is free to radiate from the Mode 3 active region, producing the spurious Mode 3. If the frequency becomes high enough that the active region lies within the feed region, then Mode -1 will again increase if the feed region cannot discriminate that mode. Below f_0, the Mode 1 active region is larger than the spiral, and therefore that mode radiates inefficiently. The reflected Mode -1 radiates at about the same level as the desired Mode 1, so the overall polarization can be expected to be nearly linear.

Figure 3.4(b) shows the modal decomposition of the Mode 1-excited coiled two-armed spiral shown in Fig. 3.1. Modes ±3 and ±5 appear to radiate more efficiently because their active region diameters have also been reduced. Above $2f_0$ the smooth inner portion of the spiral radiates Mode 1 efficiently, causing Mode -1 to decrease. Between f_0 and approximately $2f_0$ the radiation occurs primarily from the coiled portion. A side-effect of the arm coiling is that the coils act as energy-storage elements, preventing Mode 1 from radiating as efficiently from the coiled arms as it would if the arms were made smooth. This causes 0.4 dB gain reduction at $1.5f_0$.

Figure 3.5 shows the modal decomposition of the Mode 1-excited four-armed coiled spiral shown in Fig. 3.2. In this configuration unradiated Mode 1 energy reflects from the arm ends as Mode -3 instead of Mode -1 as for the two-armed spiral. However, Mode -3 contamination never reaches a high level because once that mode can radiate efficiently (above $3f_0$), the energy has already been radiated from the Mode 1 active region located well within the smooth inner spiral. This clearly demonstrates the motivation for

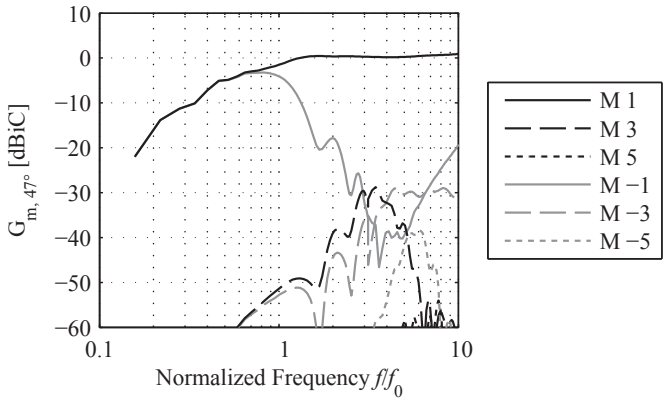

(a) Two-armed smooth spiral

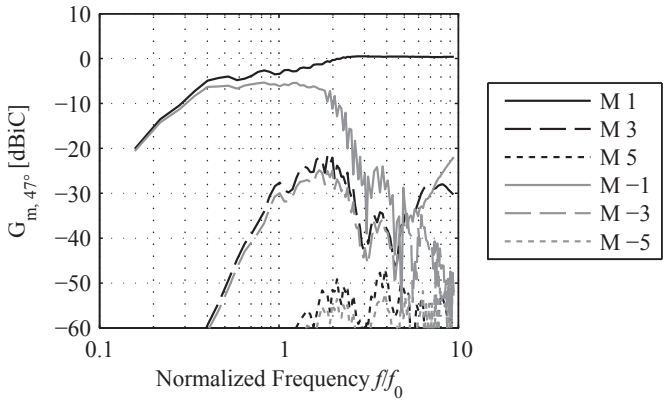

(b) Two-armed coiled spiral

Figure 3.4: Mode gains versus frequency at 47° off broadside for Mode 1-excited two-armed (a) smooth and (b) coiled spiral antennas.

including a non-coiled inner spiral.

3.3.3 3-dB Beamwidths

Using (2.2), the 3 dB beamwidth of an infinite spiral with small growth rate can be estimated to be approximately 76°. However, the presence of spurious modes can produce significant deviation from this value. Figure 3.6 shows the minimum, maximum, and average 3 dB beamwidths for the three spirals discussed earlier. Below approximately $1.5f_0$ the two-armed spirals' beamwidths vary between 85° to 360°, consistent with a dipole-like radiation pattern. Above $1.5f_0$ the smooth two-armed spiral shows little azimuthal variation of the beamwidth since the undesired modes have fallen to more than 20 dB below Mode

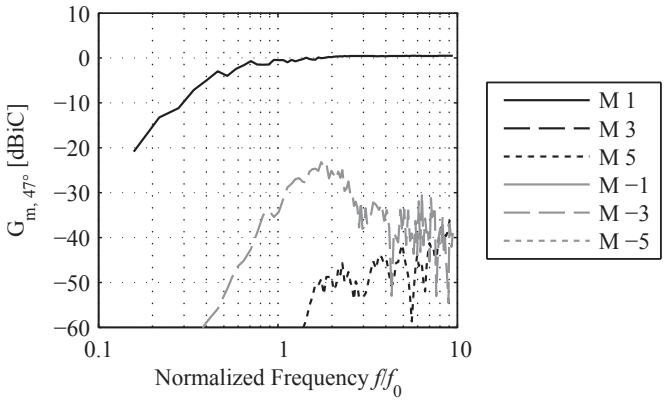

Figure 3.5: Mode gains versus frequency at 47° off broadside for the Mode 1-excited four-armed coiled-arm spiral antenna. Note that the even-ordered modes, as well as Modes 3, -1, and -5, are suppressed by the spiral geometry as well as the mode of excitation

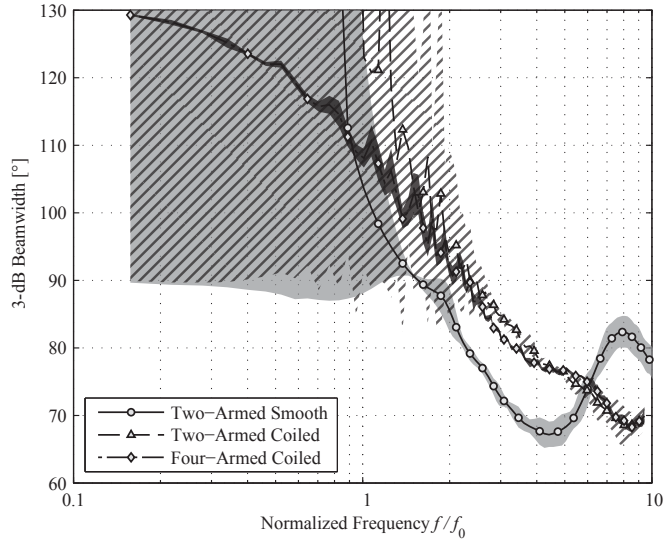

Figure 3.6: Co-polarized minimum, maximum, and average 3-dB beamwidths (with respect to azimuth, sampled in 6° increments) versus frequency. The shaded regions indicate the range between the minimum and maximum 3-dB beamwidths, while the solid lines indicate the average beamwidth. The presence of inductive loading has introduced a noticeable amount of ripple in the beamwidth.

1. The coiled two-armed spiral continues to have large beamwidth variation until $2.5f_0$ due to Mode -1 contamination. In contrast, the four-armed spiral shows little beamwidth variation throughout due to its very low level of modal contamination. The beamwidth transitions smoothly from that of a crossed dipole ($\approx 130°$) below f_0 to that of an infinite spiral ($\approx 76°$) well above f_0.

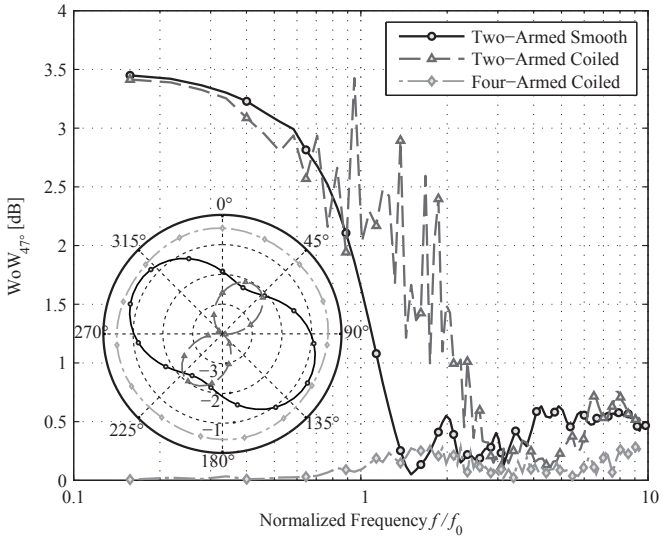

Figure 3.7: Co-polarized azimuthal gain variation at 47° from broadside. Performance is degraded compared to the non-coiled case. Shown in the inset are azimuthal gains at f_0.

3.3.4 WoW

Another parameter of frequent interest in direction finding [49] is the azimuthal co-polarized gain variation (Wobble of the Wave - WoW), defined as the ratio of maximum co-polarized gain to the minimum co-polarized gain, at a given angle off broadside. In Fig. 3.7 we see that in the range of f_0 to $2.5f_0$ the arm coiling degrades the WoW compared to the smooth spiral, due to increased presence of Mode 3. By increasing the number of arms to four, the level of WoW can be reduced to a low level throughout. Additionally, from Fig. 3.8 it is seen that WoW vs. angle off broadside has also been reduced significantly by the use of the four-armed spiral.

3.3.5 Axial Ratio

By coiling the spiral arms, the axial ratio (Fig. 3.9) below f_0 has been improved somewhat compared to the smooth spiral, but is still at a very high level. Between f_0 and $2.5f_0$ the increased presence of Mode -1 from the arm coiling causes the AR to remain high in that region. The AR for the four-armed spiral remains low throughout, owing to the reduced modal contamination afforded by the four-armed spiral and excitation. The main contributor to AR for the four-armed spiral is Mode -3, which exists due to the reflection of residual

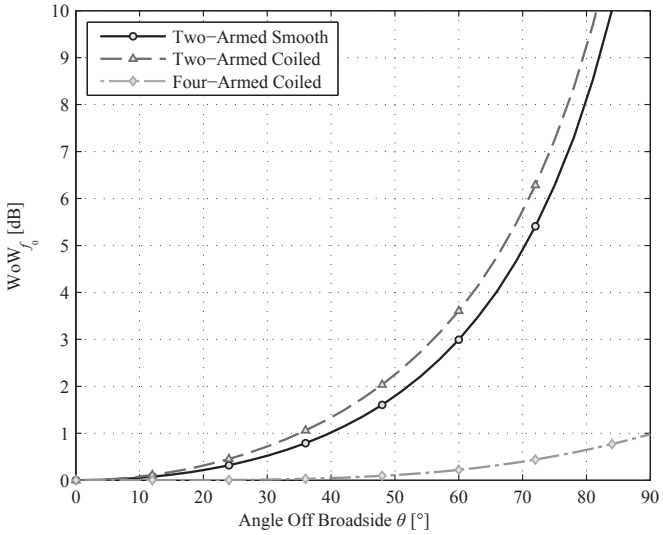

Figure 3.8: Co-polarized azimuthal gain variation at the cutoff frequency versus angle off broadside.

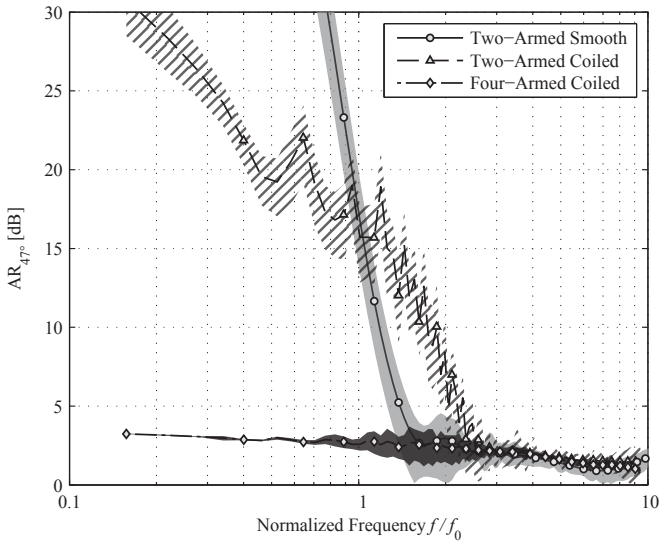

Figure 3.9: Minimum, maximum, and average (with respect to azimuth, sampled in 6° increments) axial ratios at 47° from broadside. Performance is degraded substantially compared to the non-coiled case, being unacceptable for frequencies below approximately $2.5f_0$.

Mode 1 from the arm ends.

Figure 3.10 shows a plot of the AR at f_0 versus angle off broadside. Here one can see that the axial ratio of the four-armed spiral is perfect at broadside, and remains in a useful range (< 3 dB) out to 50° with very little variation over all azimuthal angles.

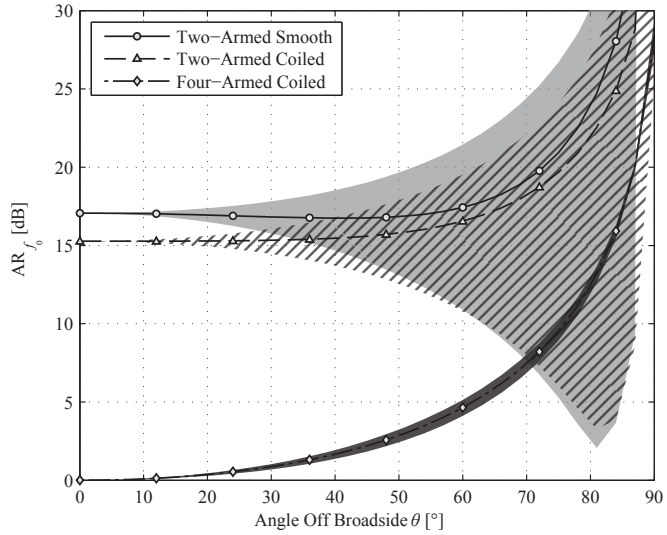

Figure 3.10: Minimum, maximum, and average (with respect to azimuth, sampled in 6° increments) axial ratios versus angle off broadside evaluated at the cutoff frequency f_0. The four-armed coiled spiral shows excellent performance compared to two-armed spirals.

3.3.6 Co-polarized Broadside Gain

Figure 3.11 shows that the broadside gain below $0.8f_0$ is improved by implementing arm coiling. Above that frequency, the arm coiling reduces the gain due to the increased modal contamination. Some of this gain is recovered over the range $0.8f_0$ to $2f_0$ through the use of a four-armed spiral; however, addition of a physical four-armed Mode 1 beamformer is likely to reduce this advantage somewhat.

3.3.7 Beam-forming Network Errors

Throughout the preceding analysis, the excitation was provided by an ideal BFN. However, physically realizable BFNs will invariably have errors, which can be characterized by the procedure in Section 2.3. A typical four-armed Mode 1 BFN is shown in the Fig. 3.12 inset, which consists of a quadrature hybrid followed by two Marchand baluns. The amplitude and phase errors of this network arrange themselves in such a way to produce spurious Mode 3. If the spiral can not radiate or dissipate this mode efficiently, the mode will reflect from the ends of the spiral arms with the same phasing as Mode -1, which produces cross-polarization at broadside. Assuming that the errors of the quadrature hybrid are much larger than the errors of the Marchand baluns, and assuming an amplitude error of ±0.5 dB and phase error of ±2°,

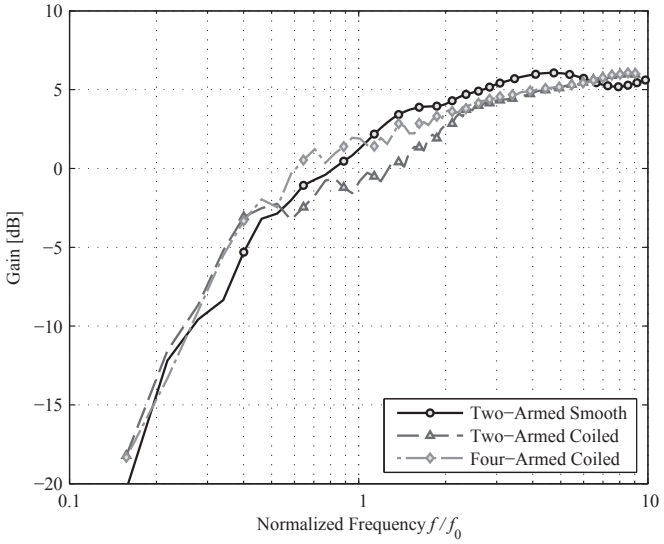

Figure 3.11: Broadside co-polarized gain versus frequency. While the gain has improved at the lower end of the frequency range, the mid-range and high-end gain have been reduced somewhat.

then the cross-modal discrimination between Mode 1 and Mode 3 ($CMD_{1,3}$) will be approximately 23 dB. Figure 3.12 compares the two-armed spiral with an ideal BFN to the four-armed spiral with this realistic BFN. It shows that, even considering errors due to a realistic BFN, the four-armed spiral has performance below f_0 far superior to the two-armed spiral.

3.4 Fabricated Antennas

Using the knowledge gained from the studies of the previous section, two 141 mm-diameter antennas with two and four arms are constructed (the four-armed spiral is shown in Fig. 3.13 and the fully assembled two-armed spiral in Fig. 3.14). Both antennas feature a combination laminate consisting of 508μm-thick RT/Duroid 5880 bonded to 3.175 mm-thick FR-4. The center region consists of a non-coiled equiangular spiral printed on the RT/Duroid material. The metal-to-slot ratio (M/S) of this portion is linearly tapered from M/S = 4 at the center to M/S = 1 (self-complementary) at the outside of the center region. Since no miniaturization is required in the center region, a 63.5 mm-diameter portion of the FR-4 is removed to help preserve pattern purity at high frequencies ($f > 2.2f_0$). The outside region consists of an equiangular coiled-arm spiral printed on the combination portion of the laminate. The arm width is 1.016 mm and the

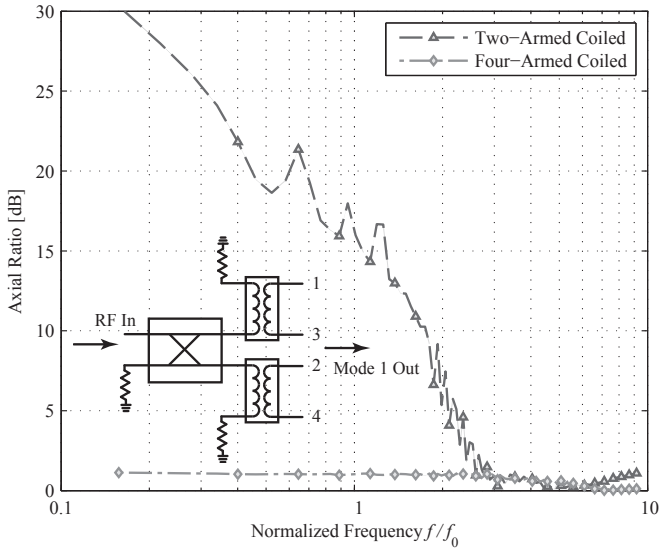

Figure 3.12: Comparison of broadside axial ratio for the ideal-beamformed two-armed spiral and the four-armed spiral with realistic beam-forming network (see inset)having misbalances of ±0.5 dB amplitude and ±2° phase (Modes 1 and 3 cross-modal discrimination $\mathrm{CMD}_{1,3} \approx 23$ dB).

coil pitch is linearly tapered from 38 coils/turn at the inside to 80 coils/turn at the outside. The greater thickness of the outside region substrate allows larger coils to be formed, increasing the path length, and thus allowing a higher degree of miniaturization. A polyvinyl chloride (PVC) sidewall (Fig. 3.14) with 141 mm outer diameter and 6.35 mm wall thickness is used to mechanically support the spiral. If a conducting ground plane is used, then the low-frequency gain is reduced by the tendency of reactive energy to couple to the ground plane. This problem is mitigated through the application of ferrite tile absorber (TDK IB011), which predominantly absorbs the backward radiation over the frequency range of the antenna.

The spiral is excited at the center using a phase-matched and soldered bundle of 2.159 mm-diameter semi-rigid coaxial cables. To simulate an ideal Mode 1 BFN (IBFN), the measured far field of each arm is given the appropriate complex weighting and then the far fields are superimposed. The use of the IBFN allows evaluation of the spiral and feed cable assembly in isolation from the BFN, which is useful when assessing the physics of the antenna element.

Each spiral is modeled in **FEKO**, using MoM with multilayer Green's function (see Fig. 3.13(a) and Fig. 3.13(b)). In order to simulate the antenna using the available computational resources, the following

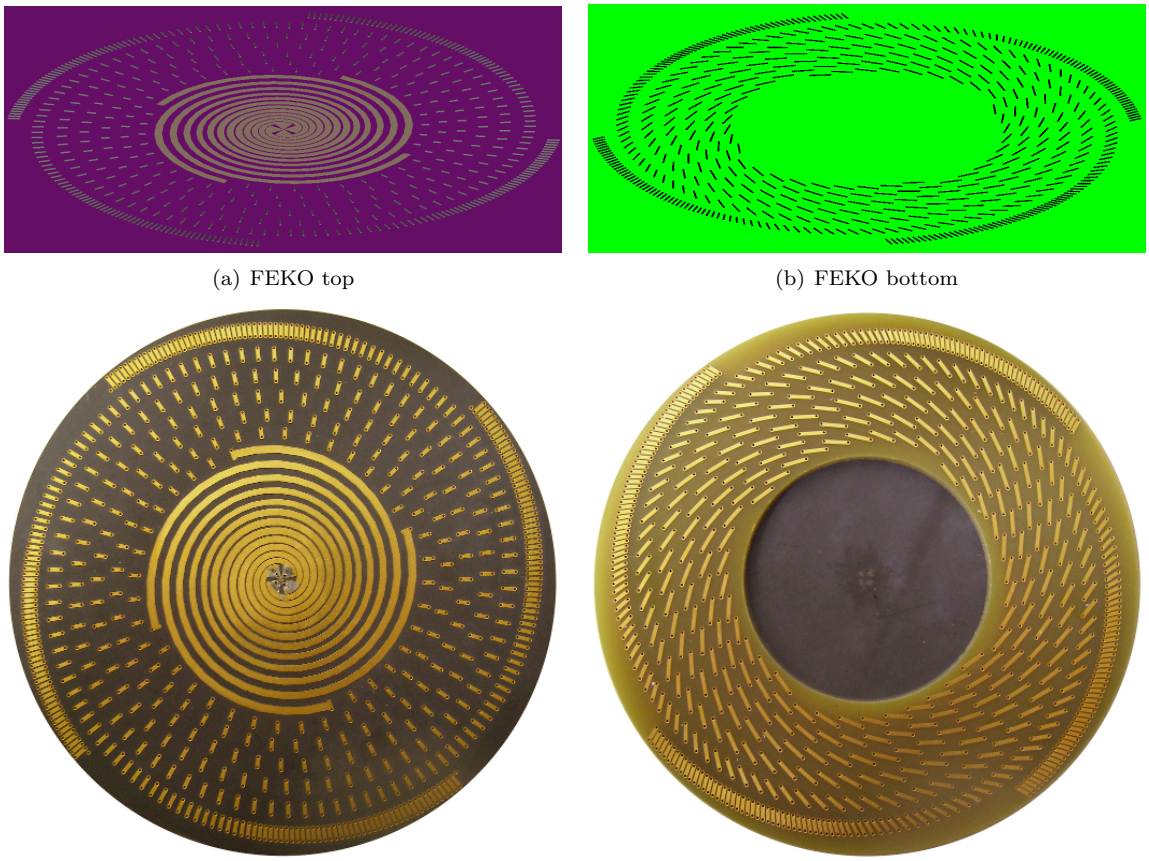

(a) FEKO top

(b) FEKO bottom

(c) Fabricated top

(d) Fabricated bottom

Figure 3.13: Fabricated four-armed spiral with arm coiling applied to the final $1^1/_2$ turns. The two-armed spiral is fabricated similarly, but with $2^1/_4$ turns of arm coiling.

simplifications were made to the computational models:

- The contributions of the dielectric sidewall, the finite square-shaped ferrite-coated backing, and the feed structure are neglected.
- The combination laminate is laterally infinite, as required by the multilayer Green's function implementation.
- The material properties of the bonding layer are assumed to be that of FR-4.
- The entire coiled-arm portion is modeled as thin wires.
- The removal of FR-4 from beneath the center region is not modeled.

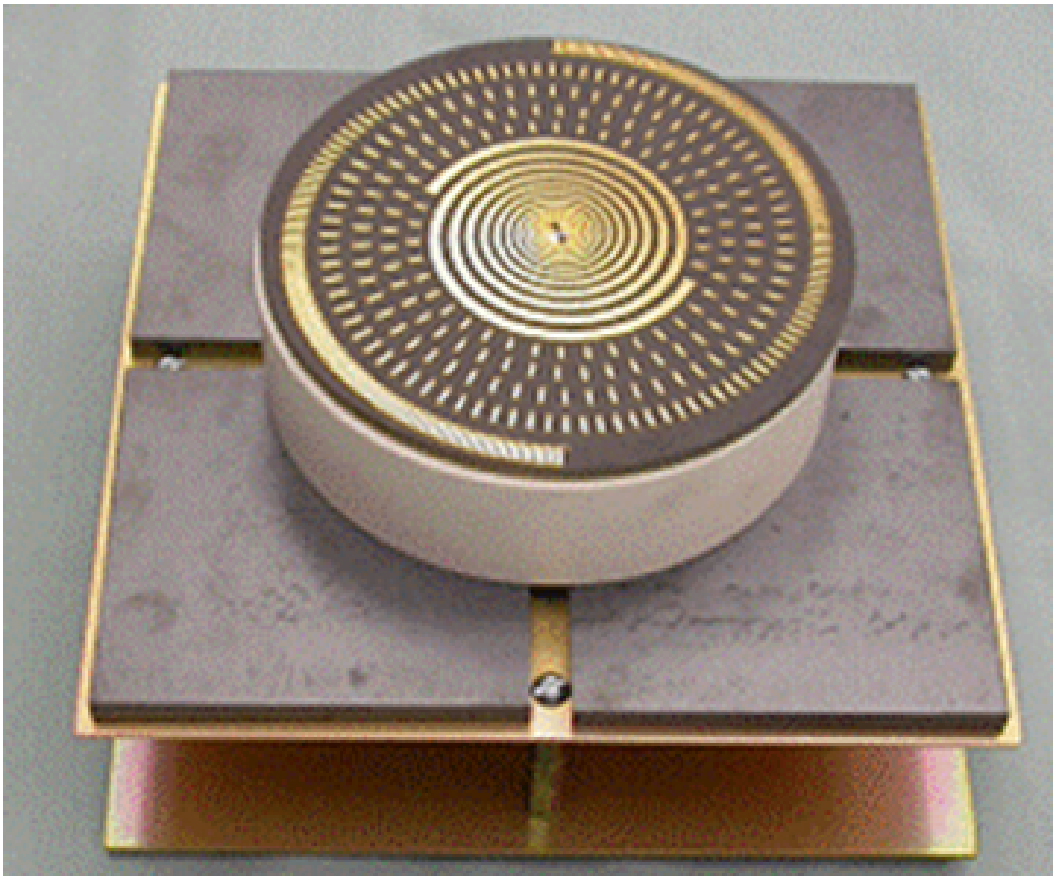

Figure 3.14: Fabricated two-armed spiral antenna with PVC sidewall and ferrite tile backing.

Figure 3.15 shows the simulated and measured broadside and off-broadside co- and cross-polarized (i.e. RHCP and LHCP) gains of the two- and four-armed spirals, and it is found that **FEKO** correlates well with measurements. In both the two- and four-armed cases the measured co-polarized gain is higher than the models predict in the range 0.3-0.6 GHz, likely due to the combined unmodeled effects of the PVC sidewall and the ferrite backing. In the **FEKO** model, the LHCP gain at broadside is that of the numerical noise (< -65 dBiC); however, the measured cross-polarized gain does not vanish at broadside. One potential source of this discrepancy is the circularly-asymmetric antenna backing, and another is the range imperfections, including multipath, alignment error, tower bounce, and range axial ratio.

Overall, the pattern of the four-armed spiral shows significant improvement in cross-polarization discrimination over the two-armed spiral, thus validating our earlier results and conclusions. For example, at 475 MHz, the discrimination of the four-armed spiral at 47° from broadside has increased to beyond 15

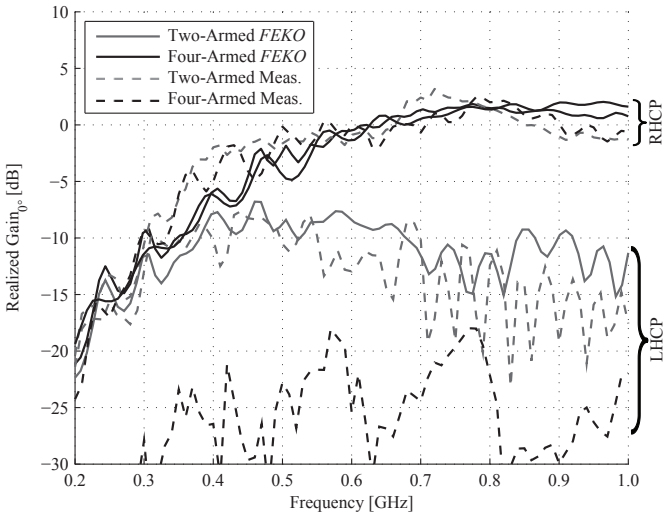

(a) Broadside ($\theta = 0°$)

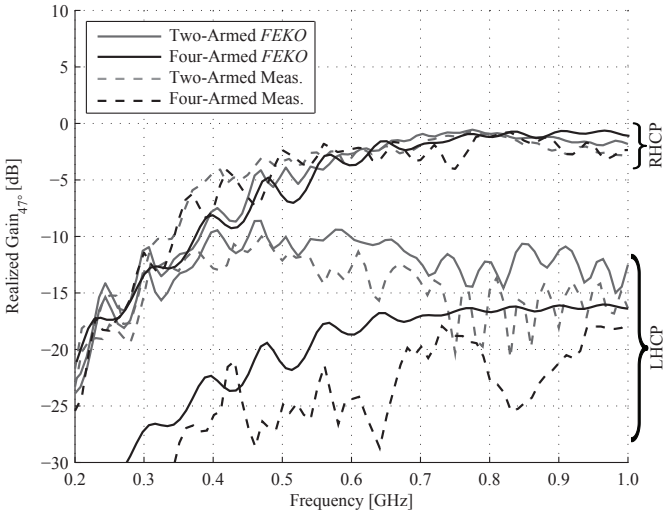

(b) Off-broadside ($\theta = 47°$)

Figure 3.15: Comparison of the measured and simulated (a) broadside and (b) off-broadside realized gains of the two- and four-armed coiled-arm spirals, averaged with respect to azimuth

dB, a huge improvement over the two-armed spiral. Nearing broadside, the improvement becomes even more significant, due to the rapid decrease of Mode -3 with respect to the desired Mode 1 (see Fig. 3.16). As stated above, range imperfections and asymmetry in the antenna backing are the causes of the increased cross-polarization at broadside.

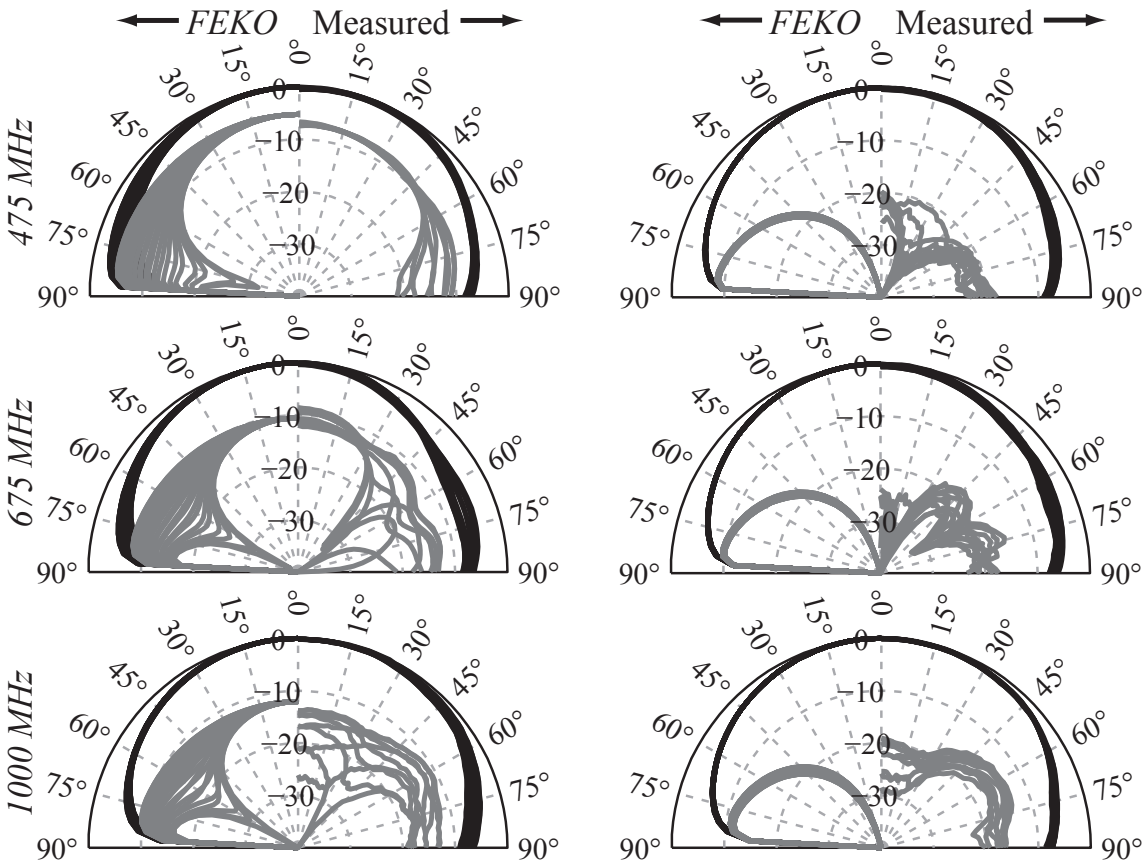

(a) Two Arms (b) Four Arms

Figure 3.16: **FEKO**-simulated and measured elevation pattern overlays at 475 MHz, 675 MHz (f_0), and 1000 MHz for the fabricated (a) two-armed and (b) four-armed spirals. The four-armed spiral shows consistently improved cross-polarization discrimination compared to the two-armed spiral.

3.5 Conclusions

This chapter has compared the performance of coiled-arm two- and four-armed spiral antennas. It was found that the four-armed spiral outperforms the two-armed spiral in nearly every respect when the spirals are operated near or below cutoff. In some instances the two-armed spiral was shown to have undesirable characteristics that make it an unsuitable candidate for practical antenna applications. On the other hand, the four-armed spiral retains its far-field performance characteristics in a robust way, even down to frequencies far below cutoff.

Due to its flexibility and relatively low cost, arm coiling is an attractive miniaturization strategy for spiral antennas. However, it was shown that the use of arm coiling to improve low-frequency gain of the

two-armed spiral produces mixed results when pattern purity effects are considered. While the low-frequency gain is improved, it occurs at the expense of other far-field parameters that are important in applications where spirals are frequently used, such as in radio direction finding and in radar warning receivers. In contrast, four-armed spiral antennas were shown to have a high degree of immunity from the contaminating effects of the miniaturization treatment. For many applications the performance improvement afforded by the four-armed spiral justifies the additional cost and complexity of the beam-forming network.

Chapter 4

Four-Armed UHF- to S-band Spiral-Helix Antenna

Due to their high power handling capability, moderate gain, and multi-mode capability, the antenna most commonly used in electronic attack (EA) applications is the horn antenna. However, this antenna has some shortcomings that are anticipated to make it insufficient to meet the needs of future EA missions. Given that EA antennas must often function over decade bandwidths, it is critical that these antennas have stable patterns in order to provide the needed coverage. Also, the horn antenna is typically large and heavy due to the means by which it is constructed and fed. On the other hand, the two-armed spiral antenna is well known for its pattern and impedance stability over frequency as well as its relatively small size and weight. However, the spiral antenna as typically implemented has low gain and very poor power handling capacity due to the use of absorptive material in the cavity. Finally, the two-armed spiral antenna is not capable of broadband multi-mode operation, despite much expended effort to make it so [12].

An antenna is desired that bridges the performance gap between the two antenna families, and represents a favorable compromise between the two. The fundamental approach is to remove the absorbing cavity from the spiral antenna so that a high-efficiency, high-power-handling capacity antenna can be realized. The elimination of this absorber also results in a significant weight and volume savings compared to both the horn and the two-armed spiral. Compared to the available commercial spiral antenna offerings, the antenna presented in this chapter has much higher gain and efficiency above f_0 and is smaller in size, while maintaining excellent pattern uniformity and cross-polarization level.

The specific objective of the antenna design is to develop a small, 6 inch (15.24 cm) diameter spiral antenna with a reflective cavity 2 inches (5.08 cm) deep or less, operating in Mode 1, with high modal purity

and with high power handling capacity from 250 MHz to 2 GHz. The technical approach is to meld the concepts from frequency independent (FI) antenna theory [27] with the theory of spiral modes [22, 27, 34]. This immediately leads one to the approach of using multiple spiral arms to realize a spiral antenna aperture since, as discussed in Chapter 2, the multiple arms act as a mode filter, enabling highly pure far-field patterns. Additionally, the concept of using various miniaturization techniques, including arm coiling [3] to miniaturize the antenna was considered, but ultimately rejected due to reduced power handling capability, as well as modal contamination as discussed in Chapter 3.

This chapter is organized as follows. Each component of the antenna design is discussed in detail in Section 4.1. The step-by-step assembly process of the antenna is outlined in Section 4.2, and the measured performance of the antenna is presented in Section 4.3.

4.1 Design

4.1.1 Feed Bundle

4.1.1.1 Upper Frequency Limit

In addition to the lower cutoff frequency $f_0 = c_0/\pi D_{\max}$, there also exists an upper limit $f_u \approx c_0/\pi D_{\min}$ to the operational frequency of the spiral, determined by the minimum diameter $D_{\min}$ that the fidelity to the spiral shape is maintained. Since the junction between the feed bundle and the spiral center is critical to the structural and electrical integrity of the overall antenna, the spiral shape is sacrificed near the feed in order to improve the robustness of the junction. Since the central feed region does not maintain a spiral shape, the mode-filtering properties of the spiral are lost, causing the pattern integrity to degrade due to modal contamination. Therefore, in order to maximize the upper frequency of operation, the size of the feed bundle should be kept to the minimum desired for power handling purposes.

4.1.1.2 Power Handling

Since a design objective is to maximize power handling of the antenna, the feed bundle must be constructed from cable with high power-handling capability. Since the desired upper frequency of operation f_u

is only 2 GHz, the bundle can be allowed to occupy a diameter of nearly 2.5 cm without causing unacceptable harm to the antenna's properties. Given that a single 6.35 mm diameter PTFE-filled semi-rigid coaxial cable has a power handling capacity of 330 W at 5 GHz, there is no need to approach this limit. Assuming a perfect impedance match, a four-armed feed bundle using this type of coaxial cable would have a total power handling capacity of 1.32 kW, with a diameter of approximately 1.5 cm. This level is expected to far exceed the power handling capacity of any of the other components of the antenna, and is therefore deemed sufficient for the design.

4.1.2 Spiral

4.1.2.1 Growth Rate

Effect on Gain: Since the antenna is expected to function at frequencies both well below and well above the Mode 1 cutoff frequency f_0 of the spiral, attention must be given to the gain of the antenna in both regions. Above cutoff, the Mode 1 active region radiates strongly, and so a slow growth rate is preferred to preserve the essential frequency-independent nature of the spiral. However, as shown in Fig. 4.1, using a slow growth rate increases the spiral's cutoff sharpness, increasing the difficulty of obtaining satisfactory gain below f_0. By careful selection of the growth rate, a balance is struck between the performances below and above f_0.

Effect on Axial Ratio: Since the antenna is excited at the center in Mode 1, the axial ratio at broadside is ideally unity; however, the off-broadside axial ratio is controlled by the growth rate of the spiral as shown in Fig. 4.2. There, it is shown that in order to realize an acceptable field-of-view of the antenna, the growth rate must not be made too large.

Effect on Power Handling Capacity: The peak power handling capacity of a free-standing self-complementary spiral in air is limited by the dielectric strength of the air as well as the distance between the spiral arms. The gap between adjacent arms is controlled by the growth rate a, where the gap becomes smaller for decreasing a. Therefore the growth rate should be maximized when peak power handling capacity is a priority. Average power handling capacity is limited in part by the ability of the structure to dissipate heat generated due to loss power. Since the loss power density is highest near the center of the spiral, most of

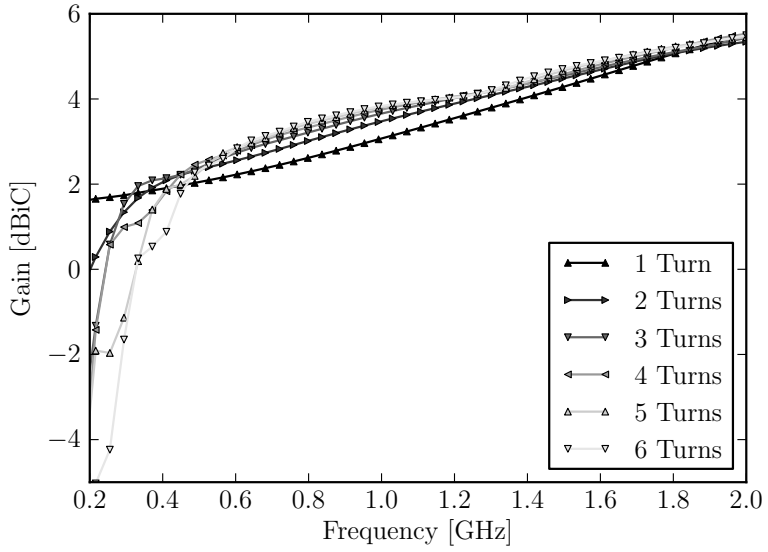

Figure 4.1: Broadside co-polarized (IEEE-defined) gain versus frequency for Mode 1-excited four-armed, 15.24 cm diameter spirals with various growth rates. Each trace represents a number of turns ranging from one turn (fast growth) to seven turns (slow growth). Faster growth rates translate into higher gain at the low end of the frequency range, but result in decreased mid-range gain for the two-armed spiral because of the increased cross-polarization. Multi-armed spirals do not exhibit this gain decrease, due to their inherently pure polarization at broadside.

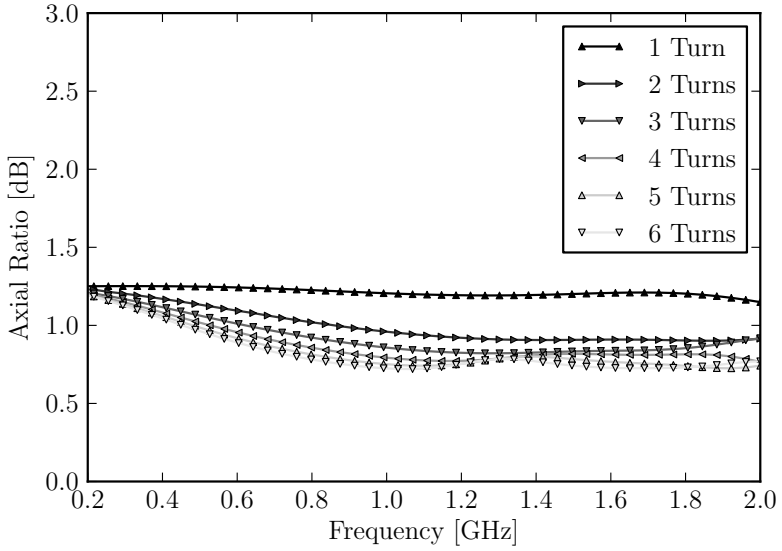

Figure 4.2: Average axial ratio for Mode 1-excited four-armed, 15.24 cm diameter spirals with various growth rates at 30° from broadside. Each trace represents a number of turns ranging from one turn (fast growth) to seven turns (slow growth). Increasing the growth rate degrades the average axial ratio.

the heat must conduct over a large fraction of the arm length. The thermal resistance of the arms increases with decreasing width of the arms, which is controlled by the growth rate in precisely the same way as the adjacent arm gap. Therefore the growth rate should also be maximized when average power handling capacity must be maximized.

For the present design, a growth rate of approximately $a \approx 0.22$/rad was chosen as a compromise among the parameters of gain, off-broadside axial ratio, and power handling. The resulting spiral shape is shown in Fig. 4.3

4.1.2.2 Impedance Control

As discussed in Chapter 2, the Mode 1 impedance of a four-armed spiral is $\eta_0/2\sqrt{2} \approx 133\ \Omega$, where η_0 is the impedance of free space. To a 50 Ω system, this presents a VSWR of approximately 2.7:1, corresponding to nearly 21% reflected power. While some impedance transformation could be performed in the feed bundle, the length of the bundle is insufficient to accomplish the necessary transformation down to the lowest frequency of operation. Therefore the impedance of the spiral aperture must be reduced to a level closer to 50 Ω. The techniques employed in accomplishing this impedance reduction are increasing substrate thickness and using a dual-layered spiral. Both of these techniques have unwanted side-effects on the far field, and so each technique is employed only to the extent necessary to accomplish the required impedance reduction.

Substrate Thickness: In the coplanar strip (CPS) style of transmission line, the characteristic impedance may be reduced by increasing the thickness of the substrate. This impedance reduction is caused by higher electric field concentration in the substrate, thereby increasing the per-unit-length shunt capacitance. Likewise, increasing the thickness of the spiral substrate generally reduces the impedance of the spiral.

However, this increase of energy concentration in the substrate has important consequences. The spiral and dielectric slab combination forms a leaky-wave waveguiding structure that traps some of the energy that would otherwise be radiated in the Mode 1 active region, and instead causes this energy to continue outward, radiating in higher-order active regions and causing pattern distortion. In the present

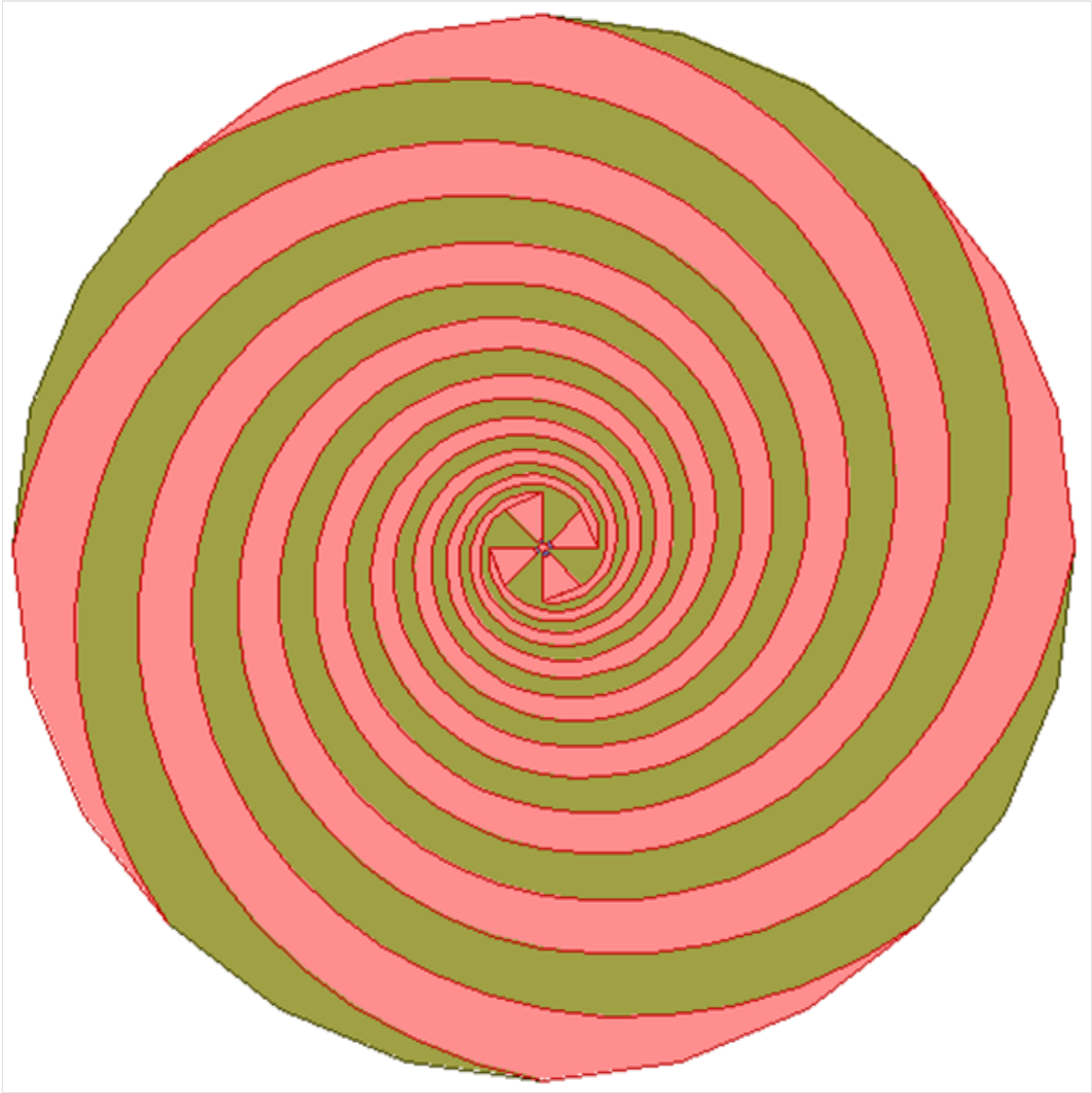

Figure 4.3: **HFSS** model (15.24 cm outer diameter, 1.53 cm feed region diameter) of the chosen spiral shape for the spiral-helix antenna design. The growth rate of $a \approx 0.2$/rad achieves an appropriate compromise among the relevant design parameters.

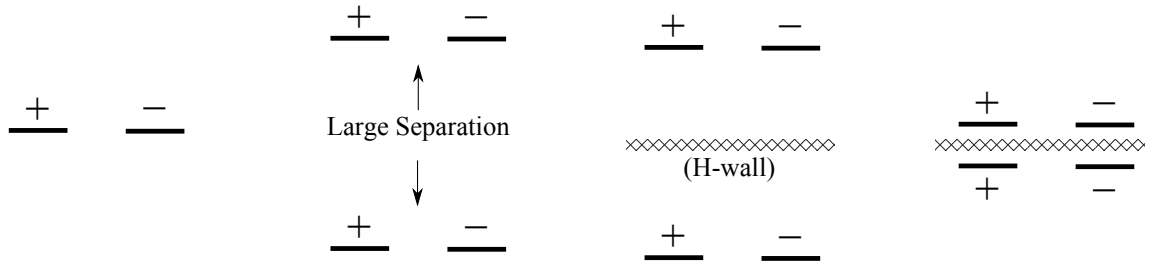

(a) Coplanar strip (CPS) (b) Parallel CPS (c) Virtual H-wall (d) Close proximity

Figure 4.4: Illustration of the dual-layering concept for spiral impedance reduction. The + and - signs indicate the instantaneous voltage polarity on the line.

design a 1.59 mm substrate thickness was selected as a compromise that lowered the impedance of the spiral while sufficiently preserving the beam integrity. To minimize prototyping cost, FR-4 substrate was used in lieu of other known electrically- and thermally-superior materials.

Dual Layering: In addition to the goal of decreasing the impedance of the spiral, it is also highly desirable to realize the highest power handling capacity possible. A method that increases the total metalization on the spiral is highly attractive. Therefore, the second impedance reduction measure uses the concept of parallel modal impedances to accomplish the impedance reduction goal. The following is a basic summary of the dual-layering concept, which explains how the impedance reduction is achieved and why the technique doesn't work well with thin substrates or large inter-arm gaps, such as those occurring near the outside of an equiangular spiral.

When thinking about the spiral as a wave-guiding structure it is often helpful to think in terms of ungrounded coplanar stripline (CPS). While this structure has obvious differences with the spiral, the extension to the situation of a spiral is conceptually straightforward. Take the following ungrounded CPS line shown in Fig. 4.4(a) as an example. The + and - signs indicate the sign of the instantaneous voltage polarity on the line and the characteristic impedance of this line is $\sqrt{L/C} = Z_0$. If a second ungrounded CPS line is added far away from the first (Fig. 4.4(b)), and the + side of the generator is tied to the + lines and the - side of the generator tied to the - lines, then the same voltage difference is obtained between the lines, but with **half** the current yet the **same** charge on each one. Now the impedance is $\sqrt{(L/2)/(2C)} = Z_0/2$ by the definition of characteristic impedance, due to the doubling of the capacitive coupling between the lines and

halving of the per-unit-length inductance. From a circuit-theoretical perspective, this yields two uncoupled (zero mutual inductance or capacitance) ungrounded CPS lines in parallel. Note that there exists an H-wall (i.e. even mode) symmetry plane between the two lines (Fig. 4.4(c)), which means that the H-field must be perpendicular and the E-field must be parallel at that boundary. Now, if the top and bottom ungrounded CPS lines are brought closer together, flux linkage occurs between the top and bottom ungrounded CPS lines. This increases the mutual inductance of the two lines, thereby increasing the characteristic impedance and countering the effect that one is attempting to promote by using dual-layering.

If the vertical distance is decreased until it is much less than the horizontal strip separation (Fig. 4.4(d)), then there is tight flux linkage between the top and bottom conductors, bringing the total inductance of each line up to $2L$. The capacitance of each strip is $C/2$ because the charge tries to move away from the H-wall. Combining these per-unit length inductances and capacitances in parallel brings the characteristic impedance back up to the expected value of $\sqrt{L/C} = Z_0$ as the top and bottom lines become asymptotically close.

In addition to the dielectric loading described earlier in this section, spiral metallization has been applied to both the top and bottom of the 1.59 mm thick FR-4 spiral substrate to realize a dual-layered structure that accomplishes the desired impedance reduction while increasing the average power handling capacity of the spiral. The top and bottom metallizations are connected with vias at the feed point and at the outside of the spiral where the transition to a helix occurs, but are otherwise not connected along the length of the spiral. The small separation between the layers means that the currents on the top and bottom layers are essentially in-phase, ensuring the applicability of the earlier analysis. The exponential growth rate means that the modal impedance gradually increases from the spiral center to the outside. This accomplishes a tapered impedance transformation from the 50 Ω impedance of the feed bundle to the higher impedance of the terminating helix.

4.1.3 Helix

The four-armed spiral is a bi-directional radiating structure. Given that the antenna is expected to operate down to 250 MHz, and that the antenna is only allowed to have a height of 5.08 cm ($d \approx \lambda/23$),

it is clear that coupling to the ground plane poses a problem for achieving good gain performance below f_0. This coupling can be reduced by utilizing an antenna structure that accomplishes directional radiation without the aid of the ground plane. This directional radiation can serve to mask the ground plane from the antenna, greatly aiding the antenna performance below f_0. The purpose of this section is to show that this function can be realized by adding a quadrifilar helix-like loading to the end of the spiral, so that currents that reach the end of the spiral continue downward along the helix.

A left-handed, quadrifilar, axial-mode helix radiates RHCP in the backward direction if it is fed in Mode 1 at the top. If the helix is sufficiently long, there exist two distinct regions on the helix, the so-called C and S [50] regions. The C region is the closest to the feed where the current has a decaying behavior, whereas in the S region (where the surface wave exists) the current is nearly constant throughout the length of the helix. Given the short height of the desired antenna, there is only room for the C region. The lack of the S surface-wave region limits the amount of gain that can be obtained from the helix. Fig. 4.5 shows the 15.24 cm diameter 0.75-turn helix structure used as the spiral termination in the antenna, which is capable of providing a significant front-to-back ratio despite its short length. For simulation purposes the structure is excited at the top with a ring-type Mode 1 feed, and terminated at the bottom in 266 Ω loads. The simulated front-to-back ratio of this structure varies from 20 dB at 200 MHz to 5 dB at 600 MHz. This is sufficient to provide some masking of the ground plane effect at low frequencies. The gain of the structure varies from -22 dBiC at 200 MHz to over 3 dBiC at 600 MHz. Thus the helix is able to make a significant contribution to the overall gain of the antenna.

4.1.4 End Loading

In order to provide an acceptable impedance match over the frequency range of 250 MHz to 2 GHz with an antenna having a minimum electrical radius $kr \approx 0.5$, it is necessary to apply lumped resistive loading to the bottom arm ends of the quadrifilar helix. Since the antenna is to be located above a ground plane, using a star-type termination topology is the obvious choice. The loads are realized as 50 Ω N-type coaxial connectorized terminations. This choice of termination has a number of unique advantages:

- Numerous high-power commercially-available loads exist, in power handling capacities of up to 1 kW

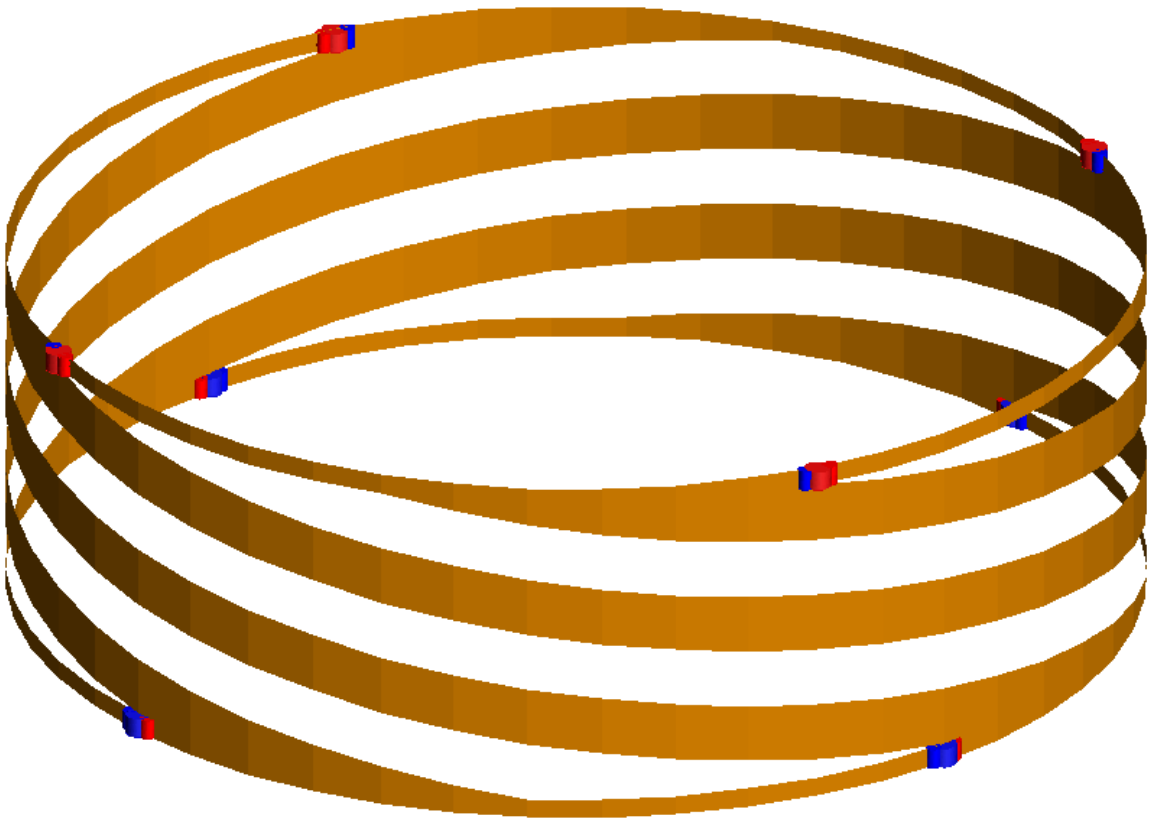

Figure 4.5: **FEKO** model of the 15.24 cm diameter, 0.75-turn quadrifilar helix used in the spiral-helix antenna. The model is fed at the top with a ring feed, and is terminated at the bottom in 266 Ω discrete resistors. The front-to-back ratio varies from 20 dB at 200 MHz to 5 dB at 600 MHz. The gain varies from -22 dBiC at 200 MHz to 3 dBiC at 600 MHz, which is a significant contribution to the gain of the overall spiral-helix antenna.

- The thermal engineering of the loads has been already been performed and validated extensively by the manufacturers
- In cases where it is not acceptable to dissipate high powers near the antenna, the power may be routed elsewhere simply by replacing the loads with cables routed to the appropriate location.

4.2 Fabrication

Fig. 4.6 shows the fabrication process for the four-armed spiral helix. The fabrication steps are outlined as follows:

(1) First, to provide a solid base on which to perform subsequent fabrication steps, a pre-drilled aluminum baseplate (Fig. 4.6(a)) is populated with four N-type pass-through type coaxial connectors.

(2) Next, four pre-formed 250 mil diameter, 50 Ω semi-rigid copper coaxial cables are attached to the baseplate to form a bundle (Fig. 4.6(b)). The bundle is then soldered together, and the soldered joints are cleaned up for the next step.

(3) Then, the 8"-diameter bottom-metalized FR-4 baseplate is press-fit over the soldered bundle (Fig. 4.6(c)). The press fit negates the need to perform a difficult soldering to the cable bundle. The coaxial loads are affixed to the bottom of the baseplate

(4) The helix is placed on the baseplate, and the helix arms are soldered to the coaxial load center pins (Figs. 4.6(d) and 4.6(e)). The bottom metalization negates the need for absorptive filling of the cavity.

(5) Finally, the spiral is affixed to the top (Fig. 4.6(f)). If a dual-layered spiral is used, a dielectric spacer is used to obtain electrical isolation between the bottom spirals and the coaxial cable shields. The spiral is soldered to the coaxial cable bundle at the center and soldered to the helix arms at the outside, which completes the assembly.

The fully-assembled antenna is shown in Fig. 4.7. While the antenna is designed for use with a large ground plane which eliminates the backlobe, the antenna may also be deployed without a ground plane in which

(a) Bundle fixture

(b) Assembled bundle

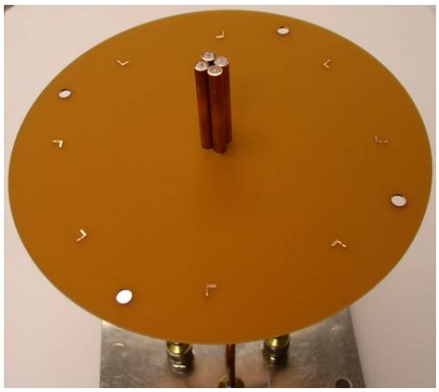

(c) Baseplate

(d) Helix

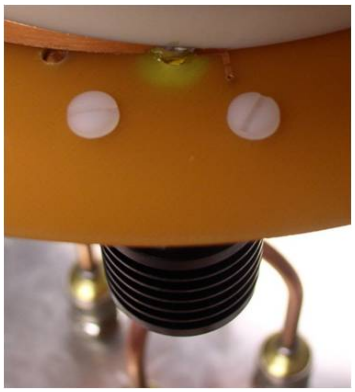

(e) Coaxial terminations

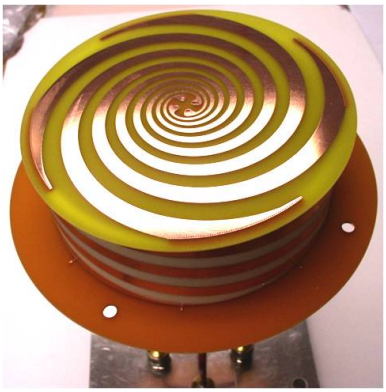

(f) Dual-layered spiral

Figure 4.6: Fabrication process for the four-armed spiral.

case the backlobe is 7 dB below the main lobe at f_0.

4.3 Measurement

The measured and simulated active S_{11} is shown in Fig. 4.8, showing excellent agreement between measurement and simulation, as well as good consistency among all ports indicating high-quality fabrication. As seen, the return loss remains greater than 10 dB above 350 MHz. This amounts to nearly 9x improved mismatch loss compared to a self-complementary spiral in free space. Fig. 4.9 compares the broadside gain of the spiral-helix, showing impressive gain improvement over the band, while having a much shallower cavity depth and likely enabling higher power handling than any of the commercial alternatives. The ideal-beam-formed patterns of the antenna at f_0 are shown in Fig. 4.10, where excellent azimuthal uniformity is evident. The cross-polarization null fill-in at broadside shown in the measured results is due to non-idealities in the measurement.

4.4 Conclusions

The antenna presented in this chapter bridges the performance gap between the horn antenna traditionally used in EA applications, and the absorptive-backed spiral antenna. The fabricated antenna shows much-improved gain and power handling capacity compared to the absorptive-backed spiral, while having a very compact form factor compared to commercially-available antennas. Also, the antenna has a useful bandwidth that extends far below the cutoff frequency f_0 of the spiral, validating the resistive loading approach used in the design. The resistive loading is easily removable and reconfigurable, allowing varied approaches to thermal management. The resulting antenna provides a highly compact replacement to the traditional horn antenna while maintaining a high degree of beam quality.

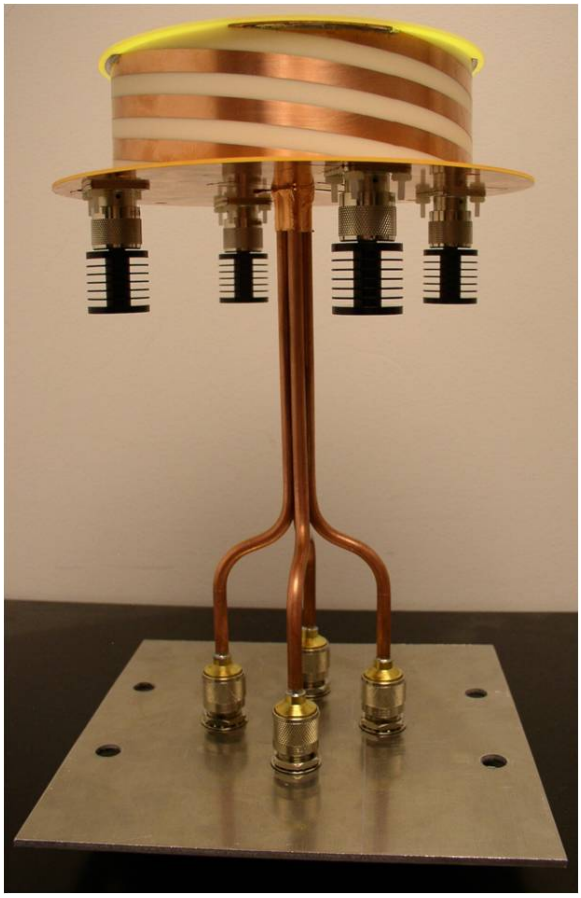

Figure 4.7: The fully-assembled spiral-helix antenna. The antenna can be readily shortened by about 15 cm by trimming of the coaxial bundle.

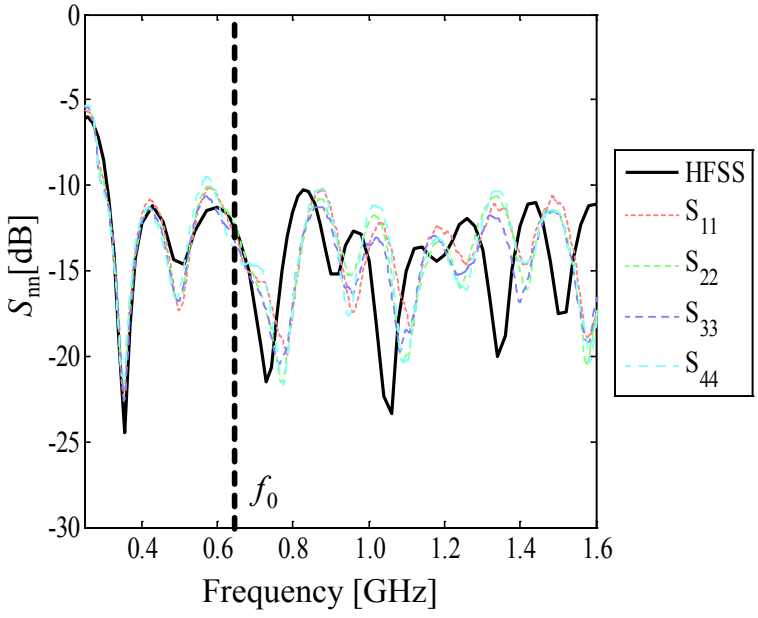

Figure 4.8: S_{11} for the spiral-helix antenna

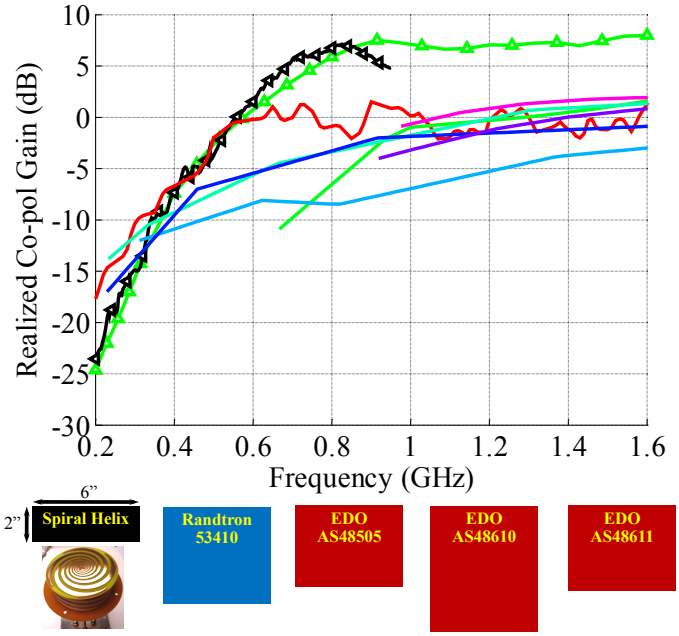

Figure 4.9: Comparison of the broadside realized gain of the spiral-helix with several commercially-available spiral antennas (results are scaled so that all antennas have the same diameter). The spiral-helix discussed in this chapter outperforms the commercial antennas, despite having an extremely shallow cavity depth.

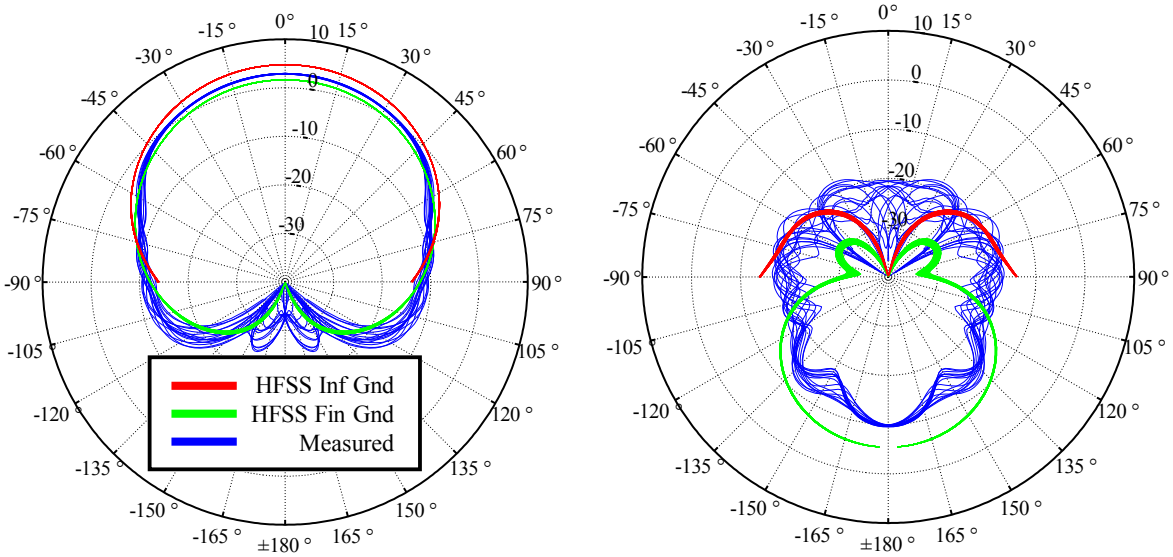

(a) RHCP (b) LHCP

Figure 4.10: Ideal-beam-formed pattern overlays of the spiral-helix antenna at f_0. The “HFSS Fin Gnd” and “Measured” traces represent the simulated and measured patterns of the antenna shown in Fig. 4.7. The “HFSS Inf Gnd” trace represents the pattern of the antenna mounted on an infinite ground plane.

Chapter 5

Wideband Pattern Nulling Using Multi-Armed Spiral Antennas

5.1 Introduction

The ability to place nulls in an antenna's radiation pattern is of fundamental importance in antenna array theory. Some possible uses are to reduce multipath, unintentional, or hostile interference in navigation systems, to reduce cosite interference on mobile communication platforms, or to provide spatially-selective jamming capability. Some [51, 52] have described systems using the spiral antenna for wideband adaptive null placement, using the fact that multi-armed spirals are known to make excellent wideband DOA sensing elements. Others [53] have used the phase modes of the multi-armed spiral antenna to decorrelate interfering MIMO signals. However, the algorithms previously described for use with these systems neglect the unique and vitally important physical principles of the multi-armed spiral. Furthermore, these algorithms typically call for an iterative null search process. This chapter describes a method that uses the spiral (or phase) modes [12, 28, 31] of the spiral antenna to implement a direct (i.e. non-iterative) nulling method. Valuable insight into the physical capabilities and limitations of the method with the multi-armed, multi-mode spiral antenna is easily obtained as a consequence of using the spiral modes.

This chapter is organized as follows. Section 2.4 reviews the fundamental physical principles of the multi-armed spiral antenna. Section 5.2 discusses the emergence of nulls by the superposition of mode patterns, as well as the basic behavior of the resulting nulls. Section 5.3 introduces a simple nulling algorithm, capable of placing a number of nulls at arbitrary locations in the radiation pattern. Section 5.4 demonstrates the use of the algorithm for placing a single null into a radiation pattern, while Section 5.5 demonstrates

Table 5.1: Relative mode phasing needed to produce a null at the given azimuth location

Relative Mode Phasing $\Delta\phi = \phi_{M2} - \phi_{M1}$ [°]	Null Azimuth [°]
0	180
45	225
90	270
135	315

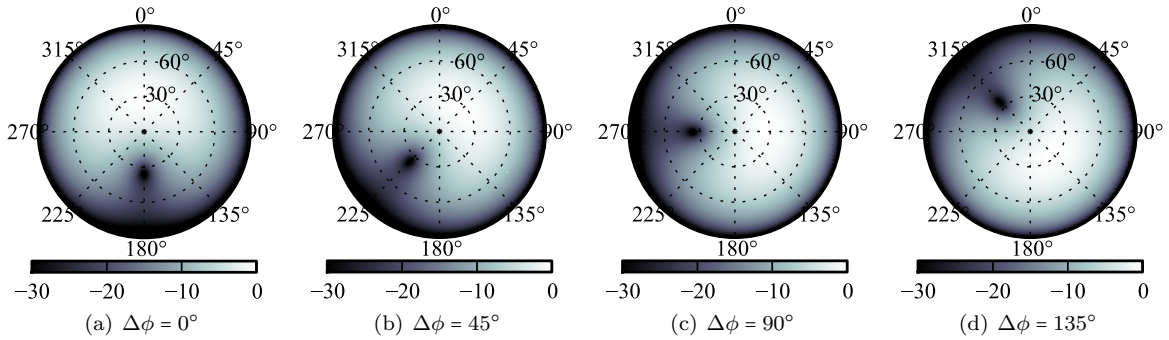

(a) $\Delta\phi = 0°$ (b) $\Delta\phi = 45°$ (c) $\Delta\phi = 90°$ (d) $\Delta\phi = 135°$

Figure 5.1: Theoretical upper-hemisphere RHCPpartial far field patterns for several relative phasings. Notice the clear null rotation in azimuth.

multiple simultaneous null placement. Finally, Section 5.6 discusses certain practical considerations and limitations of the method; namely, null rotation compensation and mode cutoff.

5.2 Mode Superposition

The essence of the nulling concept can be simply illustrated by superimposing ideal mode patterns, expressions for which were first derived in [3]. A null occurs wherever the amplitudes of the two modes are equal and their phase differs by π radians. For ideal spiral modes this condition occurs at a discrete number of points $\Delta m = m_H - m_L$, where m_H and m_L are the respective higher and lower mode indices. The azimuth at which the null occurs is determined by the relative phasing of the modes. Table 5.1 shows how the phase differences are related to the null azimuth location. Figure 5.1 shows the far-field patterns for several relative phasings, where clear and precise azimuthal pattern rotation is observed. Likewise, the null elevation is set by the relative amplitude of the modes. Table 5.2 shows how the relative amplitudes are related to the null elevation. Fig. 5.2 shows the resulting far-field patterns, where null steering in elevation is evident.

Table 5.2: Relative mode amplitudes needed to produce a null at the given elevation location

Relative Mode Amplitude $\max(\lvert M2\rvert)/\max(\lvert M1\rvert)$ [%]	Null Elevation [°]
50	90
75	36
100	25
200	11

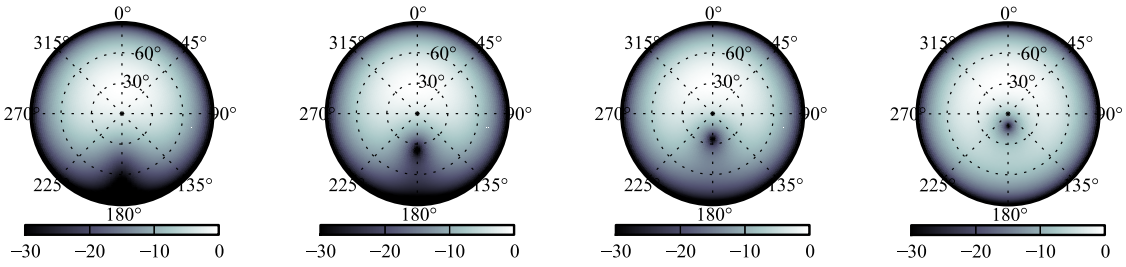

(a) 50% (b) 75% (c) 100% (d) 200%

Figure 5.2: Theoretical upper-hemisphere RHCPpartial far field patterns for several relative amplitudes. Notice the clear null movement in elevation from horizon (a) toward boresight (b→d).

5.3 Nulling Algorithm

To obtain specific field values in $N-1$ given directions (θ_p, ϕ_p), the problem can be simply formulated by point matching as

$$[F] = [A][a] \tag{5.1}$$

where the desired complex far-field values $F_p = F(\theta_p, \phi_p)$ are the elements of the vector $[F]$, and the elements of $[A]$ are

$$A_{pm} = F_m(\theta_p, \phi_p) \tag{5.2}$$

At least one of the F_p must be nonzero to avoid the trivial solution, which reduces the number of achievable broadband (i.e. not using spiral Mode 0) nulls to $N-2$. Solving (5.1) at each frequency of interest results in a set of $N-1$ complex excitation weights $a_m(f)$ for Mode m, where f is frequency. If a spiral mode-forming network is used, then the a_m are used as voltage inputs to the modeformer, after correcting for modeformer non-idealities. If direct arm excitation is used instead, the arm excitations are found by performing a DFT on the vector $[a]$, as discussed in Section 2.4.1. It should be noted that this formulation implicitly accounts

Table 5.3: Geometrical parameters of the three-armed spiral

Parameter	Value
Outer Diam.	50.8 mm
Inner Diam.	4.7 mm
Growth Rate a	0.127/rad (3 turns)
Subst. Type	RT/Duroid 6002
Subst. Thickness	508 μm (nom.)

for the unequal modal impedances of the spiral.

5.4 Single-Null Placement

Given the constraint that spiral Mode 0 be unused, the simplest nulling situation is that where only a single null is placed in the radiation pattern of the antenna. For this a minimum of three arms are needed. To validate the null placement approach, a three-armed spiral is designed and fabricated, and the relevant parameters are given in Table 5.3. The spiral is fed at the bottom with a bundle [29] of three soldered-together semi-rigid 85mil-diameter coaxial cables. Three vias in the spiral center allow the central conductors of the cables to pass through the substrate and be soldered to the three spiral arms (Fig. 5.3). The antenna is measured using the spherical near-field antenna testing facility at the University of Colorado. Measured data are collected for each individual arm of the spiral, with the unused ports terminated in 50Ω loads. From this data the complex mode patterns of the antenna are derived [32]. Since nulls in the RHCPpattern are desired, the RHCPcomponent $F_m^{RH}(\theta,\phi)$ of the pattern is used in (5.1) as follows

$$\begin{bmatrix} 1 \\ 0 \end{bmatrix} = \begin{bmatrix} F_1^{RH}(\theta_1,\phi_1) & F_2^{RH}(\theta_1,\phi_1) \\ F_1^{RH}(\theta_2,\phi_2) & F_2^{RH}(\theta_2,\phi_2) \end{bmatrix} \cdot \begin{bmatrix} a_1 \\ a_2 \end{bmatrix} \tag{5.3}$$

where the RHCPfield at point (θ_1,ϕ_1) is normalized to unity, and the RHCPfield at (θ_2,ϕ_2) is forced to vanish. For the purposes of demonstration the normalization point is chosen to be $(\theta_1 = 0°, \phi_1 = 0°)$ and the null point is chosen to be $(\theta_2 = 30°, \phi_2 = 60°)$. The resulting mode vector at 8.3 GHz, for example, is

$$[a] = [1.000 \angle 99.4° \quad 1.017 \angle -70.2°]^T \tag{5.4}$$

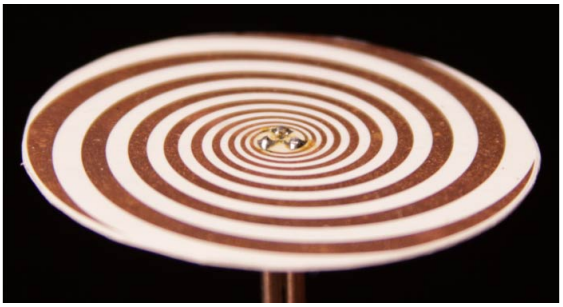

Figure 5.3: Photograph of a coaxial-bundle-fed three-armed spiral used for experimental validation of the single-null case.

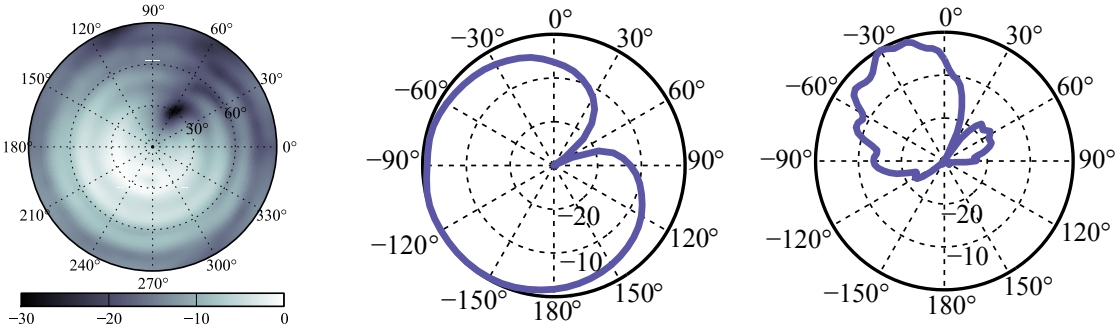

(a) Upper Hemisphere (b) $\theta = 30°$ conical cut (c) $\phi = 60°$ planar cut

Figure 5.4: Measured RHCPpartial pattern cuts at 8.3 GHz for a three-armed spiral with a null at $(\theta = 30°, \phi = 60°)$. Patterns are synthesized using the superposition of individual arm-measurement data.

where the mode vector has been normalized with respect to the Mode 1 amplitude. Transformation back to the arm domain is accomplished by left-padding the mode amplitude vector with a single zero in the first position, and then applying the DFT. The resulting weights are (normalized to the first arm)

$$[a_{arm}] = [1.00 \angle 9.19° \quad 9.03 \angle 15.0° \quad 10.0 \angle -165.6°]^T \tag{5.5}$$

These weights are applied to the arms of the spiral by multiplying each arm weight by each complex arm pattern, and superimposing the weighted patterns. The resulting pattern is seen in Fig. 5.4(a). Conical and planar cuts of the pattern are shown in Figs. 5.4(b) and 5.4(c), highlighting the precise position and depth of the null. The resulting pattern has been squinted to $(\theta = 30°, \phi = -120°)$ due to the corresponding constructive interference of Mode patterns 1 and 2.

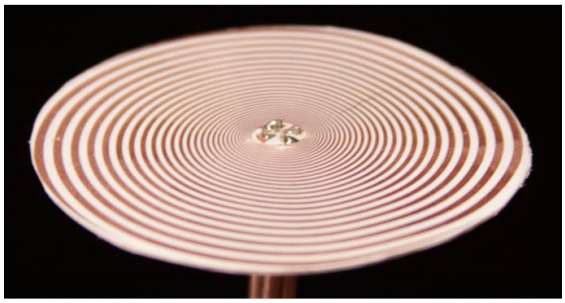

Figure 5.5: Photograph of the fabricated coaxial-bundle-fed four-armed spiral used to experimentally demonstrate two-null placement.

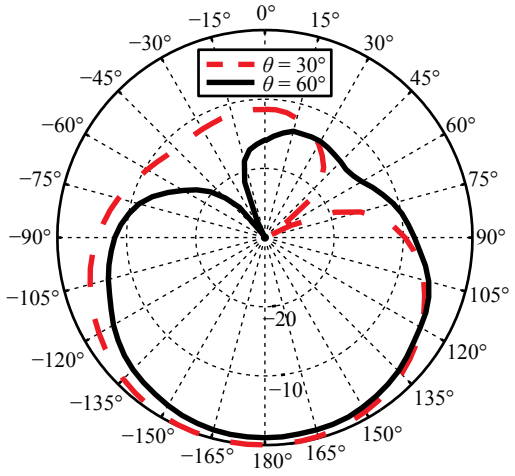

Figure 5.6: RHCP partial pattern cuts at 6.7 GHz for a four-armed spiral with two nulls. Patterns are synthesized using superposition of individual arm-measurement data.

5.5 Multiple Nulls

Extension to multiple-null placement is accomplished simply by adding to the number of modes considered in the evaluation of (5.1). The most commonly-used multi-armed spirals with four and eight arms are used next to practically demonstrate and validate the proposed technique.

5.5.1 Four-Armed Spiral

A four-armed spiral is constructed using the parameters of the previously-discussed three-armed spiral, except that the inner radius has increased to 5.2 mm(to accommodate the four-cable bundle), while the growth rate has been reduced to 0.052/rad (yielding seven turns). The antenna is measured in the far-field

antenna testing facility at Lockheed Martin Space Systems Company in Denver, CO, where again individual port pattern data are collected. Matching at the normalization point and at the null points is performed as follows

$$\begin{bmatrix} 1 \\ 0 \\ 0 \end{bmatrix} = \begin{bmatrix} F_1^{RH}(\theta_1,\phi_1) & F_2^{RH}(\theta_1,\phi_1) & F_3^{RH}(\theta_1,\phi_1) \\ F_1^{RH}(\theta_2,\phi_2) & F_2^{RH}(\theta_2,\phi_2) & F_3^{RH}(\theta_2,\phi_2) \\ F_1^{RH}(\theta_3,\phi_3) & F_2^{RH}(\theta_3,\phi_3) & F_3^{RH}(\theta_3,\phi_3) \end{bmatrix} \cdot \begin{bmatrix} a_1 \\ a_2 \\ a_3 \end{bmatrix} \tag{5.6}$$

The normalization point is chosen to be $(\theta_1 = 0°, \phi_1 = 0°)$, and the null points are chosen to be $(\theta_2 = 30°, \phi_2 = 60°)$ and $(\theta_3 = 60°, \phi_3 = -30°)$. The resulting mode vector at 6.7 GHz is

$$[a] = [1.00\angle -105.8° \quad 1.45\angle -81.1° \quad 1.15\angle 54.1°]^T \tag{5.7}$$

and the corresponding transformed arm excitation vector is

$$[a_{arm}] = [1.00\angle -66.7° \quad 2.00\angle 131.7° \quad 0.89\angle -97.3° \quad 1.10\angle 16.0°]^T \tag{5.8}$$

The measured conical pattern cuts at $\theta = 30°$ and $60°$ are shown in Fig. 5.6, once again showing excellent placement accuracy as well as agreement with theory.

5.5.2 Eight-Armed Spiral

As a final example of multiple-null placement, an eight-armed spiral (Fig. 5.7) is simulated in **FEKO** [25]. For this example six nulls are arbitrarily chosen to be located at the (θ, ϕ) locations (50.6°, 33°), (101.3°, 39°), (151.9°, 45°), (202.5°, 51°), (253°, 57°), and (303.8°, 63°). Applying the algorithm at $12f_0$, the normalized mode vector is obtained as

$$[a_{arm}] = [1.00\angle 89.5° \quad 0.75\angle 138.8° \quad 0.73\angle 56.0° \quad 0.78\angle 26.0° \quad 0.88\angle 126.0° \quad 0.99\angle 46.1° \quad 1.13\angle -171.2°]^T \tag{5.9}$$

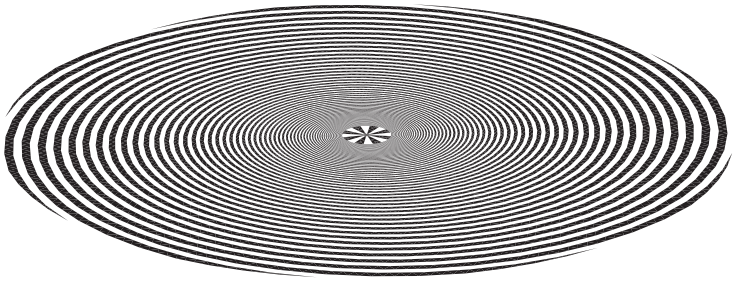

Figure 5.7: **FEKO**-simulated eight-armed spiral in free space.

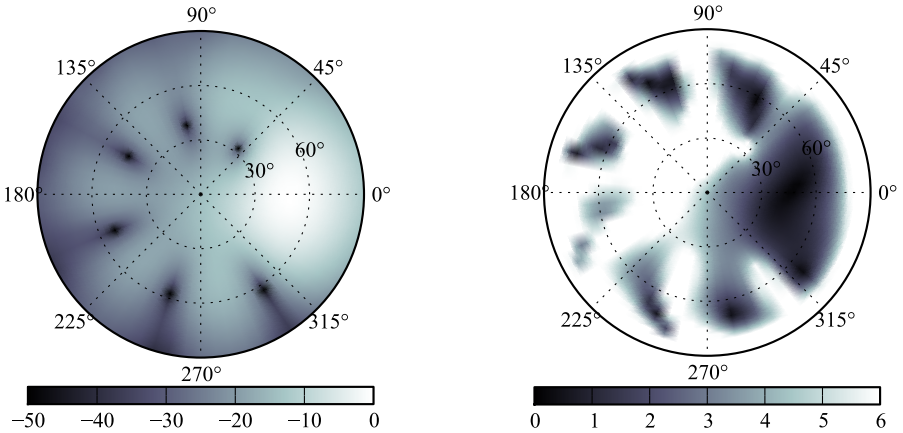

(a) Co-polarized directivity (b) Axial ratio

Figure 5.8: **FEKO**-simulated hemispherical RHCPdirectivity (a) and axial ratio (b) patterns for an eight-armed spiral at $12f_0$ showing precise null placement while maintaining low main-beam cross-polarization.

with the corresponding normalized arm excitation vector

$$
\begin{aligned}
[a_{arm}] = \\
&[1.00\angle 95.9^\circ \quad 0.34\angle -134.4^\circ \\
&0.58\angle -29.6^\circ \quad 0.77\angle -70.1^\circ \\
&0.57\angle -16.4^\circ \quad 0.77\angle 109.9^\circ \\
&0.26\angle -136.5^\circ \quad 0.54\angle -165.9^\circ]^T
\end{aligned} \tag{5.10}
$$

The resulting upper-hemisphere RHCPpartial pattern at $12f_0$ is shown in Fig. 5.8(a), showing not only precise null placement, but also a pattern free of grating lobes. The latter two observations are remarkable considering the broad bandwidth and high frequency, and are due to the fact that the phase centers of

the various active regions are highly co-located [3, 54]. Finally, the projected upper-hemisphere axial ratio pattern plotted in Fig. 5.8(b) shows that a low value, AR < 2 dB, is maintained over the main lobe.

5.6 Discussion

Having covered the basic algorithm behind multi-armed spiral antenna nulling, there are practical considerations that affect the applicability of the concept in antenna systems. Of particular importance are the effects of frequency-dependent null rotation and mode cutoff.

5.6.1 Null Rotation

As shown in the preceding discussion, the amplitude and phase of the mode vector elements, and therefore the arm vector elements, are functions of frequency. This is in part due to the changing number of radiating active regions, but is mainly due to the rotation and scaling property of the spiral antenna. As frequency is increased on a right-handed spiral, for instance, the active regions shrink and rotate clockwise, as do their respective patterns. To counteract this, it is necessary to adjust the relative phasing of the modes which, as discussed in Section 5.2, rotates the nulls back into their original position. Therefore, to provide a frequency-independent null, it is necessary to introduce a frequency-**dependent** mode phase shift. Depending on the technology used to feed the antenna this may or may not pose a substantial hurdle to the adoption of the technique.

Perhaps the most precise and conceptually simplest method involves a lookup table embedded in a digital processor that is used to adjust the null position as a function of frequency by solving (5.1) at each frequency point. Fig. 5.9 shows the null stability of the eight-armed spiral from Fig. 5.7 obtained by applying this method. To implement this method generally one would need to store the mode field information for each frequency and possible null points of interest, so that (5.1) could be solved, yielding $[a]$ as a function of frequency. Since the processing power involved in this calculation over wide bandwidths could be substantial, in certain circumstances it could be beneficial to incorporate this function into a passive RF mode-forming network.

Owing to the fact that multi-armed spirals have been used for many years for radio direction finding

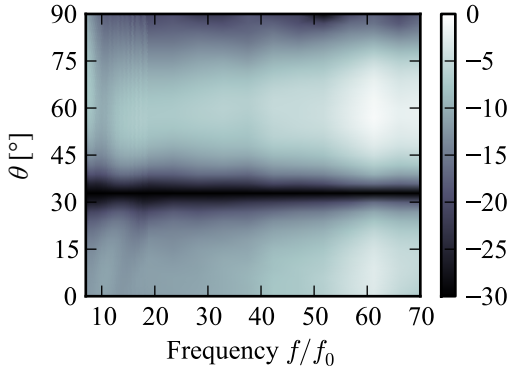

Figure 5.9: **FEKO**-simulated directivity pattern versus frequency of the eight-armed spiral discussed in Section 5.5.2, highlighting the high degree of nulled-pattern stability, with an over 30 dB deep null at 33°.

purposes, methods for accomplishing this task have been developed, with some outlined in [12]. For modest bandwidths, one method introduces delay lines into the mode inputs. Fig. 5.10 shows that the mode phase difference is roughly linear over a 1.4:1 bandwidth, with a slope of approximately −71°/GHz, suggesting that delay-line compensation may be useful. Fig. 5.11(a) shows the result of applying (5.1) at 7 GHz only for the three-armed spiral discussed in Section 5.4. The null position rotates with frequency, owing to the scaling and rotation properties of the spiral antenna as noted earlier. However, if a 4 cm-length of PTFE-filled ($\epsilon_r \approx 2.18$) coaxial cable (having −71°/GHz phase slope) is inserted into the Mode 1 channel of a three-arm, two-channel (Modes 1 and 2) spiral RF mode-forming network, then the null location versus frequency is equalized (Fig. 5.11(b)). An additional fixed 136° phase offset is then needed to compensate for the delay line effect at 7 GHz, which can be applied in the processor to avoid the use of an RF phase-shifter. This compensation is done at the expense of some null depth and frequency-flatness, since the mode amplitude-ratios are (presumably weak) functions of frequency. For wider bandwidths, an additional distortion of the spiral shape may be used to linearize the mode phase difference [12] and therefore achieve more accurate null compensation.

5.6.2 Mode Cutoff

For a spiral to radiate all modes efficiently the spiral diameter D must be larger than $M\lambda/\pi$, where M is the largest spiral mode excitation. Since the maximum realizable number of broadband nulls N_{nulls}

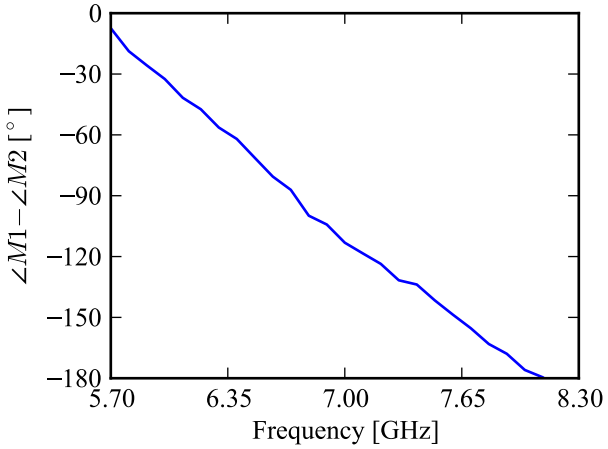

Figure 5.10: Measured mode phase difference $\angle M1 - \angle M2$ versus frequency for the null-movement-compensated pattern of the three-armed spiral of Section 5.4. The linear phase slope suggests that the delay-line compensation technique may be applicable.

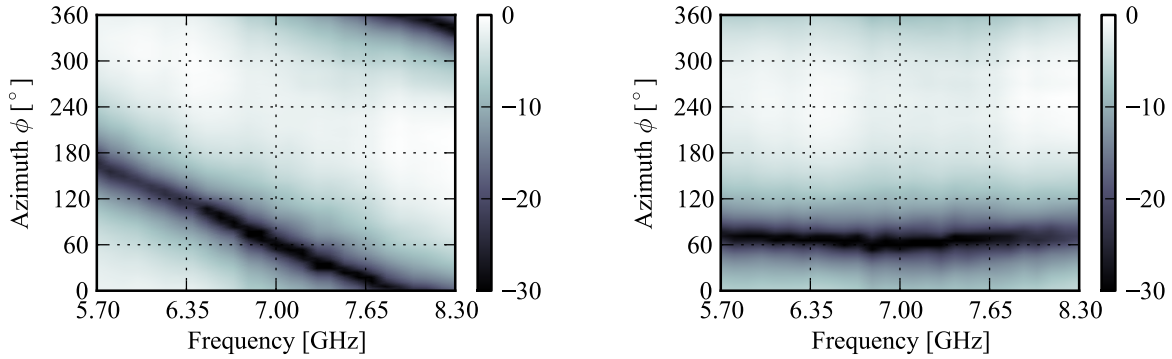

(a) Uncompensated

(b) Delay-line Compensated

Figure 5.11: Measured three-armed spiral null location with (5.1) evaluated at 7 GHz. (a) The uncompensated null has a slope similar to that shown in Fig. 5.10. (b) Improved null flatness using delay-line compensation. Patterns are synthesized using superposition of individual arm-measurement data.

is equal to $M - 1$, then the condition $N_{nulls} \leq D\pi/\lambda - 1$ governs the number of broadband (in the sense of frequency independence) nulls that can be placed. Otherwise, the ratio of maximum to minimum mode amplitude becomes very large (Fig. 5.12), which makes accurately placing the nulls difficult by worsening the condition of the problem.

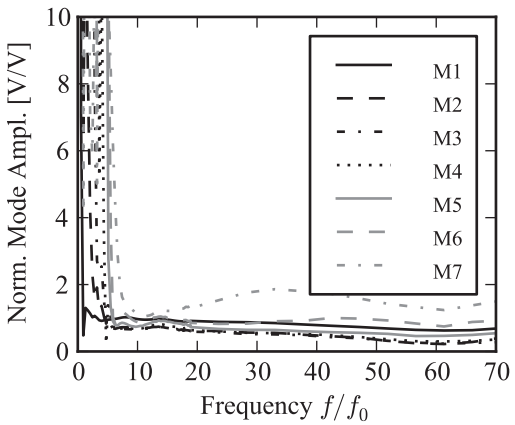

Figure 5.12: Normalized mode amplitude (with respect to Mode 1 at $7f_0$) of the eight-armed spiral with null configuration as discussed in Section 5.5.2. Cut-off modes must have large relative amplitudes in order to maintain a fixed null count. This phenomenon imposes practical limits on the number of broadband nulls that can be placed using a spiral of given diameter.

5.7 Conclusions

In this chapter a simple method of achieving arbitrary null placement using a single multi-armed spiral aperture is discussed. The method uses an N-armed spiral to achieve simultaneous nulling of $N-2$ interferers, provided that all $N-1$ fundamental phase modes are radiated efficiently. Since the spiral aperture must be $m\lambda/\pi$ in diameter to radiate the mth phase mode efficiently, the maximum number of nulls that can be practically formed is less than or equal to approximately $\pi D/\lambda - 1$. Null formation using phase modes is demonstrated computationally for an eight-armed spiral using **FEKO** and through ideal beam-formed measurements of three- and four-armed spiral antennas. Furthermore, it is shown that constant null position versus frequency is achieved when the mode weights are adjusted accordingly. Delay-line compensation has been shown to provide a practical means of achieving this weight adjustment over modest bandwidths.

Chapter 6

A Low-Cost, 18-40 GHz Antenna with a Consistent Radiation Pattern

6.1 Introduction

Throughout this thesis antenna performance enhancement has been accomplished by controlling the mode spectrum radiated by the antenna. Until this point in the thesis the antennas under consideration have been spiral antennas. In this chapter the idea of mode spectrum control has been applied to a different class of antenna; namely, the horn antenna.

There is a current need for a antennas that have a broad and consistent radiation pattern, high power handling, wide bandwidth, compact size, and low cost. The power handling capability is beyond what is likely to be achievable with spiral antennas, and so a different type of antenna must be considered. Fortunately, the bandwidth requirement (K- to Ka-band) is much narrower than the antennas previously considered in this thesis, allowing adequate trade between bandwidth and power handling to occur.

The objective of this research is to design and demonstrate a K- to Ka-band broad-beam horn antenna and to develop a low-cost prototype fabrication technique, that can be easily extended to high power-handling capability. The design uses a quad-ridged horn configuration to achieve an aperture with 60° average half-power beamwidth, a beam with excellent azimuthal uniformity, and good impedance match. Vertically-stacked printed circuit board (PCB) plated slots are utilized to realize the designed cross section of the horn antenna. This fabrication approach is not only low-cost, but it is also flexible in terms of developing a prototype that is ready for direct system or measurement application. The developed design compares favorably in terms of bandwidth with another low-cost waveguide fabrication technique known as substrate

integrated waveguide [55]. Good performance compared to the design goals is demonstrated, as well as excellent agreement between measurement and simulation.

The state of the art in this class of antennas is exemplified by the Cobham 290HC2 antenna. This antenna has a power handling capability of 100 W over a bandwidth of 18-40 GHz and a double-ridged waveguide input. However, this antenna requires use of fabrication techniques that cause the expense of the antenna to be prohibitive for certain applications. The antenna described in this chapter represents nearly two orders of magnitude in cost reduction when compared to the existing commercial state of the art. This huge reduction in cost could enable new applications for this class of antennas, as well as enabling effective means for prototyping millimeter-wave circuits and antennas.

This chapter is organized as follows. Section 6.2 examines at length the relationship between the design objectives and various antenna characteristics. Section 6.3 details the design of the antenna, while Section 6.4 describes the fabrication process. Finally, Section 6.5 presents the measured performance of the antenna.

6.2 Relation of Antenna Design Objectives to Antenna Characteristics

The antenna design has the following requirements. The half-power beamwidth (HPBW) is to have a nominal value of at least 60°, while possessing an instantaneous bandwidth of 18-40 GHz. The average power handling capacity is to be maximized, with a limit determined by the feed line rather than the aperture. To facilitate interfacing with solid-state power amplifiers, the input interface is a 2.92 mm (K) coaxial connector [56]. The polarization of the antenna is linear, but it is highly desirable to have the option to upgrade to circular polarization in the near future. The occupied physical volume and cost of the antenna are to be minimized, subject to the previously-named constraints.

The objectives for the design of the antenna are summarized in Table 6.1. From the table it is readily observed that the power handling objective affects all five of the listed antenna characteristics, and that bandwidth affects four. This suggests that a successful antenna design would derive from an antenna with inherently high power handling and adequate bandwidth. Therefore, Table 6.1 aids in the antenna design by helping to identify and prioritize the core design objectives.

Table 6.1: Prioritized driving design objectives versus anticipated driven design characteristics.

Priority	Objective	Trans. Medium	Aperture Shape	Aperture Size	Beamforming Approach	Mfg. Tech.
1	Power Handling	X	X	X	X	X
2	Bandwidth	X	X	X	X	
3	Beamwidth		X	X		
4	Form Factor				X	
5	K-connector input	X				
6	Polarization		X		X	
7	Cost					X

6.2.1 Relation of Aperture Shape to Antenna Design Objectives

There are a variety of antenna apertures that may be used in the antenna design; linear slot (e.g. dipole on a screen), annular slot, circular, rectangular, ridged, spiral, and sinuous are just a few examples. As is well known, each type has unique characteristics and associated trade-offs. Instead of comparing a large number of possible configurations, generally three have been selected for comparison: the spiral, rectangular, and quadruple-ridged apertures.

6.2.1.1 Relation of Aperture Shape to Power Handling

The average power handling capacity of an aperture in a metallic screen is maximized by making the current density as uniform as possible over all metallic surfaces. In a center-fed logarithmic spiral antenna, the current density tends to be much higher in the center than at the outside. Furthermore, the curved shape of the spiral arms forces the currents to travel in a circuitous path, causing yet more loss to occur. The heat that is generated along the spiral arms typically must be dissipated toward the outside of the aperture; consequently, the heat must conduct along the same circuitous path, thereby increasing the overall thermal resistance and therefore temperature near the center.

For sufficiently narrow bandwidths, a waveguide aperture provides the possibility for higher power handling. Since currents flow only along the outside of the aperture the current density is lower, generating less heat than concentrated currents would generate. Furthermore, since the heat is generated along the outside of the aperture, it can be dissipated radially, which is the most direct path possible.

6.2.1.2 Relation of Aperture Shape to Bandwidth

As is well-known, the widest possible bandwidth is obtained with an aperture shape belonging to the frequency-independent (FI) family of apertures (e.g. spiral, sinuous, log-periodic). However, FI shapes inherently incorporate spiraling or meandering current paths, which present challenges in the thermal management of the aperture, as discussed earlier. In contrast, the bandwidth of a waveguide aperture can be sufficiently broadened by introducing ridge loading in various configurations. These ridges serve to distort the mode spectrum of the waveguide, pushing undesired higher-order modes higher in frequency.

As a consequence of their desired function of increasing bandwidth, the introduction of ridges distorts the mode field structure, creating regions of increased tangential magnetic field. This tendency is especially evident in the gaps between ridges. The increased magnetic field intensity means higher current density on the ridges, and consequently leads to increased loss and decreased power handling. Careful shape optimization should be performed so that the ridges have the proper dimensions such that the necessary bandwidth is achieved while maintaining sufficiently high power handling capacity [57].

6.2.1.3 Relation of Aperture Shape to Beamwidth

The beamwidth of a planar, Mode 1, frequency-independent aperture is typically broad, because of the fairly small diameter $D \approx \lambda/\pi$ of the active region. A rectangular aperture also has a broad beamwidth near the cutoff frequency; however, the beamwidth quickly narrows as frequency is increased, since the aperture field is rather broadly distributed (for a TE_{10} mode). As a side-effect to increasing the single-mode bandwidth, ridge loading also tends to increase the beamwidth as a result of the fields becoming more concentrated to the region between the ridges, decreasing the effective size of the aperture.

6.2.2 Aperture Size

6.2.2.1 Relation of Size to Power Handling

Due to reduced current density and therefore lower power lost, a large aperture will generally have a higher power handling capacity than a small aperture, given a similar mode structure. Therefore the design

of the aperture for power handling seeks to maximize its size, subject to other constraints.

6.2.2.2 Relation of Size to Beamwidth

As discussed in [58], there is a fundamental relation between the physical size of an antenna aperture and its associated half-power beamwidth (HPBW). That is, the smaller the effective aperture in a given dimension, the wider the HPBW in that dimension. Therefore, in order to realize a broad-beam aperture over a broad bandwidth, the effective aperture must not become too electrically large in any dimension. In [58], the HPBW of a rectangular aperture mounted on an infinite ground plane was found to be $50.6°\lambda/b$ for the E-plane and $68.8°\lambda/a$ for the H-plane (if a and b are taken to be the major and minor dimensions of the aperture). If one attempts to meet a minimum beamwidth of 60° over an octave of bandwidth with this aperture, it is found that the necessary dimensions to meet the upper-frequency HPBW requirement cause the antenna to cut off well above the lowest desired operational frequency.

6.2.2.3 Relation of Size to Bandwidth

Furthermore, reducing the physical aperture tends to increase the susceptance of the aperture relative to its conductance [59], increasing quality factor Q of the aperture. Through the Bode-Fano criterion [60], this increases the difficulty of obtaining an acceptable broad-band impedance match of the antenna.

6.2.3 Transmission Medium

6.2.3.1 Relation of Transmission Medium to Power Handling and Bandwidth

The average power handling capacity of a transmission line is generally limited by the maximum tolerable temperature of its constituent materials [61, 62]. This temperature is influenced by the following factors:

- the ambient temperature
- the heat generated per unit length in the line due to loss power
- the ability to transfer this heat away from the constituent materials

Table 6.2: Comparison of 85 mil-diameter M17-standard semi-rigid coaxial cable variants manufactured by Micro-Coax, Inc. at 20 GHz [1]

Model Number (UT-)	PTFE Diel. Type	Outer Conductor Type	Power Handling [W]	IL @ 20 GHz [dB/m]	Max. Op. Temp. [° C]
085-M17	Solid	Copper	20.0	4.27	125
085-SS	Solid	Stainless Steel	21.5	6.94	200
085C-SP	Solid	Silver-Pl. Copper	24.3	3.29	125
085C-EDS9010-LL	Foamed	Tin-Pl. Copper	34.9	2.71	175
085C-AL-TP-LL	Foamed	Aluminum	40.1	2.92	225
085C-TP-LL	Foamed	Tin-Pl. Copper	43.0	2.71	225
085-CUSS	Solid	Stainless/Copper	43.2	3.29	250
085C-LL	Foamed	Copper	50.0	2.71	250

and the attenuation of a coaxial cable is influenced by these factors:

- the cross-sectional area of the coaxial cable
- the conductivity of the inner and outer conductor materials
- the loss tangent of the dielectric material

For typical choices of materials, the dielectric and inner conductor loss dominates over the loss in the outer conductor. However, all three components of the cable affect the power handling. Table 6.2 compares the power handling of some minor variants of the 85 mil diameter (the largest-diameter cable having single-mode operation to 40 GHz) standard M17 50 Ω PTFE-filled semi-rigid coaxial cable manufactured by Micro-Coax, Inc.

On the other hand, while the rectangular waveguide has excellent power handling capacity (Table 6.3), the bandwidth is insufficient for the desired application. Fortunately, ridged waveguide presents a third alternative that provides a fortuitous tradeoff between bandwidth and power handling capacity (Table 6.3, last row).

Table 6.3: Comparison of standard rectangular waveguides and double-ridged waveguides made of various materials manufactured by Advanced Technical Materials, Inc. [2]

Waveguide Designation	Freq. Range (GHz)	Material	Inside Dimension	Avg. Power Handling [W]	Atten. (High Freq) [dB/m]
WR42	18-26.5	Copper	0.42x0.17	800	0.33
WR42	18-26.5	Aluminum	0.42x0.17	600	0.50
WR28	26.5-40	Copper	0.28x0.14	500	0.52
WR28	26.5-40	Aluminum	0.28x0.14	400	0.77
WRD180C24	18-40	Al. Alloy		500	1.17

6.2.4 Manufacturing Technology

6.2.4.1 Relation of Manufacturing Technology to Power Handling Capacity

As discussed earlier, the average power handling capacity of a transmission line or waveguide is limited by its ability to efficiently dissipate loss heat away from the current-carrying conductor surfaces. For a hollow metallic waveguide, a favorable (though unrealistic) scenario would be to have the waveguide embedded in an infinite metallic block, where heat could conduct away radially. A realistic version of this would involve truncation of the infinite metallic block with a heat-exchanging medium; for example, liquid cooling, forced air, or radiative transfer. However, manufacturing antennas from solid blocks of metal tends to be relatively expensive and time-consuming compared to manufacturing antennas using commodity PCB processes. However, PCB has inferior thermal conductivity compared to most materials. While PCB may not be suitable for very high power-handling applications, PCB does provide an excellent technology for quickly realizing very low-cost prototypes, as described in the next section.

6.2.4.2 Relation of Manufacturing Technology to Cost

PCB has some important benefits when attempting to realize low-cost antenna prototypes. Since PCB manufacturing often requires fine feature sizes, the process is inherently precise, made possible by the high level of automation found at most PCB makers. Furthermore, it is a commodity process; consequently, there are many potential low-cost, quick turn-around suppliers from which the designer can choose. To keep the broadest possible selection of suppliers, it is important that the designer attempts to use design features

that are supported by the widest-possible variety of vendors. That is, techniques that are only available through specialized sources should be avoided if possible.

Another important consideration is scalability. While the realized cost benefit of PCB fabrication may be modest for prototype-scale quantities, the cost advantage of PCB technology quickly becomes appreciable when scaling up to medium- to large-quantity production runs. In this respect, PCB techniques are exemplary: manufacturers routinely scale production into hundreds of thousands of units with low recurring costs.

6.3 Antenna Design

6.3.1 Aperture Design

The primary objective is to design an aperture with an expected power handling greatly exceeding the limit imposed by the feed line, with a nominal half-power beamwidth (HPBW) of at least 60° over the 18-40 GHz band, while being suitable for dual-orthogonal polarized operation. For this, an aperture design based on open-ended quadruple-ridged waveguide was chosen. Being a waveguide-based design, power handling is expected to be ample. The four-fold symmetric design assures that the aperture can adequately provide both dual-orthogonal linear polarization as well as dual circular polarization. For linear polarization the Ludwig-3 definition [63] of polarization is used.

A numerical parameter study was performed in **HFSS** [64] that achieved an average HPBW of at least 60° over 18-40 GHz while obtaining a high degree of azimuthal beam uniformity, acceptably low VWSR, and little degradation in anticipated power-handling capability. An aperture design with acceptable performance was found to be the quad-ridged design shown in Fig. 6.1. The HPBW and its spread are shown in Fig. 6.2. The HPBW ranges from about 120° near the low end of the frequency range to around 50° at the high end. The HPBW averages to about 70° over azimuth and frequency combined, which is acceptable for the application. An even wider beamwidth would be desirable; however, a smaller aperture would be needed, leading to difficulty in achieving acceptable impedance bandwidth due to increase in the aperture Q. A useful feature of this aperture is that its pattern is relatively uniform with respect to azimuth, as shown in

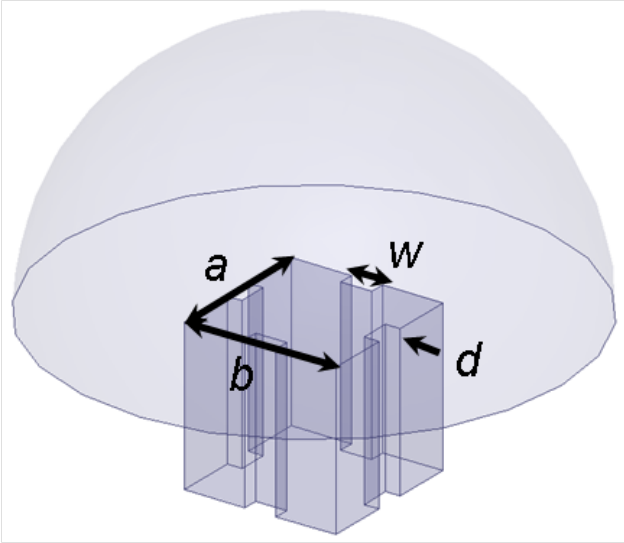

Figure 6.1: **HFSS** model of the aperture. The aperture is fed at the bottom of the model using the lowest-order quadruple-ridge waveguide eigenmode excitation. The lower surface of the hemisphere represents the metal body of the platform, while the upper surface represents the radiation boundary that truncates the FEM solution domain. a and b represent the respective major and minor maximal dimensions of the aperture, while w and d represent the respective ridge width and depth.

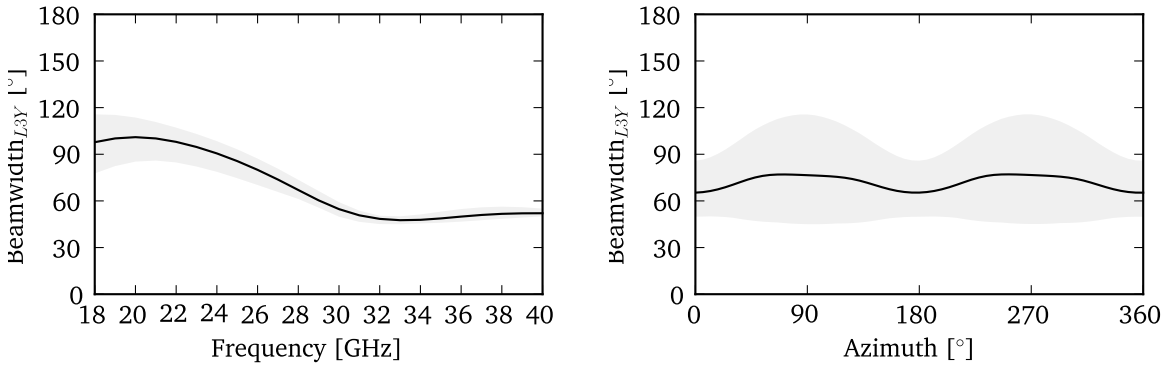

(a) HPBW with respect to frequency and its spread with respect to the azimuth variable ϕ.

(b) HPBW with respect to ϕ and its spread with respect to frequency.

Figure 6.2: Ludwig-3 beamwidth of the quad-ridged aperture.

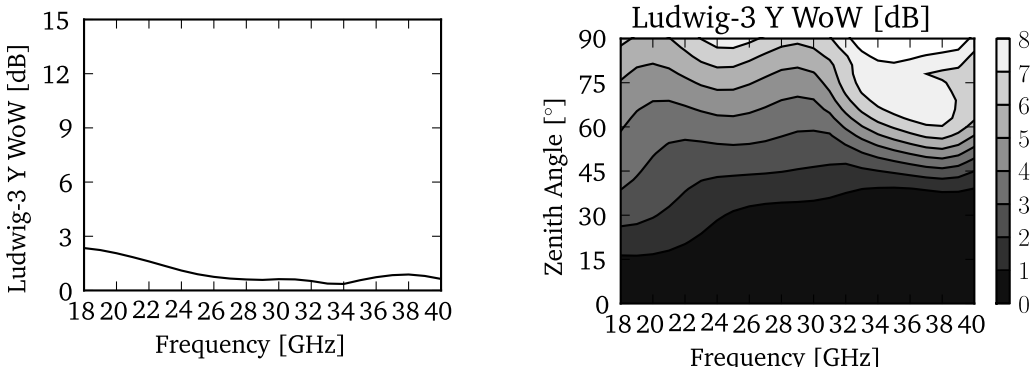

(a) WoW at $\theta = 30°$ (broadside is $\theta = 0°$).

(b) WoW over the entire upper hemisphere

Figure 6.3: WoW vs. frequency (with respect to Ludwig-3 polarization) of the quad-ridged aperture. WoW is better than 3 dB over the entire band and beyond $\theta = 30°$.

Figs. 6.3(a) and 6.3(b). The WoW is below 3 dB within 30° from broadside throughout the 18-40 GHz band. This characteristic makes the antenna useful in the single linear-polarized mode of operation.

6.3.2 Double-Ridged Waveguide to Quad-Ridged Aperture Transition

Due to its high power-handling capability and suitable bandwidth, the WRD180C24 double-ridged waveguide is a suitable choice as a feeder transmission line for single linear-polarized operation. A simple and easily-fabricated transition from double-ridged to quad-ridged waveguide is the taper. In this transition, the features of the quadruple-ridged waveguide are first mapped onto the features of the double-ridged waveguide, with a suitable taper function then used to realize the transitioning structure (Fig. 6.4). The quality of the broadband match is limited by the following factors: the overall length of the taper, the choice of taper function, and the Q of the aperture.

The simplest reasonable taper function, in terms of the number of design variables, is the linear taper. From a manufacturability perspective, this type of transition is unique in that it is the only transition function that can be practically realized using the wire electric discharge machining (EDM) technique.

In the EDM technique, the transition is fabricated using an electrically-charged wire threaded through a hole in the material. When this wire contacts the blank material, the resulting electrical discharge vaporizes a small amount of the blank material. The wire is then recharged and moved a small distance until contact and discharge occurs again. If both ends of the wire are independently controlled, complex apertures can be

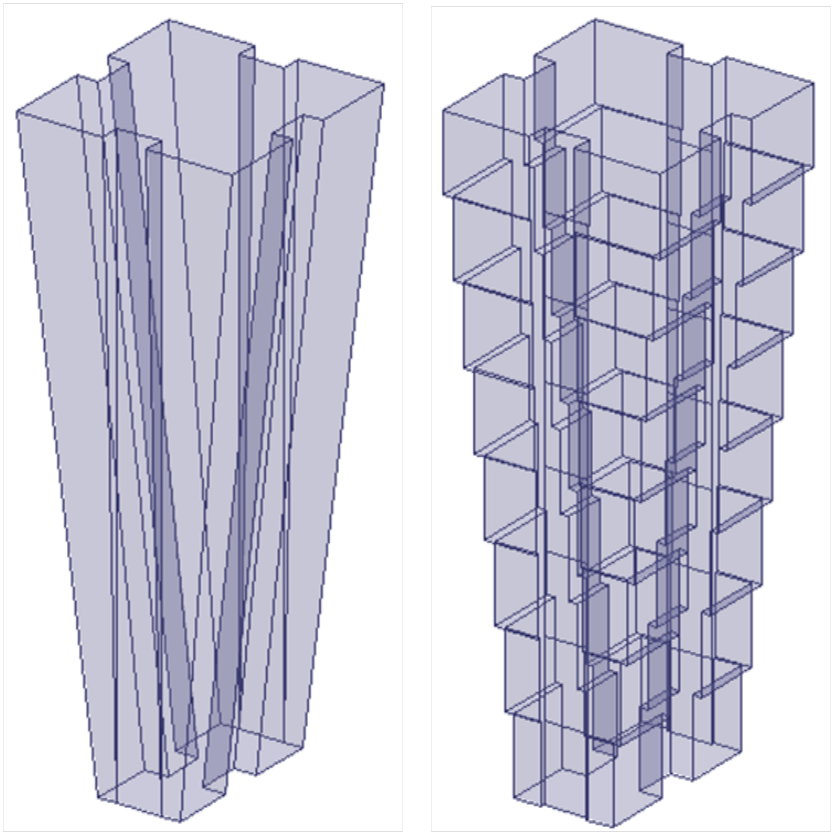

(a) Linear taper (b) Stepped realization

Figure 6.4: (a) Linear taper used to transform double-ridged waveguide to quad-ridged waveguide. (b) Stepped approximation of the linear taper.

easily and precisely cut out with smooth linear blending between shapes on the two sides of the material. This technique is ideal for producing linear tapers in bulk metallic material. More complex tapers can require involved and expensive manufacturing techniques.

In the linear taper the only design variable is the taper length L, which controls the lowest operational frequency as well as the worst-case match. A study was performed in **HFSS** comparing the performance of various taper lengths. It was found that a 2.54 cm long taper produced an acceptable lowest cut-off frequency while providing an acceptable (< 2:1) VSWR level (Fig. 6.5(a)).

Some fabrication technologies, such as the PCB stacking technique proposed in this chapter, must approximate the linear taper as a series of piecewise constant steps. The cost can be minimized by keeping the number of steps to a minimum. A numerical study was performed on the 2.54 cm long taper in **HFSS**, where tapers with four, eight, and sixteen steps were simulated (Fig. 6.5(b)). The VSWR of the four-step variant has a large increase around 28 GHz since the step length becomes $\lambda_g/2$ near that frequency. The step length of the eight-step variant is half that of the four-step variant, so the VSWR bump has been moved out of the band. Of the studied variants, the eight-step transition provides the best trade-off between complexity and performance. The VSWR has a nearly equi-ripple characteristic better than 1.7:1, which is adequate for the intended application.

6.3.3 Coax-to-Double-Ridged Waveguide Transition

The transition from WRD180C24 double-ridged waveguide to the quad-ridged aperture discussed in Section 6.3.2 is suitable for operation in a high average-power system, such as one fed by a traveling wave-tube amplifier (TWTA). However, most low- and medium-power antenna applications (utilizing solid-state power amplifiers (SSPAs)) in this frequency range use the 2.92 mm coaxial connector as the preferred interconnect. To extend the utility of the antenna to the low- and medium-power application domains, a transition from WRD180C24 to 2.92 mm is necesary. Furthermore, an end-launch version of such a transition would enable a laterally (i.e. orthogonal to the horn axis) compact realization of the antenna assembly. While WRD180C24-to-2.92 mm transitions are available commercially as machined units, their per-unit cost is high compared to what could be achievable using the stacked PCB technique. In this section, a WRD180C24 to 2.92

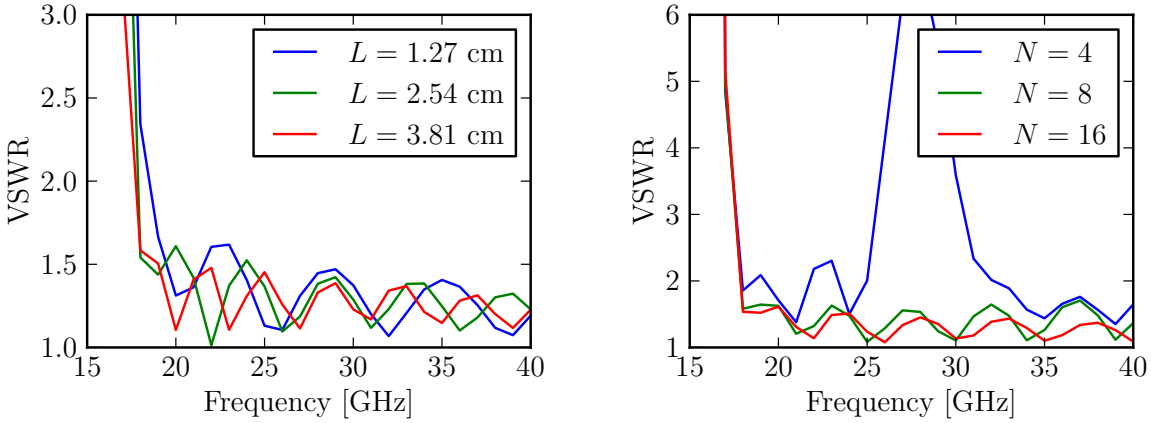

(a) Comparison of taper lengths

(b) Comparison of taper step counts

Figure 6.5: (a) Comparison of VSWR for three different trasition lengths. The 2.54 cm transition length is the shortest length that provides an acceptable VSWR over the entire 18-40 GHz band. (b) VSWR of the stepped realization of the 2.54 cm long tapered double-ridged to quad-ridged waveguide transition, for various numbers of steps. The eight-step transition has the best trade-off between performance and complexity.

mm transition is described, intended to be paired with the transition from Section 6.3.2 realized using the stacked-PCB technique. The resulting antenna is unique in that the individual layers can be fabricated on a single PCB panel, and can be assembled quickly by hand using commonly-available hardware. Furthermore, the antenna is structurally robust, compact, and has low material cost.

6.3.3.1 TEM-to-TE Mode Converter

The heart of the coax-to-waveguide transition is a waveguide section that converts the TEM mode of the coaxial input to the TE-type mode of the waveguide output. The essential objective is to distort the TEM mode on the input into a configuration that can be satisfactorily matched by a distorted TE mode on the output. This must be done while maintaining structure dimensions and tolerances that are compatible with the fabrication method of choice.

In this design the modes of the TEM and TE modes are distorted in such a way as to produce high field concentrations in a chosen area of the structure, to the near exclusion of field from other areas of the structure. The cross-section portions with high field concentrations are made continuous across the TEM-to-TE junction, while the portions with low field concentration can be made discontinous across the junction in order to accomplish the cross-section transformation. Effects of discontinuities are generally low where the field concentrations are low.

A critical design parameter is the center conductor diameter of the TEM side of the converter. The choice of this diameter is driven by performance considerations, but even more so by manufacturability constraints. The larger the diameter, the easier it is to obtain the field concentration necessary to obtain a high-quality transition. In the present design, a center conductor diameter of 508 μm was chosen, which is the largest center pin diameter that the Southwest Microwave 2.92 mm bulkhead connector series can accept.

The TEM side of the mode converter can be viewed to consist of a half-coax portion and a tall and narrow "recta-coax" portion (Fig. 6.6, left side). The half-coax portion achieves the highest possible field concentration while maintaining an acceptable minimum center-to-outer conductor distance needed for manufacturability. The recta-coax portion dimensions are chosen to achieve the lowest possible field

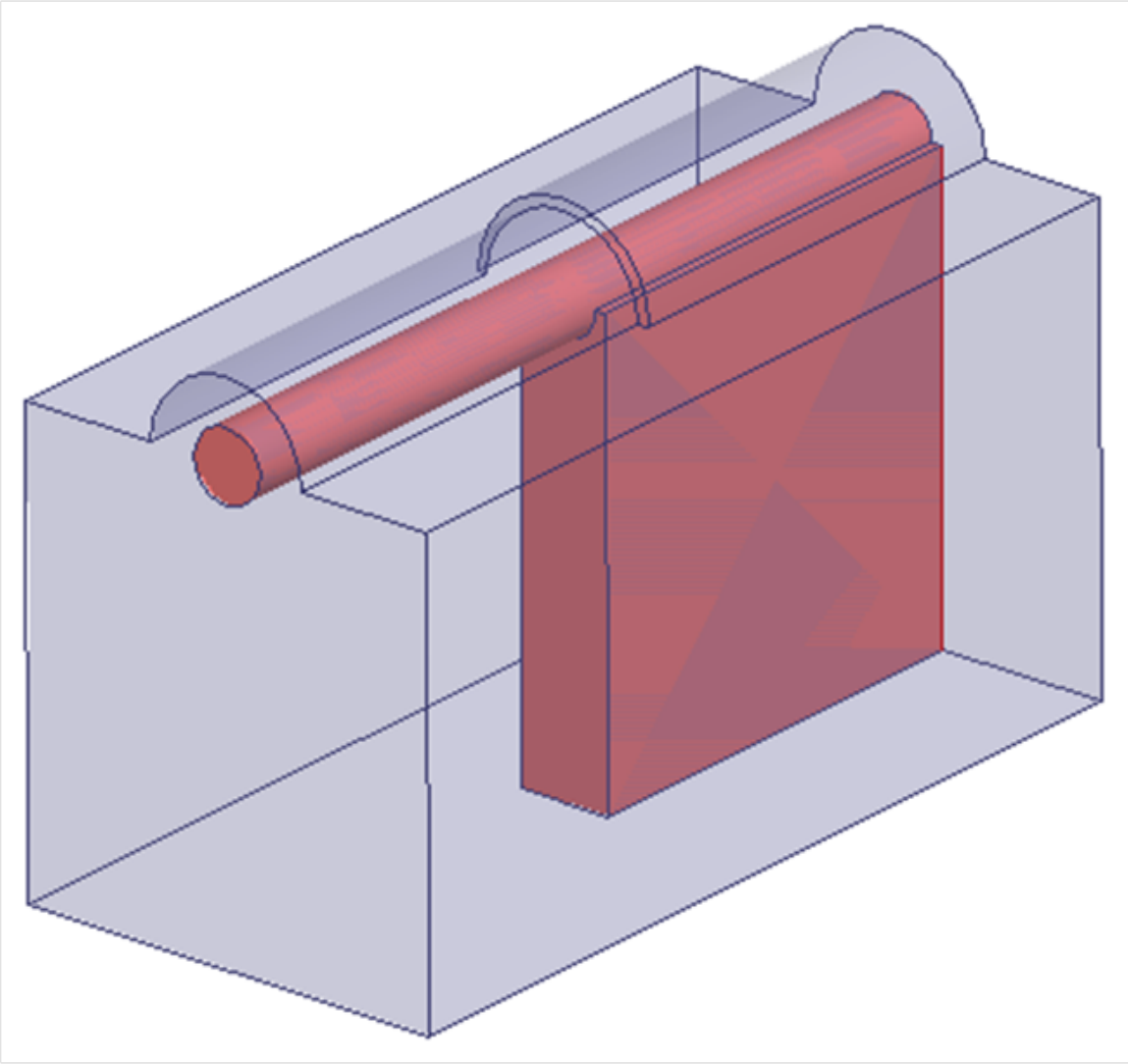

Figure 6.6: HFSS model of the TEM-to-TE mode conversion structure. On the left is the TEM input, and on the right is the TE output.

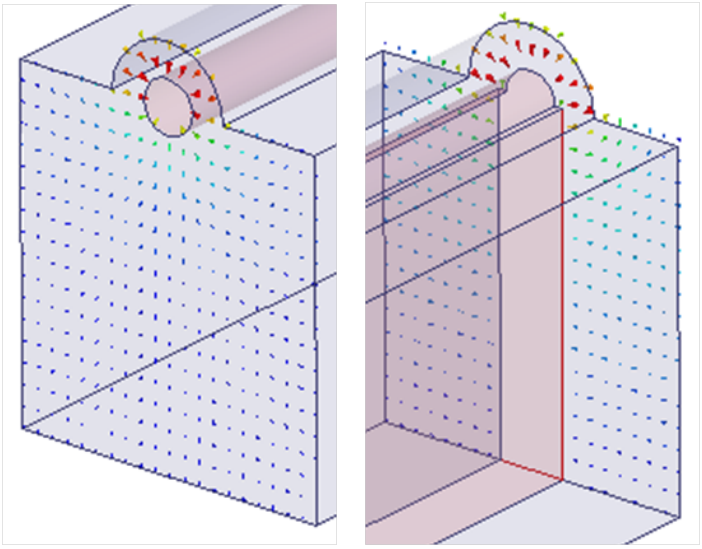

(a) TEM Mode (b) TE Mode

Figure 6.7: Electric field distribution in the TEM-to-TE mode conversion structure.

concentration while preventing coupling into higher-order modes. This has led to a TEM structure that is somewhat tall (to reduce bottom-wall coupling) and narrow (to prevent higher-order mode propagation). The mode field plots are shown in Fig. 6.7. The mode plots for the first odd mode and the first higher-order even mode at the input and output are shown in Fig. 6.8. Coupling into the input odd mode (Fig. 6.8(a)) is ideally zero due to the symmetry of the structure, but the actual amount of coupling is determined by fabrication errors. However, coupling into the input first higher-order even mode (Fig. 6.8(b)), produced by the transition from the input coaxial line, can be significant. This mode is suppressed by restricting the width of the conversion structure, causing the mode cutoff to move higher in frequency. The primary effect of coupling into this mode is an increase in reflection coefficient since the mode is poorly matched to the output even mode (Fig. 6.8(d)).

The TE side can be viewed as a continuation of the TEM side, except that the center conductor has been replaced with a ridge of essentially the same width as the center conductor diameter (Fig. 6.6). This single-ridged waveguide presents a largely continuous cross section to the high-concentrated field in the half-coax portion, while transforming to the necessary TE waveguide structure in the low-concentrated recta-coax portion. The reflection coefficient of the mode converter is shown in Fig. 6.9, where return loss

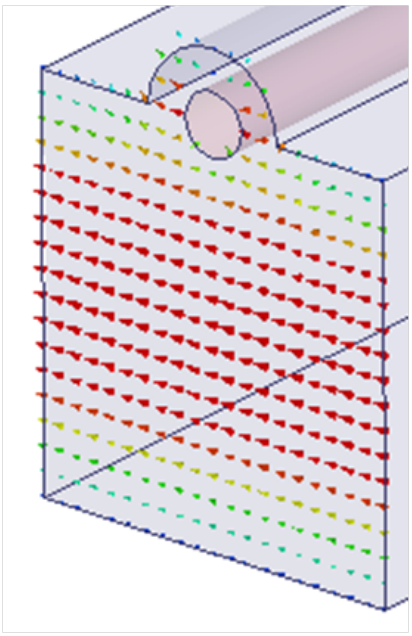

(a) First Odd Mode (Input)

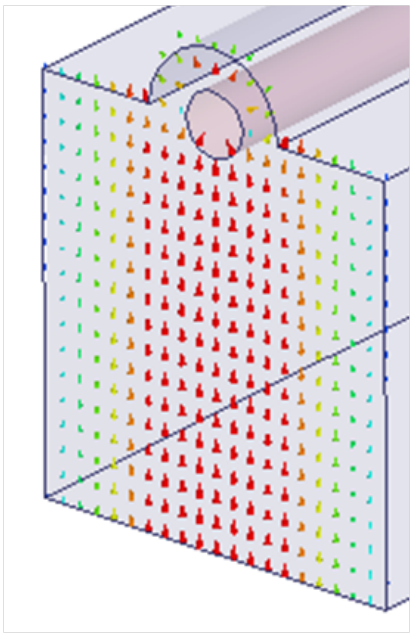

(b) First Higher-Order Even Mode (Input)

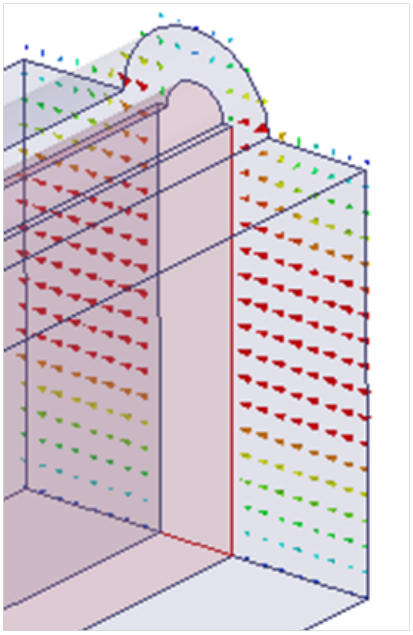

(c) First Odd Mode (Output)

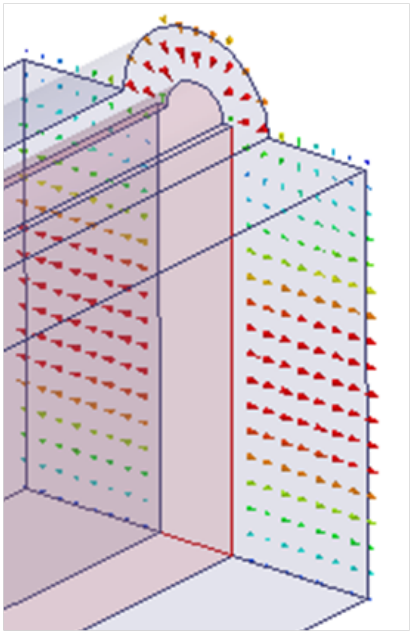

(d) First Higher-Order Even Mode (Output)

Figure 6.8: Higher-order modes in the mode conversion structure. The odd mode is ideally not excited due to the structure symmetry. The even mode is suppressed by keeping the width sufficiently narrow.

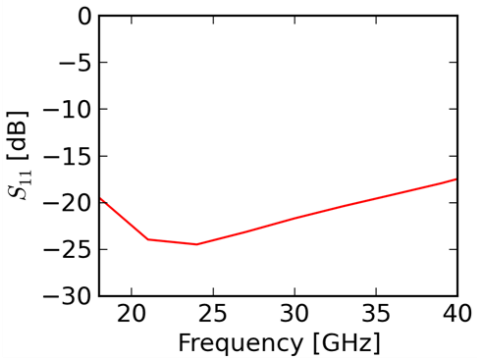

Figure 6.9: S_{11} of the mode converter shown in Fig. 6.6, which is below 15 dB throughout the 18-40 GHz band.

higher than 15 dB across the band is achieved.

The transitions into and out of the mode converter are realized as simple linear tapers (Fig. 6.10(a), with a smooth blending from air-loaded coaxial line to the mode converter body and out to WRD180C24. The entire structure is 2.54 cm in length.

6.4 Fabrication

Most PCB manufacturers have the capability to bond multiple thin layers together to create a monolithic multi-layered structure, a capability that is highly desirable for mechanical robustness. However, the PCB process is not capable of producing a monolithic structure of the 5.08 cm overall thickness needed by the fully assembled antenna. Instead, a bolt-through technique is adopted, where individual PCB layers are held together with long bolts that pass entirely through the structure. Tightening down the bolts provides positive electrical contact among layers without the need for interlayer bonding. The antenna design under consideration is sufficiently short in length that hardware capable of fastening the entire structure together is readily available.

6.4.1 Assembly

Fabrication of the complete antenna involves assembly of the WRD180C24-to-quad ridge aperture first, and then assembly of the coax-to-WRD180C24 transition. These two subassemblies are tested individually before being integrated into a fully-functional unit.

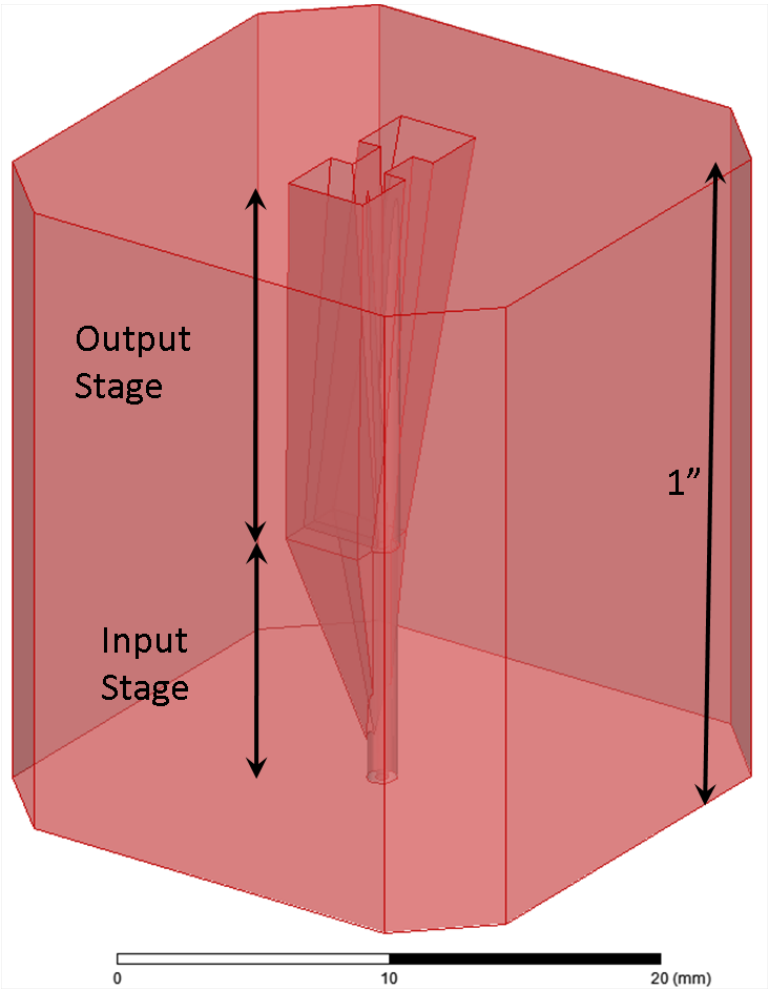

(a) Mode converter with input and output transitions

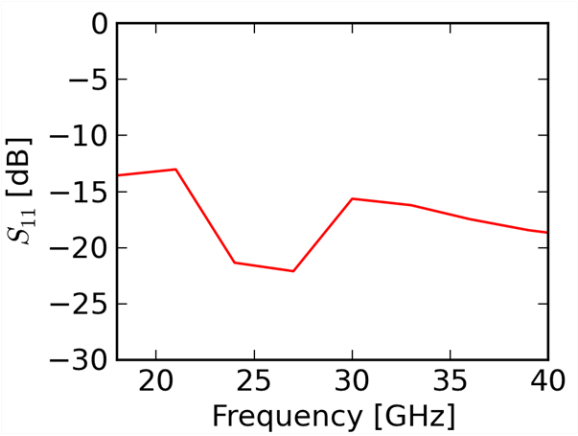

(b) S_{11} of the entire mode converter

Figure 6.10: Completed modeformer (a) structure and (b) performance, including coax and waveguide transitions.

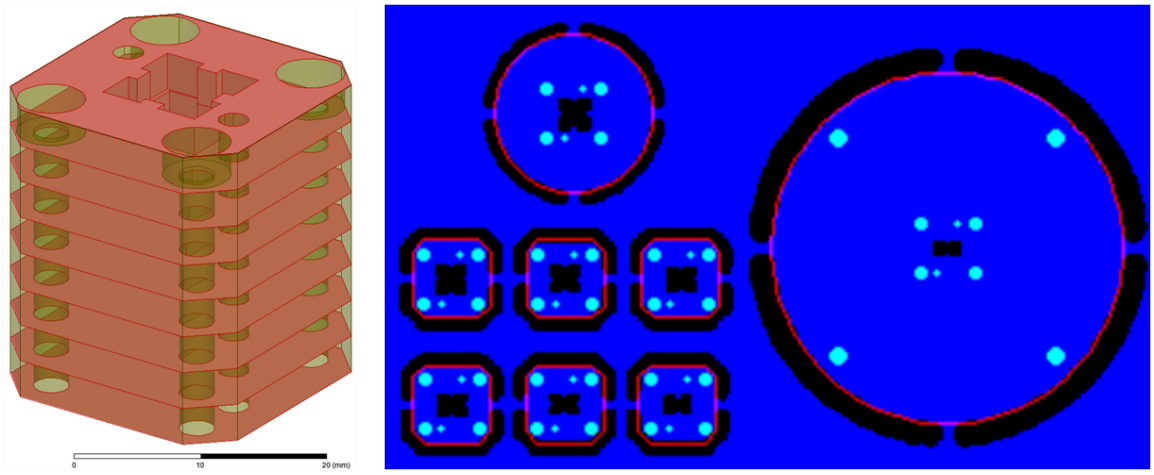

(a) (b)

Figure 6.11: (a) Double-ridged waveguide to quad-ridged aperture subassembly, showing the layer positioning and (b) PCB layout with the eight individual antenna sections. In the upper left is the top layer containing the radiating aperture and platform phantom (for testing purposes). In the lower left are six horn layer shims, and on the right is the fixturing plate and first horn layer combination.

6.4.1.1 Double-ridged Waveguide to Quad-ridged Aperture

For PCB fabrication purposes the stepped transition shown in Fig. 6.4 is broken down into eight 3.175 mm layers. The outline of the device is chosen to coincide with the outline of a standard 180C24 waveguide flange, so that testing of the subassembly can be performed apart from the coax-to-WRD180C24 transition. Fig. 6.11(a) shows the outline of the subassembly and the positioning of the individual PCB layers. Figure 6.11(b) shows the layout of parts on the PCB panel.

Eight total layers are needed for the structure, where the top layer provides a phantom for the antennas platform outline, while the bottom layer provides a secure base for interfacing with the antenna measurement fixture. Figure 6.12 shows the antenna (with measurement fixturing) prior to assembly. The assembled subassembly is shown in Fig. 6.13(a) along with measurement fixturing. A close-up view of the aperture is provided in Fig. 6.13(b), where the screw heads and registration pin holes have been covered with copper tape to ensure that the fabricated and modeled antennas are as similar as possible. For subassembly testing the antenna is fed by a commercial off-the-shelf (COTS) coax-to-double ridge waveguide (2.92mm-to-WRD180C24) transition. The layers are set up so that long registration dowel pins can be used with the coax-to-waveguide transition to provide precise alignment of all layers. The layers of the entire stackup are

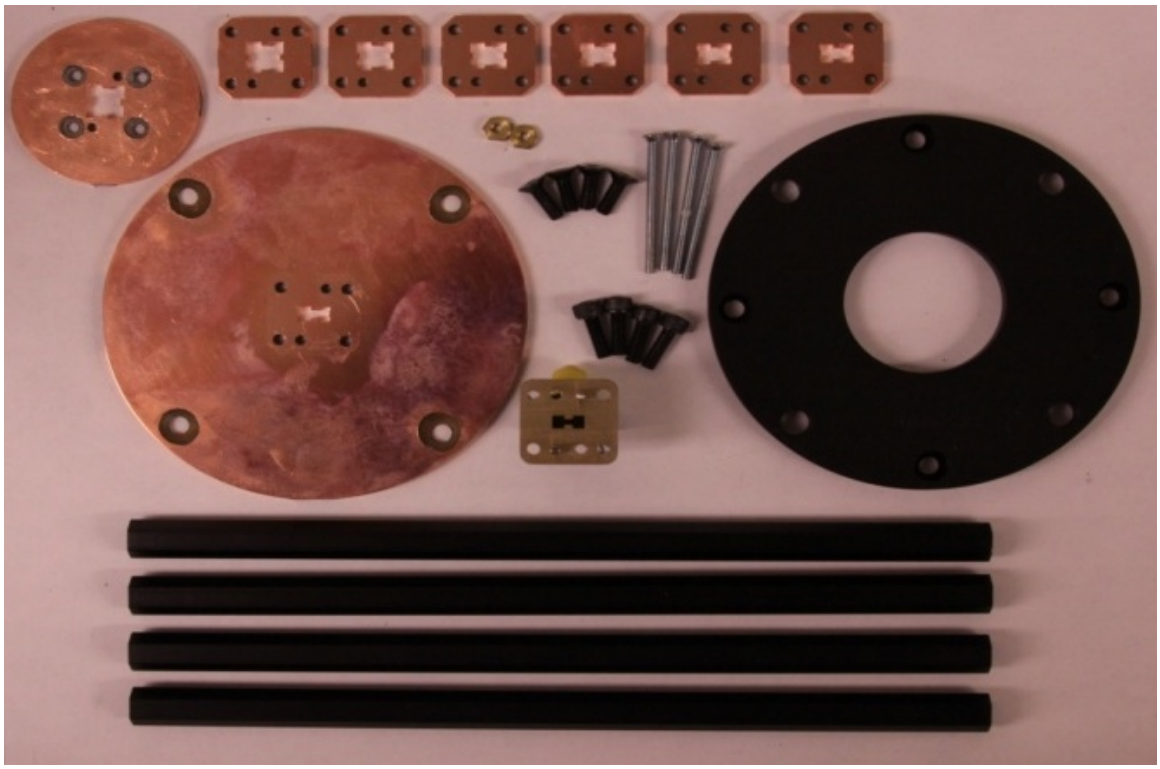

Figure 6.12: Double-ridged waveguide to quad-ridged aperture subassembly and measurement fixture prior to build. The positioner mounting plate and the positioner mounting standoffs are not part of the antenna, but are used for fixturing.

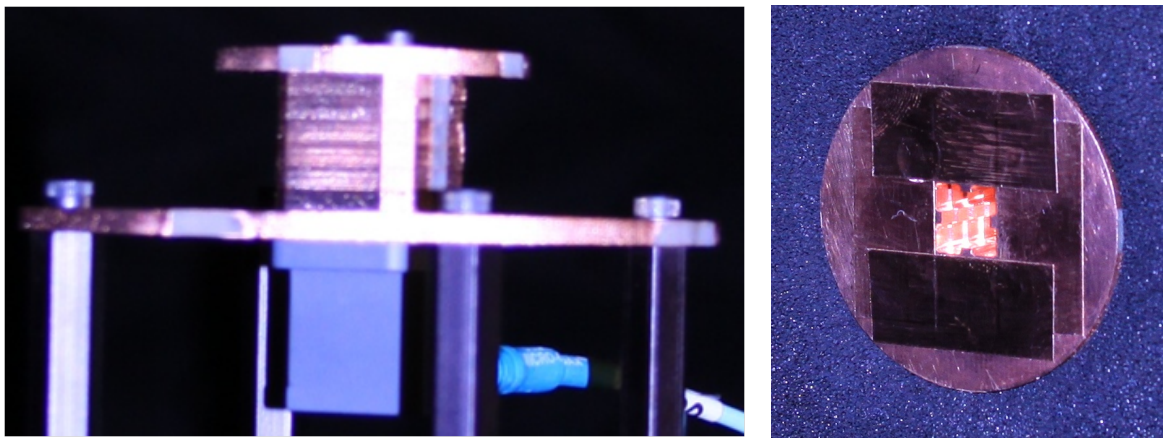

(a) Assembled antenna (b) Aperture with backing absorber

Figure 6.13: A close-up view of the fabricated antenna with absorber backing.

securely fastened together by 4-40 threaded screws, countersunk so the heads are flush-mounted. Finally, in order to keep the best possible agreement with the computational model, the screw heads are covered over with copper tape. The resulting antenna is structurally rigid, robust, and precisely aligned.

6.4.1.2 Coax-to-Double-ridged Waveguide Transition and Aperture Integration

The assembly of the 2.92 mm-to-WRD180C24 transition and its integration with the radiating aperture is straightforward. Fig. 6.14(a) shows the Southwest Microwave Model 1012-05SF 2.92 mm bulkhead connector fitted with the center conductor. The first four layers are then stacked and bolted securely to the bulkhead connector (Fig. 6.14(b)) allowing the center conductor to pass through, forming the initial part of the TEM input line. The remaining layers of the TEM line are added and secured by 4-40 thread machine screws and aluminum standoffs (Fig. 6.14(c)). The ridge of the first waveguide section is soldered to the center pin of the TEM line (Fig. 6.14(d)). Finally, the remaining layers are stacked up, along with the layers of the radiating aperture, and bolted together to form the completed antenna (Figs. 6.14(e) and 6.14(f)).

6.5 Measurement

In order to accurately measure the far-field performance of the antenna, scattering from the antenna support structure (fixturing) should be kept to a minimum. Figure 6.13(b) shows the fixtured antenna, where 2.54 cm thick urethane foam absorber was securely sandwiched between the antenna and the fixturing structure to simulate a free-space environment. The antenna was then measured using the spherical near-field technique in the antenna measurement facility at the University of Colorado. The measurement setup is shown in Fig. 6.15, where WR-42 and WR-28 open-ended waveguide probes were used as sources over their respective bandwidths. Using this setup, the agreement achieved between measured and simulated principal-plane (Fig. 6.16) and intercardinal-plane (Fig. 6.17) radiation patterns is excellent in the upper half-space. Since the absorber largely prevents radiation in the lower half-space, the agreement there is not expected to be accurate. While in theory the principal-plane cross-polarization discriminations (XPD) are zero, due to fabrication error the XPD reaches -25 dB at some frequencies, but the cross-polarized gain

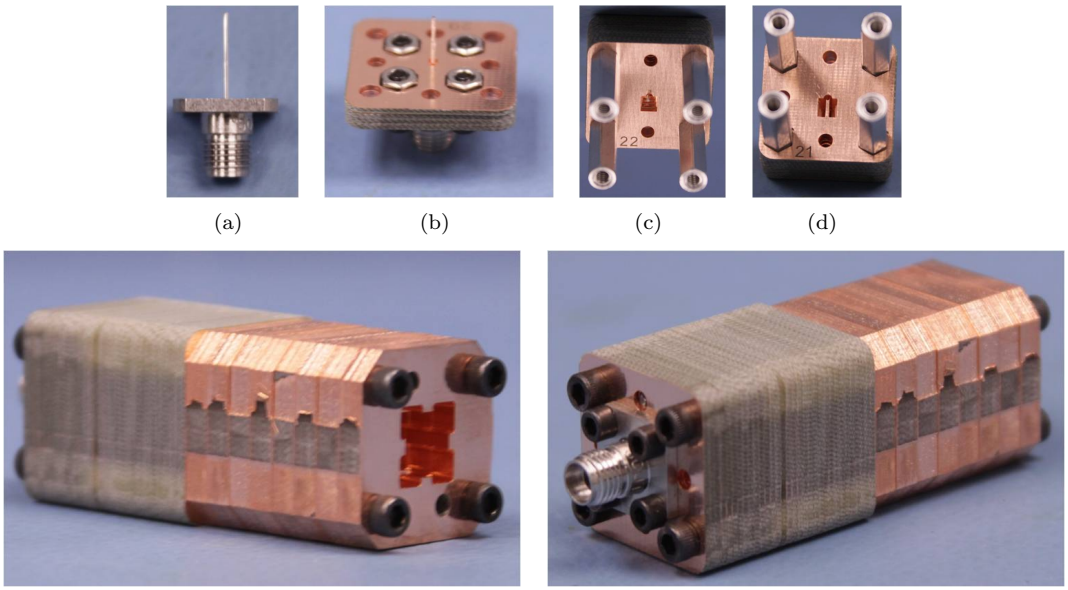

(a) (b) (c) (d)

(e) (f)

Figure 6.14: Assembly of the antenna with end launch. (a) Probe. (b) First four layers secured by machine screws. (c) TEM line secured by machine screws and hex standoffs. (d) First layer of waveguide section soldered to center pin. (e) Assembled antenna, aperture view. (f) Assembled antenna, connector view.

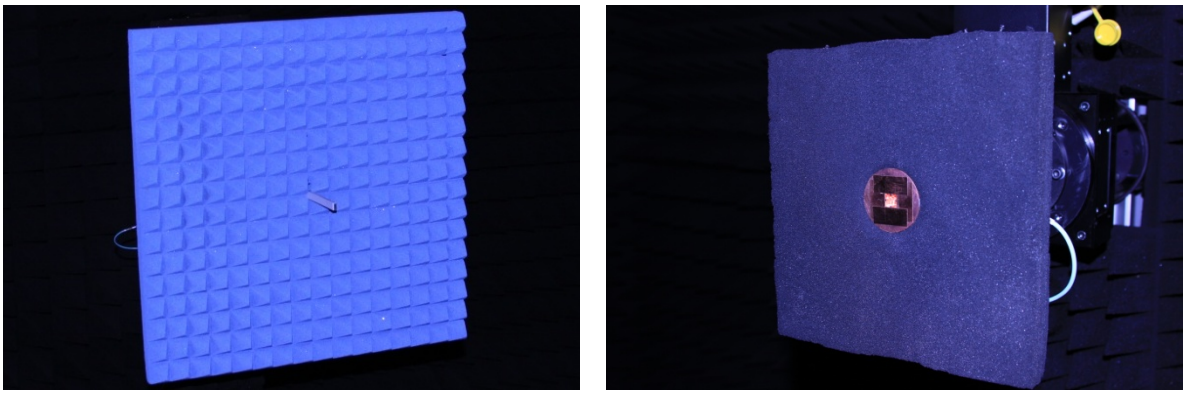

(a) Probe (b) AUT

Figure 6.15: Antenna measurement setup.

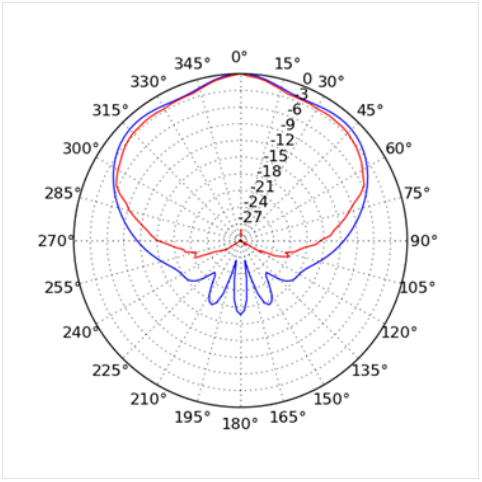

(a) 18 GHz E-plane

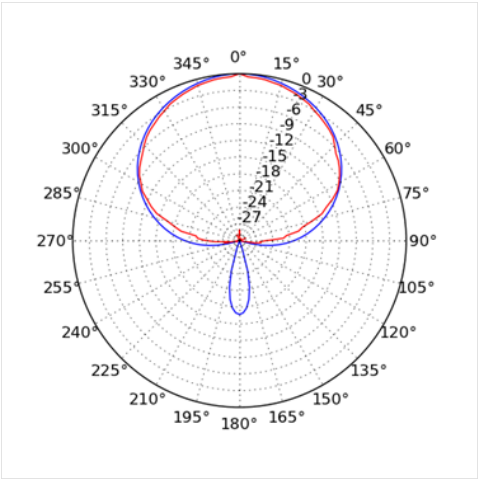

(b) 18 GHz H-plane

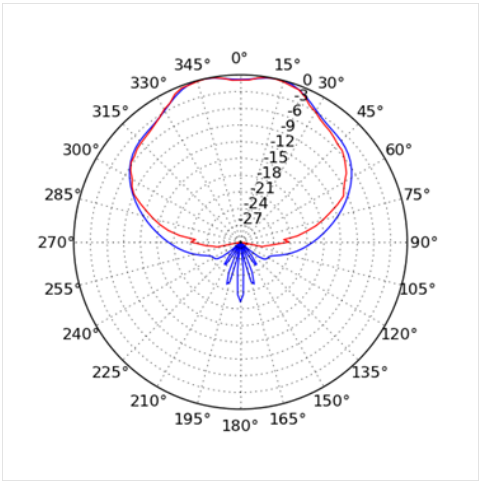

(c) 26 GHz E-plane

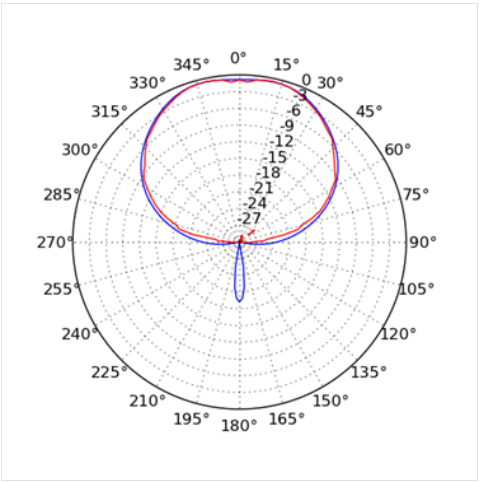

(d) 26 GHz H-plane

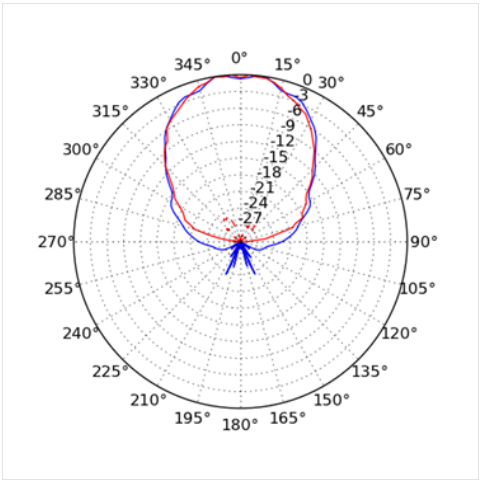

(e) 40 GHz E-plane

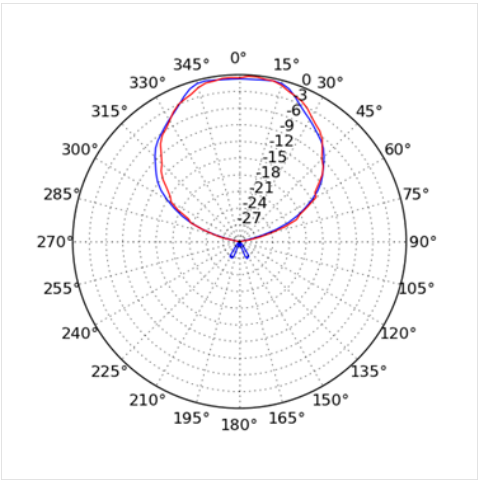

(f) 40 GHz H-plane

Figure 6.16: Simulated (blue) and measured (red) low-, mid-, and high-frequency E- and H-plane patterns for the antenna in Fig. 6.15(b)

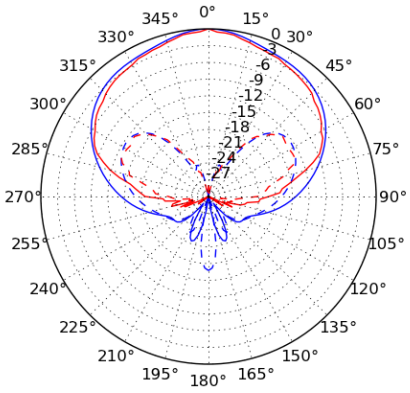

(a) 18 GHz E-plane

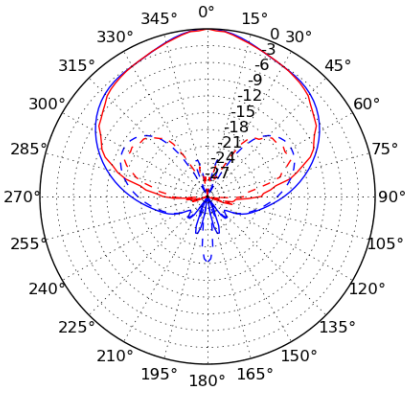

(b) 18 GHz H-plane

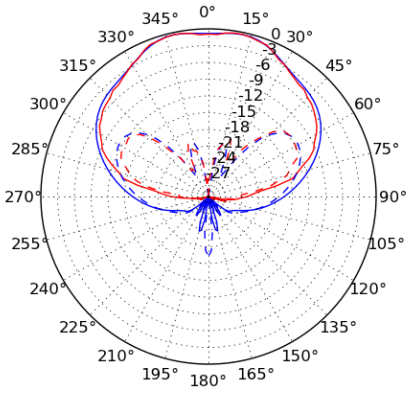

(c) 26 GHz E-plane

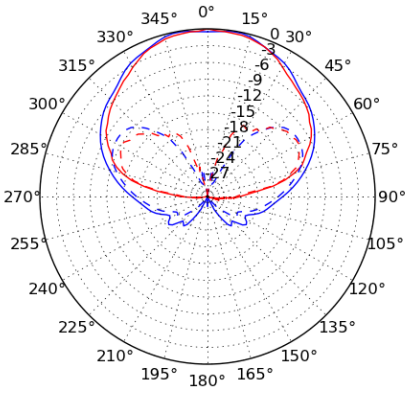

(d) 26 GHz H-plane

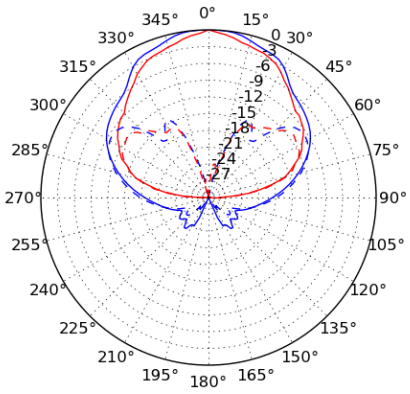

(e) 40 GHz E-plane

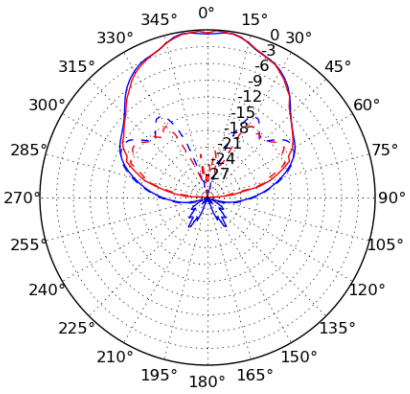

(f) 40 GHz H-plane

Figure 6.17: Simulated (blue) and measured (red) low-, mid-, and high-frequency intercardinal plane patterns for the antenna in Fig. 6.15(b)

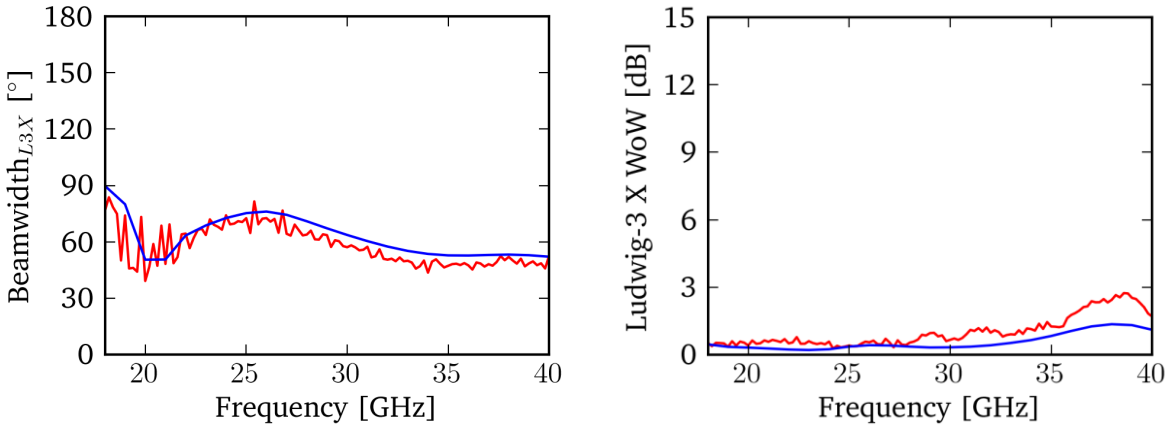

(a) HPBW (b) WoW

Figure 6.18: Measured vs. HFSS-simulated beamwidth and azimuthal beam uniformity

is generally 30 dB or greater below the beam maximum. However, this level of principal-plane XPD is acceptable for the envisioned application. Figures 6.18(a) and 6.18(b) respectively show the measured and simulated half-power beamwidth and WoW of the antenna, where good agreement is observed in both cases. Figure 6.19(a) shows the measured VSWR of the antenna measured at the double-ridged waveguide input, where some over-cutting of the inside corners of the waveguide sections has resulted in higher-than-expected VSWR value. Despite this, the VSWR performance of less than 2:1 is still an acceptable level. Adding the 2.92 mm-to-WRD180C24 transition results in the VSWR shown in Fig. 6.19(b), where the discrepancy between measurement and simulation is explained by the corner overcutting in the horn subassembly as well as non-idealities in the alignment and soldering of the center pin to the ridge waveguide.

6.6 Conclusions

This chapter discussed the design, fabrication, and measurement of a low-cost horn antenna based on the use of stacked PCB layers. A comprehensive examination of the relationship between the design objectives and the antenna characteristics was performed. It was found that, out of all other design objectives, the power handling objective affected the largest number of antenna characteristics. This analysis showed that a prudent design approach would be to use an antenna with inherently high power-handling capacity. The WRD180C24 double-ridged waveguide was found to provide ample power handling capacity as well as

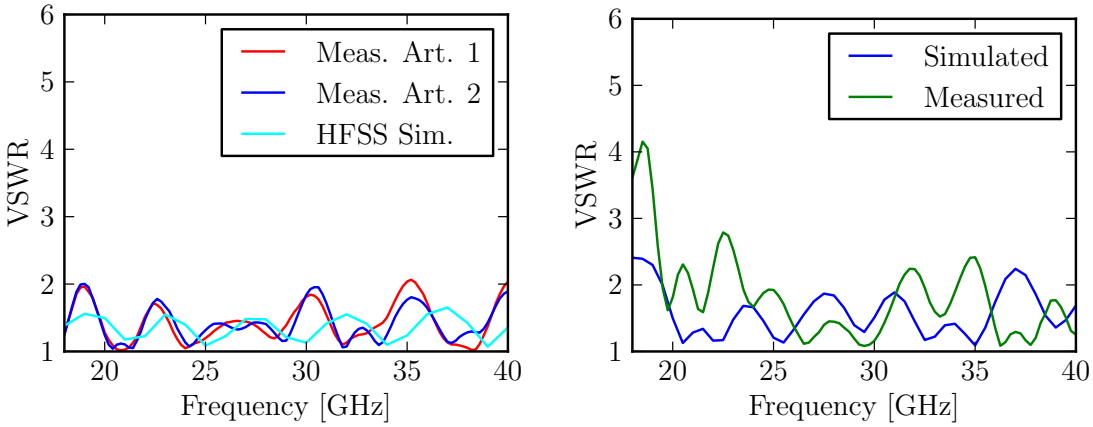

(a) Without end-launch

(b) With end-launch

Figure 6.19: (a) Measured (two articles) vs. simulated VSWR of the quad-ridged horn antenna without coaxial end-launch. The discrepancy between measurement and simulation is caused by overcutting of the corners by the circuit board manufacturer, causing the impedance to be higher than anticipated. (b) Measured vs. simulated VSWR of the entire antenna assembly.

adequate bandwidth. The desire for broad and equal beamwidth and dual-polarization capability led to the choice of a quad-ridged waveguide aperture as the radiating element. A coax-to-double-ridged waveguide end launch was designed for low- to medium-power testing. For prototyping purposes the entire antenna, including the coax-to-waveguide end launch, was fabricated using a novel low-cost technique based on stacked printed circuit board layers with plated slots. The performance of the antenna fabricated with this low-cost technique was found to be excellent, with principal-plane cross-polarization generally 30 dB or greater below the beam maximum. This indicates that the effect of layer registration error is acceptably small. Inter-cardinal plane co- and cross-polarized patterns match closely with simulations, indicating that the attainable precision of the fabrication technique is sufficient for many applications. The realized antenna has a stable beam pattern over an octave of bandwidth while maintaining good impedance match.

Chapter 7

Conclusions

7.1 Mode Theory of Spiral Antennas

Chapter 2 covered important theoretical background needed for understanding the research conducted herein. The active-region principle of operation of the spiral antenna was illustrated by evolving the spiral from a simple two-wire transmission line. The concepts of the truncation principle and cutoff frequency are also discussed. Spiral mode theory was introduced by examination of the solution of the infinite-armed spiral electromagnetic boundary-value problem. The usefulness of the mode theory is based on the fact that any arbitary excitation of a spiral can be decomposed into its constituent mode spectrum. The far field can likewise be decomposed into a mode spectrum that is related to the excitation spectrum. The multi-arm case was presented as a discrete version of the infinite-armed spiral. The role of multiarming in accomplishing mode filtering was explored and motivated by example. The use of the DFT for decomposing the excitations of a spiral into its constituent mode spectrum was used to implement a simple method for evaluating the errors in a modeforming network. Finally, impedance reduction of high arm-count multi-armed spirals by ring-feeding was noted, enabling practical implementation of high arm-count spiral antennas.

7.2 Pattern Purity of Coiled-Arm Spiral Antennas

Chapter 3 compared the performance of coiled-arm two- and four-armed spiral antennas. It was found that the four-armed spiral outperforms the two-armed spiral in nearly every respect when the spirals are operated near or below cutoff. In some instances the two-armed spiral was shown to have undesirable

characteristics that make it an unsuitable candidate for practical antenna applications. On the other hand, the four-armed spiral retains its far-field performance characteristics in a robust way, even down to frequencies far below cutoff.

Due to its flexibility and relatively low cost, arm coiling is an attractive miniaturization strategy for spiral antennas. However, it was shown that the use of arm coiling to improve low-frequency gain of the two-armed spiral produces mixed results when pattern purity effects are considered. While the low-frequency gain is improved, it occurs at the expense of other far-field parameters that are important in applications where spirals are frequently used, such as in radio direction finding and in radar warning receivers. In contrast, four-armed spiral antennas were shown to have a high degree of immunity from the contaminating effects of the miniaturization treatment. For many applications the performance improvement afforded by the four-armed spiral justifies the additional cost and complexity of the beam-forming network.

7.3 Four-Armed UHF- to S-band Spiral-Helix Antenna

The antenna presented in Chapter 4 bridges the performance gap between the horn antenna traditionally used in EA applications, and the absorptive-backed spiral antenna. The fabricated antenna shows much-improved gain and power handling capacity compared to the absorptive-backed spiral, while having a very compact form factor compared to commercially-available antennas. Also, the antenna has a useful bandwidth that extends far below the cutoff frequency f_0 of the spiral, validating the resistive loading approach used in the design. The resistive loading is easily removable and reconfigurable, allowing varied approaches to thermal management. The resulting antenna provides a highly compact replacement to the traditional horn antenna while maintaining a high degree of beam quality.

7.4 Wideband Pattern Nulling Using Multi-Armed Spiral Antennas

In Chapter 5 a simple method of achieving arbitrary null placement using a single multi-armed spiral aperture is discussed. The method uses an N-armed spiral to achieve simultaneous nulling of $N-2$ interferers, provided that all $N-1$ fundamental phase modes are radiated efficiently. Since the spiral aperture must be $m\lambda/\pi$ in diameter to radiate the mth phase mode efficiently, the maximum number of nulls that can

be practically formed is less than or equal to approximately $\pi D/\lambda - 1$. Null formation using phase modes is demonstrated computationally for an eight-armed spiral using **FEKO** and through ideal beam-formed measurements of three- and four-armed spiral antennas. Furthermore, it is shown that constant null position versus frequency is achieved when the mode weights are adjusted accordingly. Delay-line compensation has been shown to provide a practical means of achieving this weight adjustment over modest bandwidths.

7.5 A Low-Cost, 18-40 GHz Antenna with a Consistent Radiation Pattern

Chapter 6 discussed the design, fabrication, and measurement of a low-cost horn antenna based on the use of stacked PCB layers. A comprehensive examination of the relationship between the design objectives and the antenna characteristics was performed. It was found that, out of all other design objectives, the power handling objective affected the largest number of antenna characteristics. This analysis showed that a prudent design approach would be to use an antenna with inherently high power-handling capacity. The WRD180C24 double-ridged waveguide was found to provide ample power handling capacity as well as adequate bandwidth. The desire for broad and equal beamwidth and dual-polarization capability led to the choice of a quad-ridged waveguide aperture as the radiating element. A coax-to-double-ridged waveguide end launch was designed for low- to medium-power testing. For prototyping purposes the entire antenna, including the coax-to-waveguide end launch, was fabricated using a novel low-cost technique based on stacked printed circuit board layers with plated slots. The performance of the antenna fabricated with this low-cost technique was found to be excellent, with principal-plane cross-polarization generally 30 dB or greater below the beam maximum. This indicates that the effect of layer registration error is acceptably small. Inter-cardinal plane co- and cross-polarized patterns match closely with simulations, indicating that the attainable precision of the fabrication technique is sufficient for many applications. The realized antenna has a stable beam pattern over an octave of bandwidth while maintaining good impedance match.

7.6 Original Contributions

The original contributions of this thesis are as follows:

- Demonstrated that the mode-filtering property of multi-armed spiral antennas can be successfully applied to the design of spiral antennas with high far-field quality.

- Demonstrated a clear path for wideband spiral antenna implementation in high-power transmitting applications. This is done by careful selection of the feed structure, radiating element, and arm termination.

- Implemented multi-arming as a way to reduce pattern contamination on coiled-arm antennas. Also used the technique to realize an antenna with excellent pattern symmetry, even at frequencies deep below the cutoff frequency.

- Developed and successfully applied a dual-layering approach to reduce modal impedance. Whereas other other impedance-reduction techniques typically reduce the peak power handling, this technique is expected to actually improve both peak and average power handling by retaining a self-complementary spiral structure.

- Developed a spiral-helix termination with simple and flexible thermal management. Use of commercially-available coaxial loads allows the use of a pre-engineered thermal management solution. Alternatively, the lost power can be routed to a more convenient location by connecting coaxial cables in place of the loads and routing the cables to a location where thermal management or RF power reclamation can be implemented.

- Formulated a new algorithm for pattern nulling by modal superposition. Since the phase centers of each of the modes are co-located, grating-lobe-free bandwidth is unlimited in principle. Null rotation can be compensated in various ways depending on system requirements, and can be as simple as adding delay lines and phase shifters to a mode-forming network.

- Recognized the benefit of the ring-topology feed for spirals with more than 6 arms. The ring-type feed topology reduces the modal impedances of Mode 1-excited antennas with high arm counts to enable practical impedance transformations.

- Demonstrated a fabrication technique based on commodity printed circuit board technology for low-cost millimeter-wave horn antenna prototyping. This technique can be used to realize a huge cost reduction compared to conventional machining for suitable horn antenna designs.

7.7 Future Work

The work performed in this thesis could be expanded in the following interesting areas.

7.7.1 Exploitation of N-fold Rotational Symmetry in EM Simulation

Current-generation commercial electromagnetic simulation codes, whether based on the Method of Moments or the Finite Element Method, appear to be generally incapable of exploiting the inherent N-fold rotational geometric and excitational symmetry of N-armed modally-excited spiral antennas.

In a modally-excited N-armed spiral (the most common excitation case), the currents and charges for any given spiral arm are related to those of any other arm by a known rotation and phase shift. Exploitation of this symmetry could result in an N-fold reduction in unknowns, resulting in much-improved computational efficiency. The case of asymmetric excitation could be handled straightforwardly by modal decomposition and superposition, where at most N separate problems would need to be considered (one for each mode). The worst case would be where all N possible modes (including the unbalanced mode) would need to be solved, requiring N separate solutions but with N-fold fewer unknowns.

This symmetry exploitation would seem to be nearly as straightforward to implement as the currently-implemented E- and H-plane symmetry planes in commercial EM simulation packages. This omission in the commercial codes seems to be more related to the specialized use-case than to any inherent numerical difficulty. The current lack of this exploitation capability is a significant detriment to the future development of spiral antennas with high arm counts.

7.7.2 Wideband Pattern Nulling

The research in Chapter 5 proved the principle of wideband pattern nulling, but the technique remains untested using hardware that implements the necessary functionality. Implementation of the complete nulling

system either through a direct digital interface or through an RF hybrid beamforming network would be a significant contribution.

Cosite Mitigation: Both mobile and fixed-site communication platforms can have a number of antennas located in a small area. Cosite interference on these platforms is a major concern, and can be the subject of expensive integration studies. Demonstration of a nulling system's capability to reduce antenna-to-antenna coupling in crowded antenna installations, such as encountered in mobile communication, is an application area that also has yet to be explored.

7.7.3 PCB Stacking Technique

Efficiency: While the patterns and VSWR performance of the stacked-PCB antennas are very promising, one area that has yet to be tested is the RF efficiency of the technique. Factors that can affect the efficiency are:

- Additional path length resulting from the stepped approximation of smooth antenna structures.
- Surface roughness of the plated slots. The slots are mechanically machined, and some tooling roughness has been observed on some surfaces of the plated slots. This has been most observable where large tool diameters have been used at high speed.
- Inter-layer surface-mating quality. Poor mating quality could result from planarity imperfections in the PCB material or due to assembly compression stress, roughness and oxidation of the mating surfaces.

The question of whether low-cost commodity manufacturing techniques are capable of achieving the necessary quality standards is vitally important to the practicality of the technique.

PCB Panel Arrays: The PCB stacking technique has been used in this thesis to realize a single horn antenna element; however, the technique could potentially also used to fabricate large antenna arrays. A critical question would be whether this would represent a significant cost reduction compared to traditional fabrication techniques.

Lateral Propagation: The PCB stacking technique is used in this thesis to enable wideband inter-layer propagation. However, while the author's colleagues have pursued lateral propagation in recta-coax waveguide, lateral propagation in ridged waveguide using the stacked PCB technique has not been attempted at this time.

7.7.4 Spiral Antenna Power Handling

The spiral-helix antenna presented in Chapter 4 of this thesis was designed with high power-handling capacity in mind; however, due to cost considerations the fabricated antenna used some materials suspected to have rather low power-handling characteristics, and the fabricated antenna was only subjected to low-power testing. A redesign using more suitable materials and subjected to high RF power-handling measurements would validate the design approach taken.

7.7.5 Spiral Antenna Phase Center

For phase center computation this thesis only examined the uniform pattern weighting function over a restricted field of view; however, other pattern weighting functions are possible. Determining a weighting function that maximized a certain performance parameter would be a worthwhile contribution; for instance, maximizing gain for a parabolic reflector or lens.

Dielectric lenses can be used to improve the gain of a spiral antenna by placing the spiral phase center at the focus of the lens. However, it is known that the presence of the dielectric affects the position of the phase center. A careful quantitative study of this effect on the spiral antenna phase center would be a valuable addition to the body of knowledge.

This thesis has shown that the location of the phase center of a spiral antenna can be made to be frequency-stable in terms of the electrical distance kd. However, the physical location varies by some amount. Reflector and lens antennas can have a more stable beamwidth when the feed phase center is essentially a fixed constant. Therefore determination of the shape of the spiral antenna aperture so as to accomplish a physically-fixed phase center would be of some value.

Bibliography

[1] Micro-Coax, Inc. (2011, July) Semi-rigid coaxial cable product selector. [Online]. Available: http://www.micro-coax.com/pages/products/ProductTypes/CableTypes/Semi-RigidCoaxial/EqualTo50ohms/Size/Between085and141inches.asp

[2] I. Advanced Technical Materials. (2011, July) Raw waveguide information. [Online]. Available: http://www.atmmicrowave.com/wave-RawWG.html

[3] R.-S. Cheo, V. H. Rumsey, and J. W. Welch, "A solution to the frequency-independent antenna problem," IRE Trans. Antennas Propag., vol. 9, pp. 527–534, November 1961.

[4] P. Kasemir, N. Sutton, M. Radway, B. Jeong, T. Brown, and D. Filipović, "Wideband analog and digital beamforming," in TELSIKS 2009, October 2009, pp. 372–375.

[5] J. S. Chatterjee, "Radiation field of a conical helix," Journal of Applied Physics, vol. 24, no. 5, pp. 550–559, May 1953.

[6] E. M. Turner, "Spiral slot antenna," U.S. Patent 2,863,145, 1958.

[7] J. D. Dyson, "The non-planar equiangular spiral antenna," in Proc. USAF Antenna Research and Development Program Symp., 1958.

[8] ——, "The equiangular spiral antenna," IRE Trans. Antennas Propag., vol. AP-7, pp. 181–187, April 1959.

[9] J. Jones, P. Taylor, and C. Morrow, "Design techniques for a light weight high power spiral antenna," in WESCON/60 Conf. Record, August 1960, pp. 107–122.

[10] W. R. Free, F. L. Cain, C. E. Ryan, C. P. Burns, and E. M. Turner, "High-power constant-index lens antennas," vol. 22, pp. 582–584, 1974.

[11] J. A. Kaiser, "Dual operation with the two-wire spiral antenna," vol. 9, no. 6, pp. 583–584, November 1961.

[12] R. G. Corzine and J. A. Mosko, Four-Arm Spiral Antennas. Norwood, MA: Artech House, 1990.

[13] P. A. Lantz, "A two-channel monopulse reflector antenna system with a multimode logarithmic spiral feed," in Sixteenth Annual Symposium on USAF Antenna Research and Development Progress, 1966.

[14] P. A. Lantz and G. G. Chadwick, "A 17:1 dual-band circularly polarized two-channel monopulse tracking system," in Proc. USAF Antenna Research and Development Program Symp., 1969.

[15] B. H. Burdine, "Radiation from the double-spiral antenna," in Proc. USAF Antenna Research and Development Program, 1955.

[16] V. H. Rumsey, "Frequency independent antennas," IRE National Convention Record, vol. 1, pp. 114–118, 1957.

[17] ——, "A solution to the equiangular spiral antenna problem," vol. 7, no. 5, pp. 117–117, 1959.

[18] B. Cheo and V. Rumsey, "A solution to the equiangular spiral antenna problem - continued," in IEEE Antennas and Propagation Society International Symposium, 1966, December 1966, pp. 126–130.

[19] V. H. Rumsey, "A new way of solving maxwell's equations," vol. 9, no. 5, pp. 461–465, September 1961.

[20] G. A. Deschamps, "Impedance properties of complementary multiterminal planar structures," IRE Trans. Antennas Propag., vol. 7, no. 5, pp. 371–378, December 1959.

[21] H. G. Booker, "Slot aerials and their relation to complementary wire aerials (babinet's principle)," Journal of the Institution of Electrical Engineers – Part IIIA: Radiolocation, vol. 93, no. 4, pp. 620–626, January 1946.

[22] R. Sivan-Sussman, "Various modes of the equiangular spiral antenna," vol. 11, pp. 533–539, Sep 1963.

[23] C. Liang and Y. Lo, "A multipole-field study for the multiarm log-spiral antennas," vol. 16, no. 6, pp. 656–664, November 1968.

[24] Office of Naval Research. (2007, September) ONR BAA announcement # ONR 07-009. [Online]. Available: http://www.onr.navy.mil/ /media/Files/Funding-Announcements/BAA/07-009.ashx

[25] FEKO: EM Software and Systems [Online]. Available: http://www.feko.info.

[26] HFSS: High Frequency Structure Simulator Ansoft Corporation [Online]. Available: http://www.hfss.com.

[27] V. H. Rumsey, Frequency Independent Antennas. New York: Academic Press, 1966.

[28] T. P. Cencich and J. A. Huffman, "The analysis of wideband spiral antennas using modal decomposition," vol. 46, no. 4, pp. 20–26, August 2004.

[29] D. S. Filipović and T. P. Cencich, Antenna engineering handbook, 4th ed. McGraw-Hill, 2007, ch. Frequency Independent Antennas, pp. 13–1ff.

[30] M. J. Radway, T. P. Cencich, and D. S. Filipović, "Pattern purity of coiled-arm spiral antennas," vol. 59, no. 3, pp. 758–766, March 2011.

[31] L. Josefsson and P. Persson, Conformal Array Antenna Theory and Design. Hoboken, New Jersey: John Wiley and Sons, Inc., 2006.

[32] T. Milligan, "Parameters of a multiple-arm spiral antenna from single-arm measurements," vol. 40, no. 6, pp. 65–69, December 1998.

[33] Y. Mushiake, Self-Complementary Antennas. Springer-Verlag, 1996.

[34] B. A. Kramer, M. Lee, C.-C. Chen, and J. L. Volakis, "Design and performance of an ultrawide-band ceramic-loaded slot spiral," vol. 53, pp. 2193–2199, July 2005.

[35] B. A. Kramer, S. Koulouridis, C.-C. Chen, and J. L. Volakis, "A novel reflective surface for an UHF spiral antenna," vol. 5, pp. 32–34, December 2006.

[36] J. L. Volakis, G. Mumcu, K. Sertel, C.-C. Chen, M. Lee, B. Kramer, D. Psychoudakis, and G. Kisiltas, "Antenna miniaturization using magnetic-photonic and degenerate band-edge crystals," vol. 48, no. 5, pp. 12–28, October 2006.

[37] H. Nakano and J. Yamauchi, "Sunflower spiral antenna," in Proc. 1980 IEEE Antennas Propagat. Soc. Int. Symp., June 1980, pp. 709–712.

[38] D. S. Filipović and J. L. Volakis, "Broadband meanderline slot spiral antenna," IEE Proc. - Microw. Antennas Propag., vol. 149, no. 2, pp. 98–105, April 2002.

[39] ——, "A flush-mounted multifunctional slot aperture (combo-antenna) for automotive applications," vol. 52, pp. 563–571, February 2004.

[40] D. S. Filipović, A. U. Bhobe, and T. P. Cencich, "Low-profile broadband dual-mode four-arm slot spiral antenna with dual dyson balun feed," IEE Proc. - Microw. Antennas Propag., vol. 152, no. 6, pp. 527–533, December 2005.

[41] M. Lee, B. A. Kramer, C.-C. Chen, and J. L. Volakis, "Distributed lumped loads and lossy transmission line model for wideband spiral antenna miniaturization and characterization," vol. 55, pp. 2671–2678, October 2007.

[42] D. S. Filipovic, M. Nurnberger, and J. L. Volakis, "Ultra wideband slot spiral with dielectric loading: measurements and simulations," in Proc. 2000 IEEE Antennas Propag. Soc. Int. Symp., July 2000, pp. 1536–1539.

[43] B. A. Kramer, S. Koulouridis, C.-C. Chen, and J. L. Volakis, "Miniature UWB conformal aperture with volumetric inductive loading," in Proc. 2006 IEEE Antennas Propag. Soc. Int. Symp., July 2006, pp. 3693–3696.

[44] B. A. Kramer, C.-C. Chen, and J. L. Volakis, "Size reduction of a low-profile spiral antenna using inductive and dielectric loading," vol. 7, pp. 22–25, 2008.

[45] EMSS, FEKO 5.5 User Manual. Stellenbosch, S.A.: EM Software and Systems, 2009.

[46] H. Nakano, "A meander spiral antenna," in Proc. 2004 IEEE Antennas Propag. Soc. Int. Symp., vol. 3, June 2004, pp. 2243–2246.

[47] H. Nakano, K. Nogami, S. Arai, H. Mimaki, and J. Yamauchi, "A spiral antenna backed by a conducting plane reflector," vol. 34, no. 6, pp. 791–796, June 1986.

[48] R. T. Gloutak and N. G. Alexopoulous, "Two-arm eccentric spiral antenna," vol. 45, no. 4, pp. 723–730, April 1997.

[49] S. E. Lipsky, Microwave Passive Direction Finding. Raleigh, NC: SciTech Publishing, 2004.

[50] H. Nakano, Helical and Spiral Antennas – A Numerical Approach. Research Studies Press, 1987.

[51] A. C. Goetz and T. L. Boolos, "Multiple arm spiral antenna system with multiple beamforming capability," U.S. Patent 5 327 143, July 5, 1994.

[52] K. O. Ezal, T. L. Larry, A. S. Richen, M. R. Wiatt, C. S. Agate, B. D. Werner, and M. L. Vanblaricum, "Compact antenna system for polarization sensitive null steering and direction finding," U.S. Patent US 7 577 464 B2, August 18, 2009.

[53] C. Waldschmidt and W. Wiesbeck, "Compact wide-band multimode antennas for MIMO and diversity," vol. 52, no. 8, pp. 1963–1969, August 2004.

[54] M. J. Radway, T. P. Cencich, and D. S. Filipović, "Phase center stability of planar spiral antennas," in Proc. 2009 Antenna Applications Symp., 2009.

[55] D. Deslandes and K. Wu, "Design consideration and performance analysis of substrate integrated waveguide components," in Proceedings of the 32nd European Microwave Conference, September 2002, pp. 1–4.

[56] Southwest Microwave, Inc. (2011, July) 2.92 mm "JK" connector series. [Online]. Available: http://mpd.southwestmicrowave.com/pdf/series_292mm.pdf

[57] Y. Rong and K. A. Zaki, "Characteristics of generalized rectangular and circular ridge waveguides," vol. 48, no. 2, pp. 258–265, February 2000.

[58] C. A. Balanis, Antenna Theory: Analysis and Design, 3rd ed. Hoboken, New Jersey: John Wiley and Sons, Inc., 2005.

[59] L. Lewin, Advanced Theory of Waveguides. Iliffe and Sons, Ltd., 1951.

[60] R. M. Fano, "Theoretical limitations on the broadband matching of arbitrary impedances," Journal of the Franklin Institute, vol. 249, no. 1, pp. 57–83, January 1950.

[61] Times Microwave Systems. (2011, July) A guide to the selection of RF coaxial cable. [Online]. Available: http://www.timesmicrowave.com/products/tl14/downloads/70.pdf

[62] ——. (2011, July) A guide to the selection of RF coaxial cable. [Online]. Available: http://www.timesmicrowave.com/products/tl14/downloads/71.pdf

[63] A. C. Ludwig, "The definition of cross-polarization," vol. 21, no. 1, pp. 116–119, January 1973.

[64] ANSYS Corporation. (2010, September) High frequency structure simulator. [Online]. Available: http://www.ansys.com

[65] P.-S. Kildal, "Combined e- and h- plane phase centers of antenna feeds," vol. 31, no. 1, pp. 199–202, January 1983.

[66] N. Barbano, "Phase center distributions of spiral antennas," in WESCON/60 Conference Record, vol. 4, August 1960, pp. 123–130.

[67] M. S. Wheeler, "Phase characteristics of spiral antennas for interferometer applications," in IRE International Convention Record, vol. 12, March 1964, pp. 143–152.

[68] J. D. Dyson, "The characteristics and design of the conical log-spiral antenna," vol. 13, no. 4, pp. 488–499, July 1965.

[69] A. Atia and K. K. Mei, "Analysis of multiple-arm conical log-spiral antennas," vol. 19, no. 3, pp. 320–331, May 1971.

[70] Y. Y. Hu, "A method of determining phase centers and its application to electromagnetic horns," Journal of the Franklin Institute, vol. 271, pp. 31–36, January 1961.

[71] G. Taubin, "Estimation of planar curves, surfaces and nonplanar space curves defined by implicit equations, with applications to edge and range image segmentation," vol. 13, pp. 1115–1138, 1991.

[72] W. V. T. Rusch and P. D. Potter, Analysis of reflector antennas. New York, New York: Academic Press, Inc., 1970.

[73] J. J. Lee, Antenna Engineering Handbook, 4th ed. McGraw-Hill, 2007, ch. Ultra Wideband Arrays.

[74] R. C. Hansen, Phased Array Antennas. Hoboken, New Jersey: John Wiley and Sons, Inc., 2009.

[75] L. R. Lewis, Practical Phased Array Antenna Systems. Artech House, 1991, ch. Phased Array Elements – Part 2.

[76] B. A. Munk, Finite Antenna Arrays and FSS. John Wiley and Sons, Inc., 2003.

[77] M. J. Radway, W. N. Kefauver, and D. S. Filipović, "On the use of spiral antennas for electronic attack," in Proc. of the Ant. Appl. Symp., 2008.

Appendix A

Phase Center Stability of Planar Spiral Antennas

A.1 Introduction

Soon after their introduction, planar spiral antennas were recognized for their usefulness as broadband feeds for prime-focus reflector antennas. Cheo, Rumsey, and Welch [3] theoretically analyzed the spiral and discovered that for small growth rates the constant phase surface is nearly spherical in shape, and therefore the concept of phase center is well-defined for the planar spiral. Lantz [13] noted that the spiral antenna's broad, symmetric pattern could produce relatively uniform illumination of the reflector surface and allow precisely controlled edge illumination over a broad bandwidth. He used a combination of two reflective-cavity backed four-armed spirals separately fed to obtain dual-mode monopulse operation at 136 MHz, 235 MHz, and 406 MHz simultaneously. Similarly, spiral antennas have been found to be useful as lens feeds [10].

A.2 Definition of Phase Center and Phase Center Variation (PCV)

The IEEE defines phase center as **the location of a point associated with an antenna such that, if it is taken as the center of a sphere whose radius extends into the far field, the phase of a given field component over the surface of the radiation sphere is essentially constant, at least over that portion of the surface where the radiation is significant**. Balanis [58] gives the following concise definition: **The reference point which makes** [the far-field phase] **independent of** [observation angle]... Yet another definition provided by Kildal [65] is simply **... the phase reference point which maximizes the feed efficiency ...**.

Each of these definitions has important deficiencies; for instance, Kildal's definition is specific to antennas used as reflector feeds, and is meaningless for antennas used in GPS systems, for example. Balanis' definition assumes the existence of a reference point that makes the far-field phase independent of observation angle; however, such a point does not strictly exist for physically realizable antennas. While for some antennas the error is very small (e.g. for electrically small dipoles in free space), there are many antennas for which this definition breaks down. The IEEE definition modifies this somewhat by allowing only a portion of the far field surface to be considered, yet ultimately suffers from the same deficiency as the Balanis definition.

The GPS literature deals with this reality by instead allowing the phase center to be a function of azimuth and elevation. Then a mean phase center is defined which is independent of azimuth and elevation, and a quantity called phase center variation (PCV) (a function of azimuth and elevation) is defined to describe the error committed by the assignment of the mean phase center. While this representation is formally correct, it seems abusive to use the term phase center in this way, since the IEEE defines phase center as a point in space.

For the purposes of this paper, we use an alternate definition of phase center that allows for a unique point to be determined. Referring to Fig. A.1(a), **given a general far-field phase function** (shown schematically by the ellipse f), **the phase center d_z is the center of the sphere** (shown schematically by the circle ξ) **that minimizes phase error magnitude $|f - \xi|$ in a suitable sense**. This definition accomplishes three objectives. First, it defines the phase center as a point in space that can be uniquely determined provided that a suitable fitting algorithm is used. Second, the phase center is explicitly defined to be in an approximate sense, so that even antennas with non-spherical phase surfaces can be assigned a unique phase center. Third, it is sufficiently general so as to be useful in diverse situations. Under this definition of phase center the phase error $f - \xi$ plays an important role. Another quantity frequently encountered in the GPS literature is the previously mentioned PCV, where we give the following interpretation: **The PCV Δr is the displacement about the phase center d_z in the direction θ, ϕ required to make the actual phase function f and the ideal phase function ξ coincident.** Figure A.1(b) demonstrates the

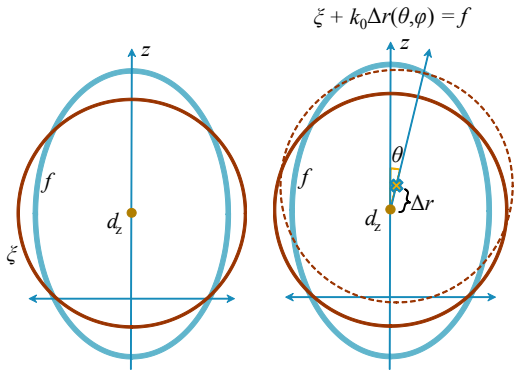

(a) Phase Center. (b) Phase Center Variation.

Figure A.1: Illustrations of the concepts of phase center and phase center variation (PCV)

definition in two dimensions, where it can be seen that an expression for PCV is

$$\Delta r = (f - \xi)/k_0 \tag{A.1}$$

where k_0 is the propagation constant of free space. That is, PCV only differs from the phase error by the multiplicative constant k_0.

A.3 Some Past Studies of Spiral Antenna Phase Center

Barbano [66] used a phaseless two-probe technique to measure the phase center of high growth rate spiral antennas at a single frequency. These measurements, taken in three different planes, were found to be in agreement with the theory of [3]. Wheeler [67] later used an assumed current distribution to calculate the phase center of wire spirals of infinite radius and infinitely small feed region. He found that for interferometer applications the growth rate of such antennas should be no greater than $a = 0.1$/rad to ensure that the phase error is sufficiently small. Dyson [68] measured apparent phase centers for two-armed conical log-spiral antennas by weighting the contribution to phase center more heavily for angles near broadside. Atia and Mei [69] use Hu's method [70] to determine the phase center of a numerically simulated four-armed conical spiral antenna using the slope of the far-field phase.

A.4 Phase Center Computation

A.4.1 Algorithm

The method most commonly used to determine the phase center of measured principal plane data is one given by Hu [70], in which the far-field phase is plotted and a straight-line fit is performed on the phase data. The slope of the fitted line is d_z/λ, where d_z is the phase center location. This method is straightforward and is especially useful when postprocessing range data manually. In practical cases the phase data will not be perfectly linear, which may be either due to measurement noise or due to inherent phase front nonuniformity. In such case it becomes necessary to fit the line to the data, which suggests the method of least squares.

At this point we note that Hu's method only provides a one-dimensional result, which may be insufficient if lateral displacement can not be neglected. If lateral displacement is to be known it is natural to instead choose to fit the phase surface, which we expect to be roughly circular in shape. A number of algorithms for fitting a circle to a general function are available [71].

One simple way that introduces the general method is to use Fourier analysis to identify the center points. A circle located at the origin in the x, y coordinate system is parameterised by

$$x = \rho\cos(\phi) \tag{A.2}$$

$$y = \rho\sin(\phi) \tag{A.3}$$

where ρ is a constant. If the circle is no longer located at the origin, we can retain this parameterisation by allowing ρ to become a function of ϕ (Fig. A.2(a)). The center coordinates of the circle are

$$d_x = \frac{1}{\pi}\int_0^{2\pi} \rho(\phi)\cos(\phi)d\phi \tag{A.4}$$

$$d_y = \frac{1}{\pi}\int_0^{2\pi} \rho(\phi)\sin(\phi)d\phi \tag{A.5}$$

which are the first-order Fourier coefficients of ρ. When ρ does not describe a circle, but instead describes a simple closed parametric curve, then the coefficients are the center coordinates of the circle that fits ρ in a least-squares sense. The extension to the case of a three-dimensional surface is straightforward. In this case

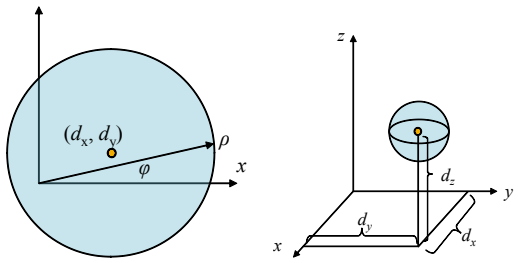

(a) 2-D. (b) 3-D.

Figure A.2: Interpretation of the coefficients d_x, d_y, and d_z as the x, y, and z phase center coordinates respectively.

the parameterisation of a simple closed surface is given by

$$x(\theta,\phi) = r(\theta,\phi)\sin(\theta)\cos(\phi) \tag{A.6}$$

$$y(\theta,\phi) = r(\theta,\phi)\sin(\theta)\sin(\phi) \tag{A.7}$$

$$z(\theta,\phi) = r(\theta,\phi)\cos(\theta) \tag{A.8}$$

with the center coordinates of the least-squares best-fit sphere given by

$$d_x = \frac{2}{\pi^2}\int_0^{2\pi}\int_0^{\pi} r(\theta,\phi)\sin(\theta)\cos(\phi)d\theta d\phi \tag{A.9}$$

$$d_y = \frac{2}{\pi^2}\int_0^{2\pi}\int_0^{\pi} r(\theta,\phi)\sin(\theta)\sin(\phi)d\theta d\phi \tag{A.10}$$

$$d_z = \frac{1}{\pi^2}\int_0^{2\pi}\int_0^{\pi} r(\theta,\phi)\cos(\theta)d\theta d\phi \tag{A.11}$$

This method works very well for closed surfaces. However, in practical circumstances we want to restrict the fitting algorithm to a portion of the main beam, while ignoring sidelobes and pattern nulls which degrade the quality of the fit. The Fourier method requires integration over a closed surface, so we must extend the algorithm by invoking the more general Method of Least Squares to estimate the Fourier coefficients.

A.4.1.1 Least Squares Computation of Phase Center

Rusch and Potter [72] used a least squares procedure to calculate the phase center of an antenna in a two-dimensional principal plane. In this section we extend this procedure to three dimensions. A general expression for the far field of an antenna in free space is

$$U(r,\theta,\phi) = F(\theta,\phi)\frac{e^{j\psi(r,\theta,\phi)}}{r} = F(\theta,\phi)\frac{e^{-jk_0 r}}{r}e^{jf(\theta,\phi)} \tag{A.12}$$

where $F(\theta,\phi)$ and $f(\theta,\phi)$ are real functions that describe the far field amplitude and phase, respectively. An ideal (spherical) phase function has the form

$$f(\theta,\phi) = C + d_x \sin(\theta)\cos(\phi) + d_y \sin(\theta)\sin(\phi) + d_z \cos(\theta) \tag{A.13}$$

where d_x, d_y, and d_z are the Cartesian coordinates of the phase center as before. Although a physically realizable phase function will not exactly have this form, we can approximate it with the following trigonometric polynomial

$$\xi(\theta,\phi) = a_0 + a_1 \sin(\theta)\cos(\phi) + a_2 \sin(\theta)\sin(\phi) + a_3 \cos(\theta) \tag{A.14}$$

Following the least squares procedure, the constants a_n are chosen to be those that minimize

$$I = \int_{\phi_1}^{\phi_2} \int_{\theta_1}^{\theta_2} [f - \xi]^2 d\theta d\phi \tag{A.15}$$

where the upper and lower limits of integration act in lieu of a weighting function, thereby uniformly weighting inside a specified field-of-view and neglecting contributions outside it. Considering I to be a function of the a_n, we wish to determine the values that minimize I.

$$\frac{\partial I}{\partial a_0} = 0 \qquad \frac{\partial I}{\partial a_1} = 0 \qquad \frac{\partial I}{\partial a_2} = 0 \qquad \frac{\partial I}{\partial a_3} = 0 \tag{A.16}$$

These equations form a linear system that can be solved for the a_n.

A.4.2 Validation

The phase center computation algorithm was validated (Fig. A.3) against the analytical results in [3] for the infinite-radius, infinite-armed equiangular spiral. In that paper, it was shown that for tightly-wrapped spirals the phase center was located an electrical distance $k_0 d_z = a$ behind the antenna, where k_0 is the propagation constant of free space, d_z is the location of the phase center, and a is the growth rate.

For validation, the Moment Method code **FEKO** was used to compute the radiation patterns of two-armed wire spirals. Before computing the phase center it is necessary to first unwrap the phase and then subtract away the inherent $2\pi m$ azimuthal phase progression, where m is the desired mode of excitation, in order to obtain a closed phase surface that is suitable for the sphere fitting routine. The previously discussed phase center computation algorithm was used, where trapezoidal integration was used to evaluate

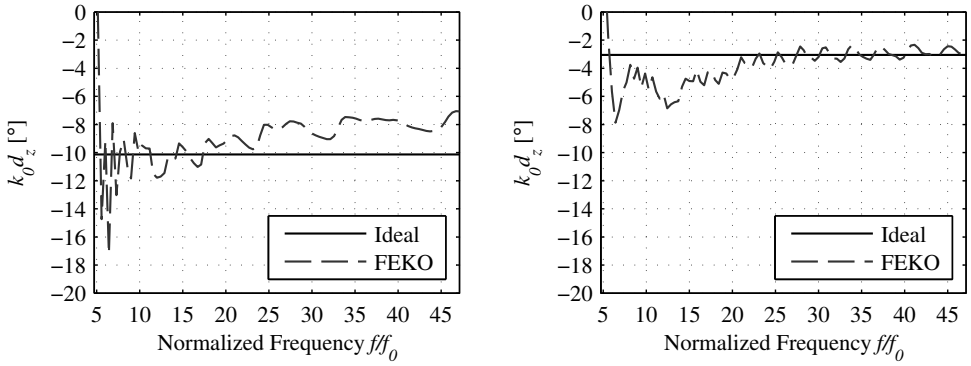

(a) Phase center vs. frequency for growth rate a = 0.1.

(b) Phase center vs. frequency for growth rate a = 0.03.

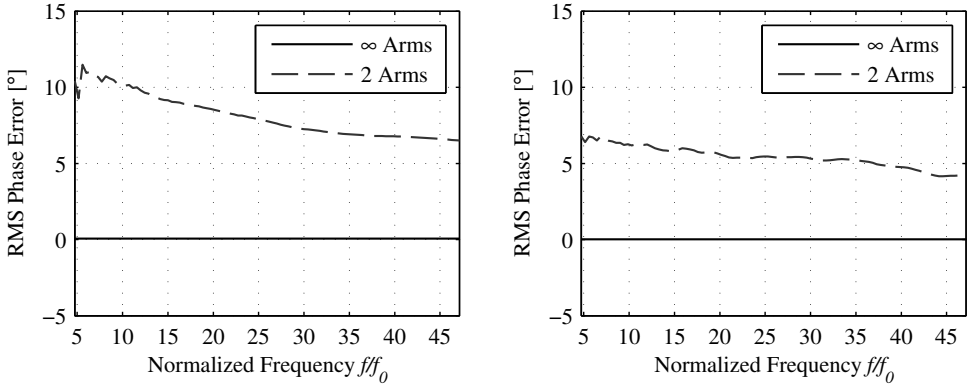

(c) Phase error vs. frequency for growth rate a = 0.1.

(d) Phase error vs. frequency for growth rate a = 0.03.

Figure A.3: Validation of the phase center computation algorithm against the infinite-armed case analyzed in [3]

the integrals that have the unknown phase function in the integrand. The resulting four linear equations were then solved numerically to yield the phase center.

It was found that good agreement between this theory and results computed with **FEKO** were obtained if the antenna structure in **FEKO** was sufficiently large ($f/f_0 \approx 10$). Since a two-armed equiangular spiral with a fine feed region ($r_{feed}/r_{max} < 0.01$) was used for this validation, contaminating effects of feed region radiation and of higher-order modes are believed to be negligible compared to the contaminating effects due to the spiral truncation.

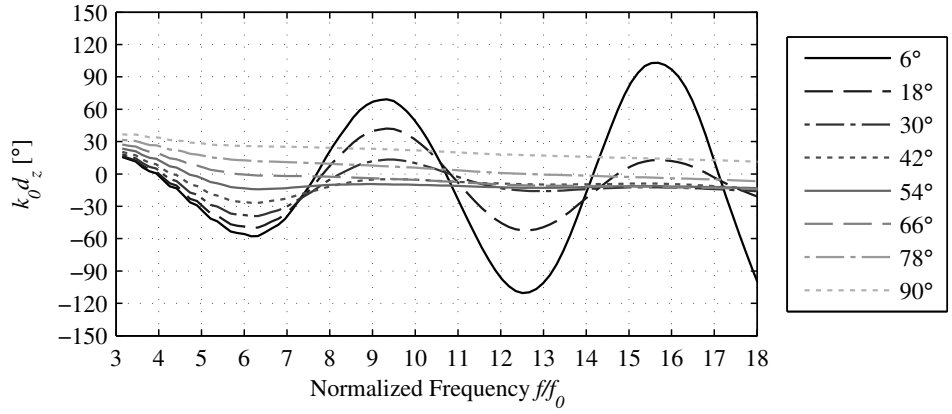

Figure A.4: Decreasing the field of view increases the sensitivity of the algorithm to small changes in the phase surface curvature close to broadside.

A.5 Studies

A.5.1 Effects of Field-of-View

The phase error and PCV can be decreased by reducing the field-of-view over which the least-squares procedure is performed. For investigation of the effect of field-of-view, a **FEKO** model of a four-armed free-standing equiangular spiral with a growth rate of a = 0.0616/rad and excited in Mode 1 was chosen. Figure A.4 shows that when considering a narrow field-of-view, small undulations in the phase surface curvature produce relatively large changes in the computed phase center position. This effect has been observed to be insensitive to the far-field sampling density within the field-of-view.

A.5.2 Effects of Excitation Mode

Since multi-armed spirals are most often used in monopulse systems, it is highly desirable for all modes to share a common phase center. Figure A.5(a) shows the phase centers for an eight-armed spiral with growth rate a = 0.14121/rad as modeled in **FEKO**. The phase center for each mode was calculated over its respective 3-dB beamwidth (M1: $0° \le \theta \le 38°$, M2: $18° \le \theta \le 60°$, M3: $27° \le \theta \le 66°$). The phase centers are co-located within 20° for frequencies above approximately nine times the cutoff frequency f_0. Below f_0, the phase centers exhibit undulation which is presumably due to the effect of end termination as discussed previously. The phase error increases for higher modes because the patterns progress lower in elevation,

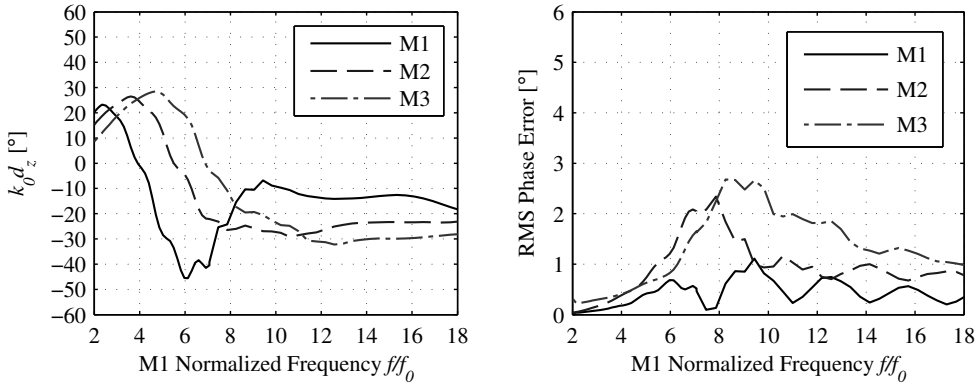

(a) Phase center.

(b) Phase error.

Figure A.5: Effect of changing the excitation mode. As the mode number is increased, the undulations are shifted higher in frequency due to the larger radiation region for increasing modes.

where the phase surface is increasingly nonspherical.

A.5.3 Effects of Number of Arms

Figure A.6 shows that increasing the number of spiral arms has little effect on the phase center stability. This study was performed using free-standing spiral models in **FEKO** with a growth rate of $a = 0.0616$/rad. However, the phase error associated with that phase center is large for the two-armed spiral for frequencies below the cutoff frequency, while the four- and eight-armed spirals have low phase error for all frequencies. This is because the two-armed spiral becomes linearly polarized near the cutoff frequency, which violates the assumption of a Mode 1 azimuthal phase progression. If the phase center of the two-armed spiral below cutoff is desired, then no azimuthal phase progression should be assumed.

A.5.4 Effects of Growth Rate

From Fig. A.7(a), where numerous phase centers are shown for a large range of growth rates, we can see that the phase center stability is not affected much by changing the growth rate. However, the phase error improves markedly with decreasing growth rate down to $a \approx 0.06$/rad, beyond which diminishing returns are seen. This is in qualitative agreement with the results from [3].

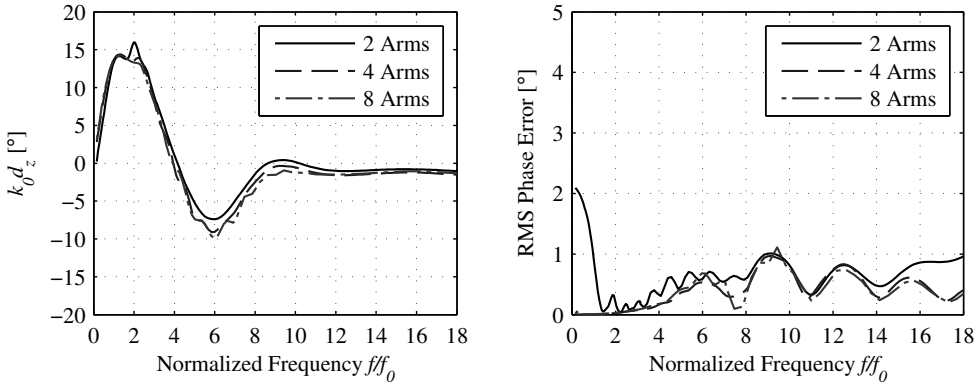

(a) Phase center. (b) Phase center variation.

Figure A.6: Effect of number of arms on the phase center of spiral antennas. Little effect is seen for the phase center, but the two-armed spiral has poorer phase error near the cutoff frequency f_0.

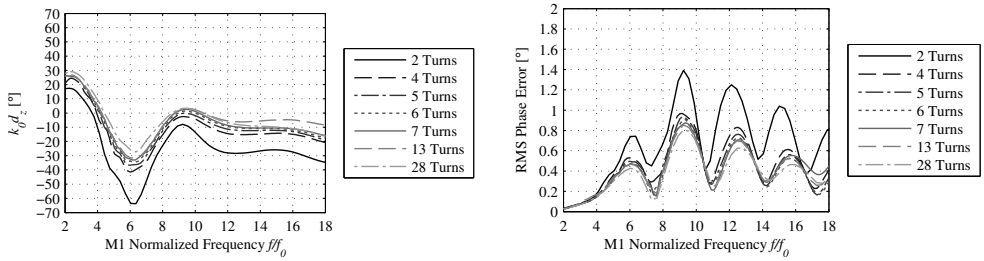

(a) Phase center. (b) Phase error.

Figure A.7: Effect of the growth rate on the phase center of spiral antennas. Little effect is seen for the phase center, but lower phase error is observed for lower growth rates.

A.5.5 Effects of End Termination

Figure A.8 illustrates the effect of adding an absorptive termination to the outside of the spiral. The particular spiral under study is an eight-armed spiral with four turns (0.1421/rad) modeled in FEKO. The unloaded spiral is 15 cm in diameter, while the loaded spiral is 20 cm in diameter with a 2.5 cm wide absorbing ring so that the unloaded diameter is also 15 cm. The inner diameter is sized to accomodate a bundle of eight 47 mil diameter semi-rigid coaxial cables. Figure A.8(a) shows that the variation of phase center with respect to frequency has been shifted lower, but the amplitude of the variation has not been diminished. This shift may be due to the increased size of the spiral due to the terminating portion. For the phase error, we see a similar effect of shifting lower in frequency.

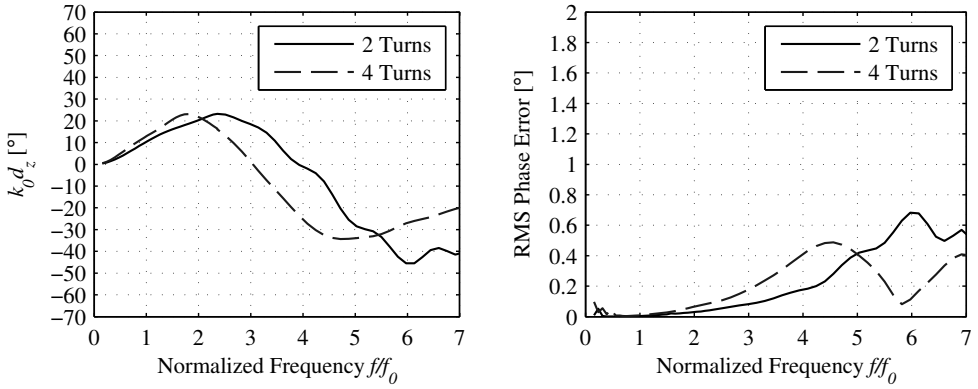

(a) Phase center. (b) Phase error.

Figure A.8: Effect of resistively terminating the spiral arms.

A.5.6 Effects of Reflective Cavity Backing

Typically a unidirectional radiation pattern is desired from a spiral antenna; however, the planar spiral inherently radiates equally both upward and downward. An absorbing cavity is most often used to accomplish this, because it causes the least degradation in the broadband properties of the radiation pattern. However, additional gain can be achieved in certain circumstances when the spiral is used with a reflective cavity backing. Figure A.9(a) shows that placing the unterminated spiral discussed in the previous section two inches above an infinite PEC plane causes large amplitude oscillations in the phase center, with an accompanying large phase error. We can see that upon adding the termination of the previous section to the spiral, the large-amplitude oscillations are highly dampened, and the phase error associated with that phase center is highly decreased, nearly to the level of the spiral in free space.

A.5.7 Effects of Beamformer Errors

Since physically realizable spiral beamformers have amplitude and phase imbalances, it is desirable to know how these imperfections affect the phase center of the spiral. The modal content of the beamformer outputs can be analyzed by performing a DFT. For a four-armed isolated spiral, only Modes 1, 2, and 3 can be excited. Any other modes (e.g. -1, 5, etc.) are excited only when energy is not radiated by these three. We will now study how the introduction of spurious modes can affect the phase center of a Mode 1

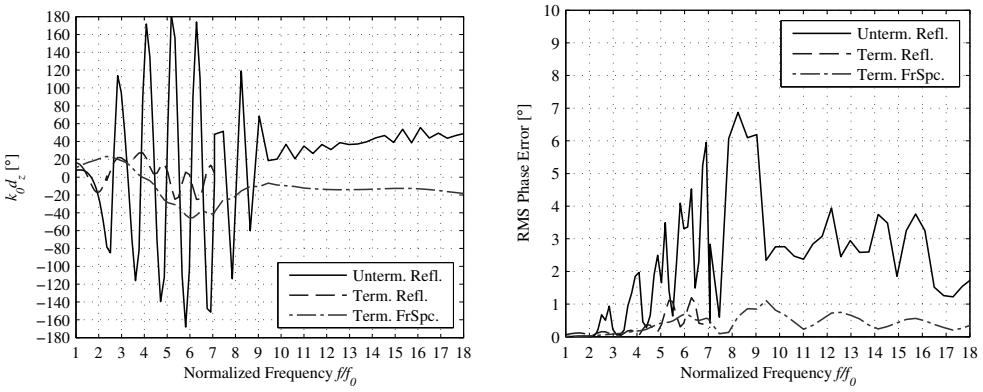

(a) Phase center. (b) Phase error.

Figure A.9: Reflecting cavity backed spiral. Adding resistive termination to the arms appears to help reduce the oscillations in the phase center.

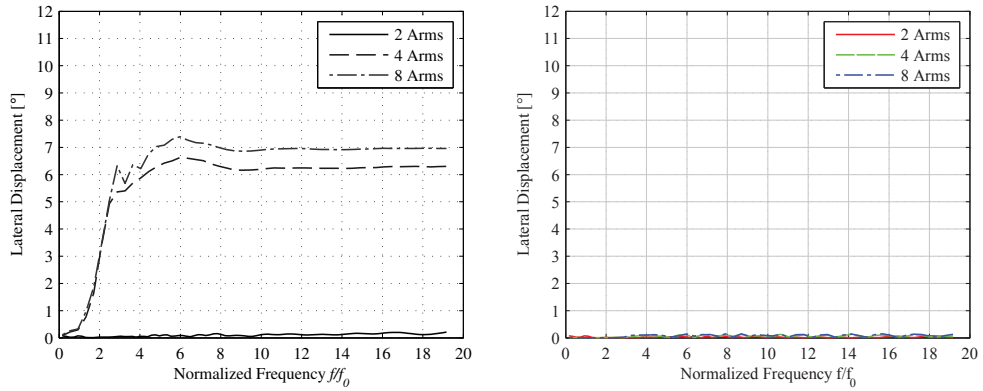

(a) Mode 2 contamination. (b) Mode 3 contamination.

Figure A.10: Lateral phase center displacement versus frequency for two types of contamination on a four-armed spiral. Mode 2 contamination causes significant lateral displacement, while Mode 3 contamination produces relatively very little displacement.

pattern. In this study the low-level spurious modes were mathematically superimposed individually on the ideal Mode 1 beamformer at a level 25 dB below that of Mode 1. This level corresponds to those observed in practical beamformers. Since Modes 1 and 2 combine to form a beam that is non-symmetrical in both amplitude and phase with respect to the spiral axis, we expect to see movement of the phase center in the lateral direction (Fig. A.10(a)). However, since Modes 1 and 3 combine to form a symmetric beam, we expect to see very little lateral movement of the phase center, and this is confirmed in Fig. A.10(b). If the phase center is allowed to move off-axis, then the Mode 2 contaminated pattern shows less phase error, and

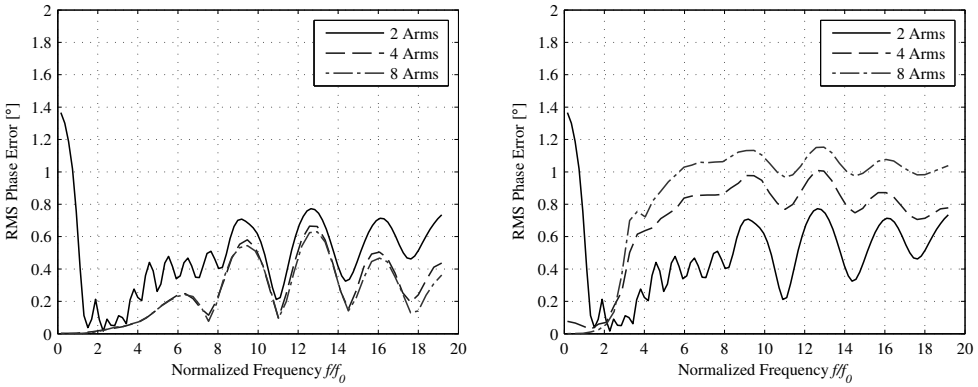

(a) Mode 2 contamination.

(b) Mode 3 contamination.

Figure A.11: RMS phase error versus frequency for two types of contamination on a four-armed spiral. Lateral displacement from Mode 2 allows there to be little additional phase error degradation. Phase error is higher for the Mode 3 case since the phase center does not move to compensate.

therefore a more well-defined phase center (Fig. A.11(a)). By contrast, Mode 3 contamination can not be compensated by moving off axis, so its effect on phase error is greater.

A.6 Conclusions

The purpose of this appendix was to investigate the phase center stability of spiral antennas. Along the way, we re-examined several existing definitions of phase center and found that each had their own deficiencies, leading us to present an alternate definition of the concept. A commonly-used term phase center variation (PCV) was reinterpreted in light of this alternate definition and was found to be simply related to the phase error committed by assigning a unique phase center.

Next, an algorithm for computing the three-dimensional phase center of antennas was presented. The additional capability to determine lateral displacements was useful for analyzing the effect of beamformer errors on phase center.

Increasing the number of arms of the spiral from two to four substantially improved the phase error near the cutoff frequency because the two-armed spiral loses the assumed $2\pi m$ phase progression. Decreasing the growth rate improved the phase error up to a point ($a \approx 0.06$/rad) after which diminishing returns were observed. Resistive termination of the spiral arms was seen to have little effect for spirals in the absence of a reflecting cavity, but was very useful once a reflecting cavity was introduced.

Finally, the effects of beamformer errors were examined and it was found that, for a four-armed spiral, contamination from Mode 2 produced a significant lateral offset with small phase error, while contamination from Mode 3 produced comparatively insignificant lateral offset but increased the phase error.

Appendix B

Multi-functional Broadband Arrays for UHF Through S-Band Electronic Warfare

B.1 Introduction

Recent interest in wideband arrays is mainly driven by the needs associated with radar (for example VHF/UHF foliage penetration (FOPEN) radar), electronic warfare (battlefield surveillance and/or direction finding) and consolidation of numerous sensor systems and functionalities into a single aperture [73]. To that end, the array bandwidth has been defined in different ways including the range of frequencies with specified maximal permitted reflection coefficient over field of view (scanning range), grating lobe appearance and their position [74], etc. To achieve wide bandwidth, common approaches revolve around the use of wideband elements like Vivaldi, bow-ties, spirals or TEM horns [75], or the exploitation of mutual coupling to achieve conditions resembling Wheelers current sheet [76].

A spiral antenna has several features that make it an appealing candidate for wideband arrays. First, it has a broad, frequency-stable pattern, thus enabling wide angle array scanning. Second, the pattern falls off near the horizon, thus reducing mutual coupling between array elements. Both of these qualities are highly desirable for multifunctional arrays that seek to combine electronic warfare tasks with communication. However, a spiral is typically absorber-backed, thus about half of its radiated power is lost and its power handling is severely limited [77]. Also, spirals do not tend to miniaturize readily, thus wide-angle wideband scanning can be affected by the appearance of grating lobes.

In this appendix we discuss the design and performance of a spiral-helix antenna array operating from

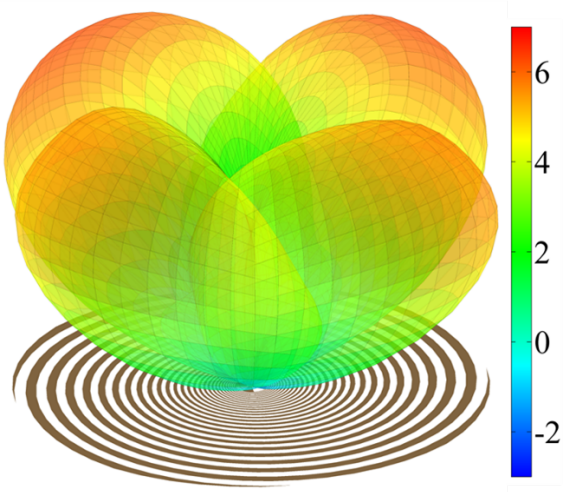

Figure B.1: One squinted beam is produced by each possible single-armed excitation of a four-armed spiral.

500 MHz to 2 GHz. A hexagonal lattice is utilized to increase the grating-lobe-onset frequency and improve the azimuthal uniformity of the radiation pattern. An equal-split corporate feed network is designed that can be used stand-alone for fixed-beam operation (as here) or combined with phasing elements to produce a scanned beam.

This appendix is organized as follows: first, we review some essential aspects of multi-armed spiral antenna theory. Then we exploit some properties of the utilized helix loading to permit its incorporation into a compact, wideband array element. Array topology and the design of a wideband seven-way equal-split corporate network are discussed next. Finally, the performance of the array with the spiral-helix element is presented, along with comparison to a typical antenna used in electronic warfare.

B.2 Element

B.2.1 Four-Armed Spiral Aperture

The four-armed spiral has been shown to be an excellent radiator for wideband monopulse sensing, where it has been commonly used as an element in missile seeker antennas [12]. As shown in Fig. B.1, the four symmetrical arms each produce a squinted beam, and the direction of an incoming wave can be determined by comparing the signal amplitudes that are received by each beam.

Table B.1: Comparison of the single-arm excitation basis and the spiral (phase) mode basis.

Mode	Single-Arm Modes				Spiral (Phase) Modes			
	$A_1 \angle \phi_1$	$A_2 \angle \phi_2$	$A_3 \angle \phi_3$	$A_4 \angle \phi_4$	$A_1 \angle \phi_1$	$A_2 \angle \phi_2$	$A_3 \angle \phi_3$	$A_4 \angle \phi_4$
0	$1 \angle 0°$	$0 \angle 0°$	$0 \angle 0°$	$0 \angle 0°$	$1 \angle 0°$	$1 \angle 0°$	$1 \angle 0°$	$1 \angle 0°$
1	$0 \angle 0°$	$1 \angle 0°$	$0 \angle 0°$	$0 \angle 0°$	$1 \angle 0°$	$1 \angle -90°$	$1 \angle 180°$	$1 \angle 90°$
2	$0 \angle 0°$	$0 \angle 0°$	$1 \angle 0°$	$0 \angle 0°$	$1 \angle 0°$	$1 \angle 180°$	$1 \angle 0°$	$1 \angle 180°$
3	$0 \angle 0°$	$0 \angle 0°$	$0 \angle 0°$	$1 \angle 0°$	$1 \angle 0°$	$1 \angle 90°$	$1 \angle 180°$	$1 \angle -90°$

Alternatively, the incoming signal amplitudes appearing at the four terminals of the spiral can be Fourier-decomposed into a different set of orthogonal spiral (phase) modes V_m, which also happen to be the eigenvectors of the spiral's impedance matrix. The individual arm and phase mode excitations are outlined in Table B.1.

As shown in Fig. B.2, when viewed as a radiator, the spiral antenna does so from the ring-shaped active regions of circumference $m\lambda$, where m is the mode index and λ is the guided wavelength of the wave traveling along the spiral arms. The radiation of each mode m is in general elliptically polarized, with the positive (outward-traveling) modes being cross-polarized to the negative (inward-traveling) modes. The radiated field due to the mode m active region will have the azimuthal phase progression equal to $e^{-jm\phi}$. Viewing a vector representation of the active-region currents at boresight, one would see that the vectors cancel for the modes $|m| \neq 1$ active regions, thus creating deep boresight nulls as shown in Fig. B.3. The depth of the null is important for seeker guidance accuracy.

If an outward-traveling $m = 1$ pattern with perfect circular polarization at boresight is desired, then the inward-traveling mode $m = -1$ must be eliminated. On a two-armed spiral this is accomplished by resistively terminating the spiral arms, thereby preventing the $m = -1$ mode from reflecting and propagating inward. This strategy is often difficult to implement satisfactorily, especially when the spiral is near its cutoff frequency $f_0 = c_0/C$, where c_0 is the speed of light and C is the circumference.

Alternatively, one can exploit the fact that a four-armed aperture does not radiate mode $m = -1$ when supplied with a mode $m = 1$ excitation. This property ensures that the boresight cross-polarization will be limited only by the quality of the beam-forming network (BFN) and the symmetry of construction. Compared to the two-armed spiral, the four-armed structure will also have much better purity of the radiated

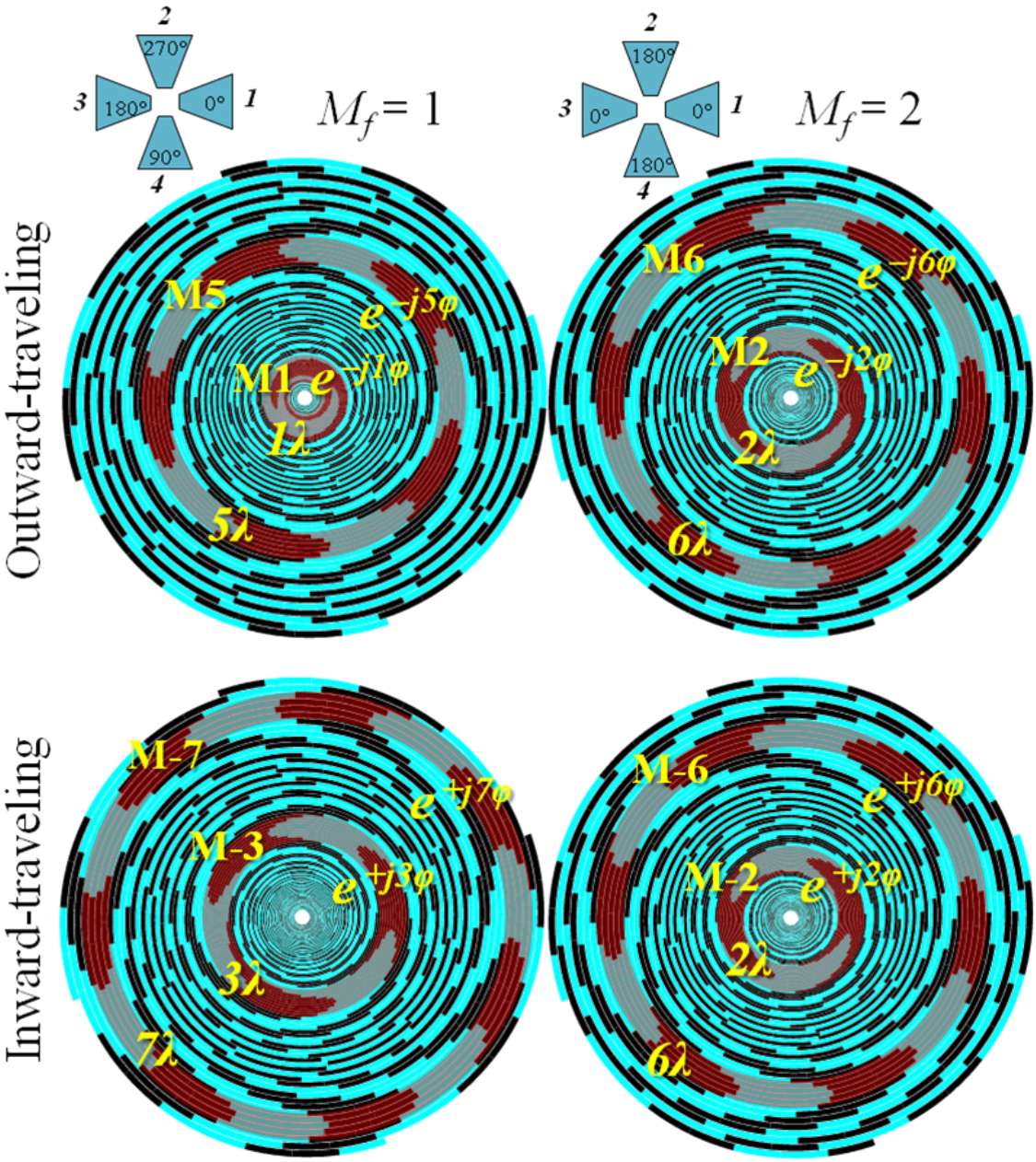

Figure B.2: Plots of the instantaneous phase along the arms of a four-armed spiral when excited at the center in spiral modes 1 (left) and 2 (right). The inward-traveling modes occur when energy reflects from the arm ends.

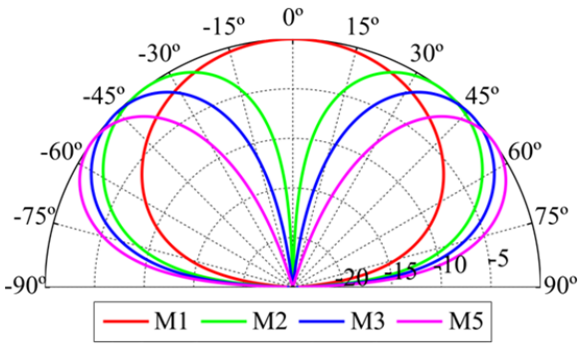

Figure B.3: Theoretical mode patterns obtained in [3]

far-field (see Fig. B.4).

The fabricated spiral aperture is 15.24 cm in diameter, with a growth rate $a = 0.1828$/rad. The spiral is etched from 56.7 g (2 oz.) copper foil laminated onto 1.5875mm (62.5 mil) thick FR-4 dielectric. The growth rate $a \approx 0.22$/rad was chosen as a compromise between off-boresight axial ratio (favoring low a) and power handling (favoring high a).

B.2.2 Spiral-Helix

One approach used to extend the low-frequency ($f < f_0$) performance of the spiral is to terminate the ends with a helix (Fig. B.5). The combination of the spiral, helix, and ground plane results in an element that exhibits good low- frequency gain while maintaining low axial ratio and azimuthal gain ripple. The performance of this antenna is compared with the scaled performances of common COTS spirals and the results are shown in Fig. B.6.

B.3 Array

B.3.1 Rectangular vs. Hexagonal Lattice

Electronic warfare antennas require the largest practical bandwidth, and therefore care should be taken to choose the array configuration that gives the best possible pattern integrity. For a given element spacing, the hexagonal lattice not only improves the beam symmetry, but also increases the frequency of first grating lobe onset compared to the rectangular lattice (see Table B.2).

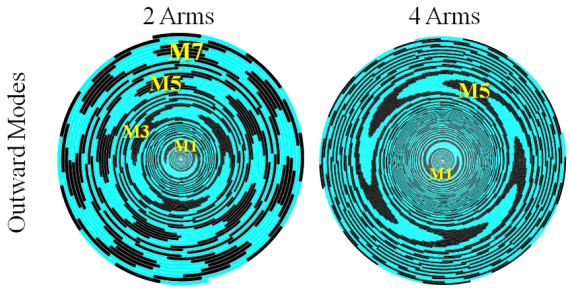

Figure B.4: Comparison of the mode-filtering properties of the two- and four-armed spiral apertures. The four-armed spiral radiates fewer modes than the two-armed spiral, and therefore has a cleaner pattern.

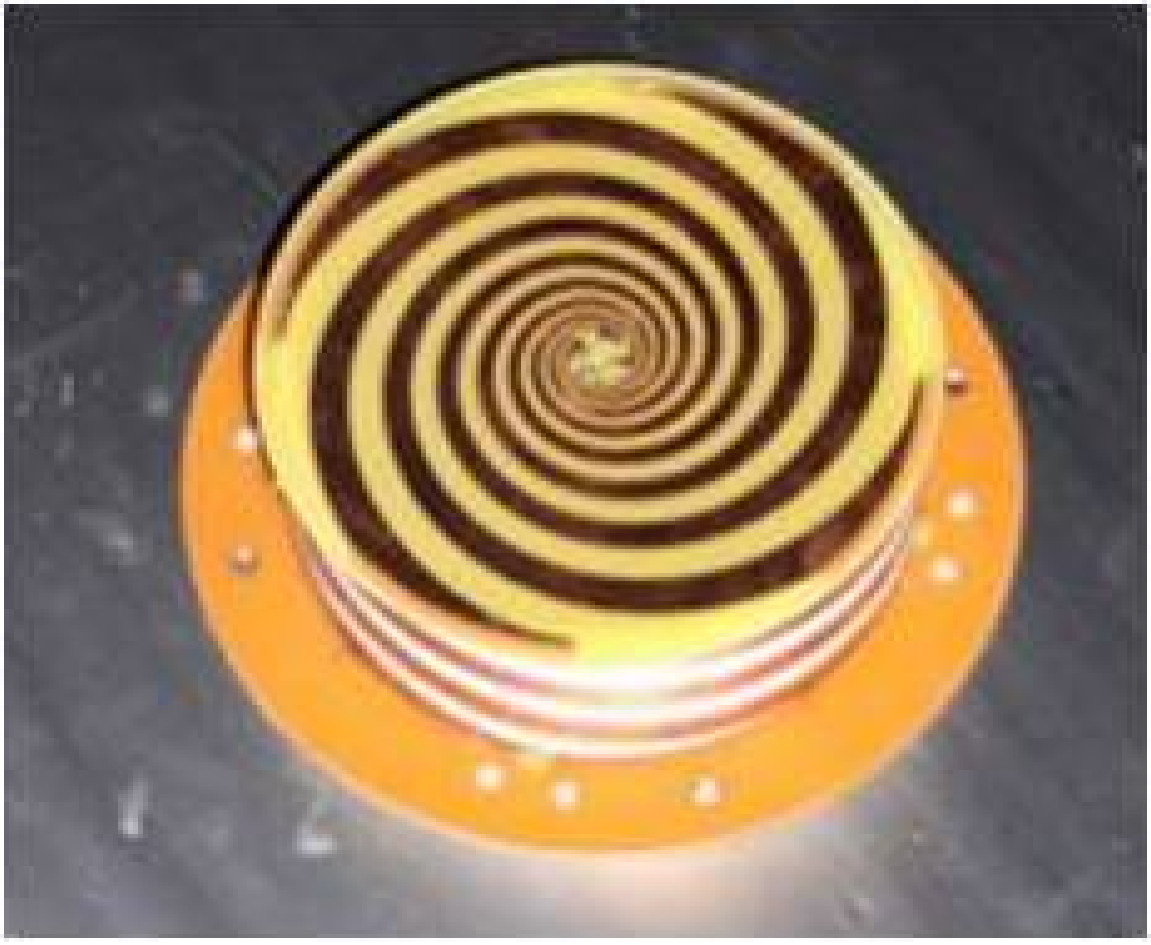

Figure B.5: Four-armed spiral-helix

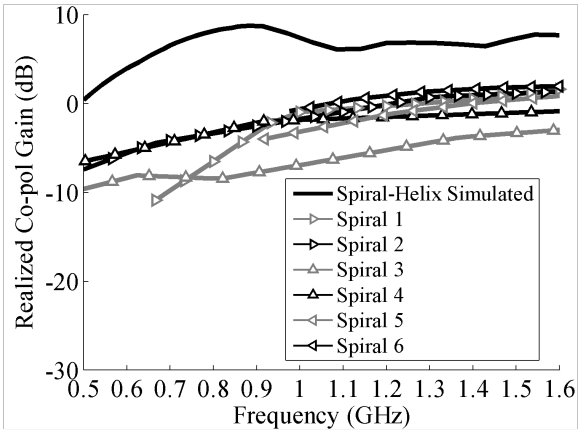

Figure B.6: Performance of the spiral-helix compared to scaled-aperture commercially-available spirals.

Table B.2: Approximate grating lobe onset frequencies (for $\theta_p = 90°$ from boresight) for corporate-fed arrays with 200 mm element separation.

Lattice Type	Grating Lobe Onset Frequency
3-by-3 Rectangular	1.45 GHz
7-element Hexagonal	1.67 GHz

B.3.2 Circular Array

In addition to increasing the grating-lobe onset frequency, the use of a hexagonal lattice with six elements placed around a central element yields a circular array, which can be useful for direction-of-arrival (DOA) estimation. For example, the four squinted beams of the four-armed element can be used for amplitude monopulse, while the six outside elements create displaced mode 1 phase centers that provide phase monopulse capability. Other DOA strategies are also possible.

An important parameter for the accuracy of DOA systems is the azimuthal gain ripple (WoW). This parameter particularly affects the amplitude monopulse beam ratio, making it difficult to associate a given beam ratio to a unique angle. This causes ambiguity in the signal elevation estimate. Furthermore, WoW indicates underlying azimuthal phase nonlinearity, which affects phase comparison DOA estimates.

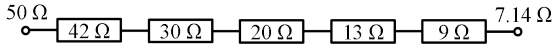

Figure B.7: Prototype impedance transformer used in the design of the corporate feed network.

B.3.3 Feed

The simplest feed type for a boresight beam is the uniform corporate feed network. To realize a scanning array, phasing elements may be distributed along the structure. The corporate feed network discussed here employs a five-step 7:1 impedance transformer (shown in Fig. B.7) as a prototype, providing an equal-ripple 20 dB impedance match over the 0.5-2 GHz bandwidth. The corporate network shown in Fig. B.8 is derived from the prototype by splitting the transformer into seven parallel branches while multiplying the port and line impedances by seven. To obtain acceptable line impedances, some sections are re-combined, dividing by the total number of output ports of the resulting divider in that branch. This results in a combination of two- and three-way power dividers. Following this procedure, the resulting corporate feed has the same return loss as the prototype transformer, and with equal power division among the ports. Each output port of the corporate feed is connected to a four-armed mode 1 beam-forming network (Fig. B.9) prior to the antenna connection.

B.3.4 Realization

A seven-element hexagonal array excited in this way has the radiation pattern shown in Fig. B.10. The boresight gain (Fig. B.11) and beamwidth (Fig. B.12) both compare favorably to that of a quad-ridged horn antenna typically marketed for electronic warfare. Due to the excellent boresight cross-polarization suppression of the individual elements, the beam has very low axial ratio within the beamwidth. The pattern

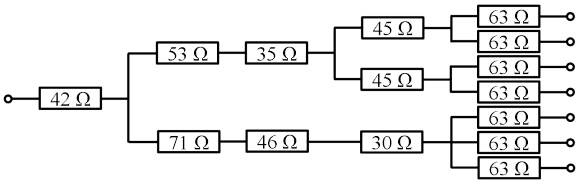

Figure B.8: Seven-element corporate feed network for achieving an equal power split over a 4:1 bandwidth with 20 dB return loss.

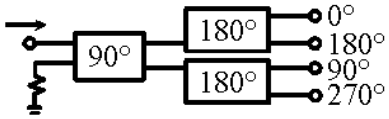

Figure B.9: Realization of a mode 1 beam forming network (BFN) using a 90 hybrid and two baluns

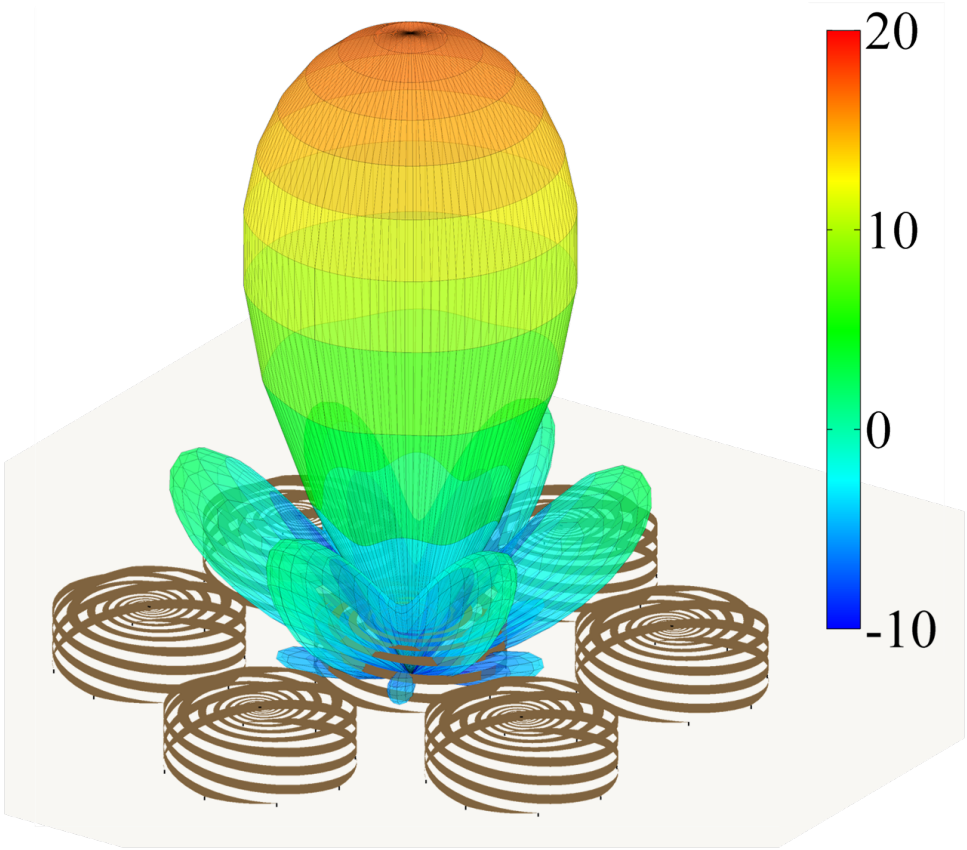

Figure B.10: **FEKO**-simulated pattern of the seven-element hexagonal array at mid-band (1.25 GHz).

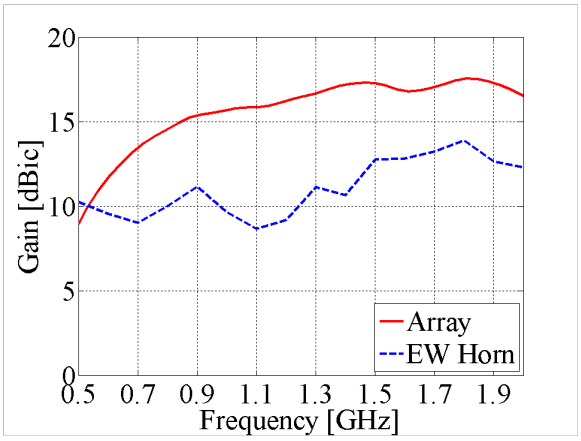

Figure B.11: Comparison of **FEKO**-simulated boresight gain of the seven-element hexagonal array to that of a quad-ridged horn antenna.

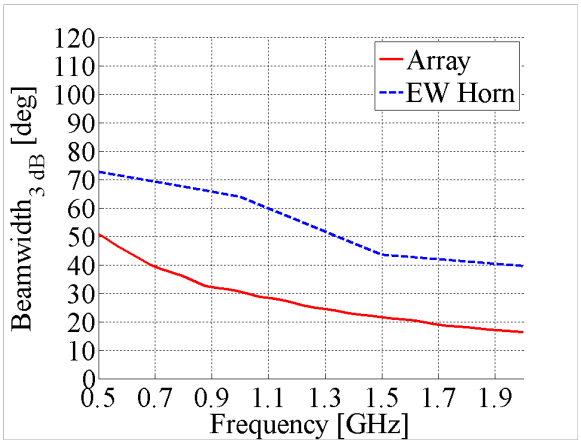

Figure B.12: Comparison of **FEKO**-simulated beamwidth of the seven-element hexagonal array to that of a quad-ridged horn antenna.

shows acceptable stability versus frequency with the main beam having low WoW (< 0.7 dB at 15° from boresight) as compared to the rectangular-array topology. Peak sidelobe levels are -20 dB, -10 dB, and -6 dB at 950 MHz, 1.7 GHz, and 2 GHz respectively.

B.4 Conclusions

An antenna array designed as an alternative to the currently-available quad-ridge horn antenna for multi-functional electronic warfare application has been discussed. A combination spiral-helix array element has been developed and its broad bandwidth and beamwidth, excellent boresight cross-polarization, and compact size are demonstrated. The choice of hexagonal lattice configuration is justified by its higher grating-lobe-onset frequency and better pattern symmetry. An equal-division seven-way corporate feed network with 4:1 20dB return-loss bandwidth based on a 5-section 7-to-1 impedance transformer was designed and integrated with spiral-helix modeformers to excite the array. For the array, higher gain and narrower beamwidth compared with a typical electronic warfare antenna are demonstrated.